The Role of Aggregates in the Thermal Stability of Mg-PSZ Refractories for Vacuum Induction Melting.

Amanda Gail Quadling

August 2014

Submitted in partial fulfilment of the requirements for PhD Materials Science and Engineering.

Imperial College London

Department of Materials

I declare that the work presented in this document is entirely my own except where duly attributed to other researchers by in-text referencing.

ABSTRACT

Mg-PSZ refractories used as vacuum induction melting crucibles are particle-reinforced composites with aggregate and matrix phases comprising fused zirconia. Three commercial varieties were cycled eight times to service temperatures and their microstructural and thermomechanical evolution investigated, with focus placed on the aggregate populations.

Two refractories, with large aggregates of similar size, were found to retain stiffness after cycling but in the refractory containing aggregates with high stabiliser levels, reaction between the stabiliser and Al and Si impurities produced secondary phases. Volume changes accompanying formation of these phases, and subsequent thermal expansion mismatches, led to aggregate break-up with consequent reductions in refractory toughness and strength. Secondary phases developed only rarely in the aggregates (with lower levels of stabiliser) of the second refractory. These aggregates remained intact and the refractory retained its toughness and strength. A third refractory contained small, unstabilised aggregates in a stabilised matrix and the strain mismatches that ensued during polymorphic transformation damaged microstructural interfaces. Refractory stiffness halved within eight cycles and toughness and strength were lost. All three refractories displayed R-curve behaviour and quasi-stable fracture curves were observed during bend tests.

The study shows that when using fused zirconia aggregates to design refractories, engineers need to i) limit stabiliser concentrations - a difference of just ±1 wt% Mg (in the presence of impurity elements) may determine whether secondary phase formation occurs and ii) eliminate alumina and silica impurities when possible through substitution of zircon sand with baddeleyite as the source for fused zirconia.

This thesis is dedicated to Kevin Quadling.

Thank-you for everything you have given and done and been over the past few years to make this degree a possibility.

ACKNOWLEDGEMENTS

Garry Stakalls spent dozens of hours cutting very large refractories into very small bars and his technical support was critical in the first two years of this project. Likewise, Ben Chang assisted with training on, and supply of, equipment in the cutting and bend test labs on many, many occasions over my time at Imperial. Thank-you technicians!

Cyril, Dan, Doni, Edo, Ele, Jenny, Miriam, Nasrin, Omar and Rob - thank-you all for your assistance with instruments, lab supplies and logistics, theory inputs and general crises aversion while we walked the postgrad path together. You have all been warm and wonderful colleagues.

The work in this thesis benefited from informal discussions with Prof. Arthur Heuer (Case Western University), Prof. Richard Bradt (University of Alabama) and Dr David Dye (Materials Dept., Imperial College). Special thanks to Dr Julie Prytulak (Dept. of Earth Science and Engineering, Imperial) for the support on ternary phase diagrams, Dr Maria Parkes (Dept. of Mechanical Engineering, Imperial) for assistance with the Raman spectroscopy and Dr Paul Lickiss (Dept. of Chemistry, Imperial) who went to considerable trouble assisting me with modeling of the crystal structures of the zirconia polymorphs for my own understanding of my materials.

My heartfelt thanks goes to Elaine Gower at Magma Ceramics and Catalysts (formally Morgan Dense Fired Shapes) who saved the day with delivery of a large batch of sample bars for the mechanical tests and quick responses to endless enquiries about crucible manufacture and performance. Gordon Bennet at Imerys first raised the spectre of impurity elements in fused aggregates and put this thesis on track. Morgan Dense Fired Shapes supplied the samples and some funding towards running costs.

Finally, to my supervisors: Bill, the UFSCar event was a fabulous entry to the world of materials science. For that and the many practical ways in which you've supported me during this PhD, thank-you so much. Luc, I have tremendous respect for the rigour of your science. It has been a privilege to learn from, and work with, you these past three years.

Portions of this work have been presented / published as follows :

- A.Quadling, L. Vandeperre, W.E. Lee and P. Myers, High Temperature Characteristics of Refractory Zirconia Crucibles used for Vacuum Induction Melting, in *Proceedings of the Unified International Technical Conference on Refractories*, UNITECR 2013, edited by Dana G. Goski and Jeffrey D. Smith, Wiley, **2013**.
- Aggregate Evolution During Thermal Cycling of Zirconia Refractories. Presentation given at the *CASC Industry Day*, Imperial College, **17 Jan 2014**.
- A Raman Study on the Microstructural Changes of Zirconia Aggregates During Thermal Cycling. Poster presented at the *SCERN Meeting*, Stoke-on-Trent, **5 March 2014**.
- A Raman Study on the Microstructural Changes of Zirconia Aggregates During Thermal Cycling. Presentation given at the *Department of Materials Postgraduate Day Seminar*, **24 March 2014**.
- A. Quadling, L. Vandeperre and W.E. Lee, Second Phase-induced Degradation of Fused Mg-Partially Stabilized Zirconia Aggregates. (Manuscript submitted to *Journal of the American Ceramic Society* in August **2014; revisions underway**).
- A. Quadling, W.E. Lee and l. Vandeperre, The Impact of Thermal Cycling on the Mechanical Properties of Fused Mg-Partially Stabilized Zirconia Aggregates. (Manuscript in preparation).

TABLE OF CONTENTS

LIST OF FIGURES

LIST OF TABLES

1. INTRODUCTION

1.1. The field of refractories

A refractory is a ceramic that specifically offers high temperature (>1580 °C) resilience[1]. Unlike the majority of structural and functional ceramics, refractories are characteristically heterogeneous at micrometre (micron) scale, multiphase and porous (often 10-20% porosity or greater[2]). Physically, these materials can be separated into three broad categories as fired shapes (bricks or complex forms), monolithics (castable or flowing forms) and insulators (fibres, foams and flakes), with end-use dominated by the iron and steel sector (Fig. 1).

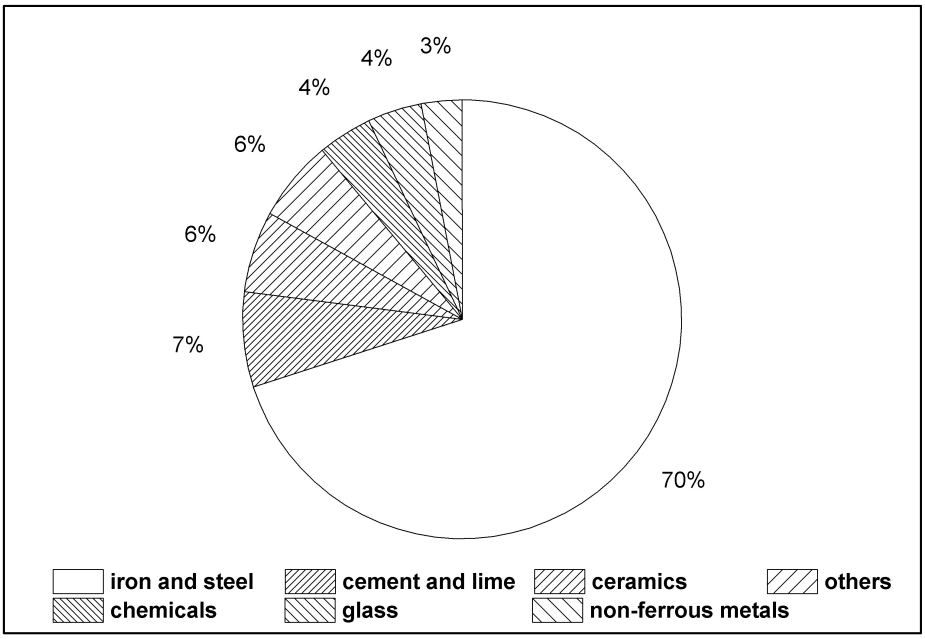

Figure 1 : World refractory usage by sector, in 2003. Data derived from Garbers-Craig[3].

The International Standards Organisation Committee (ISO) separates the most common refractory types by composition: alumina-silica (acidic) versus basic (non-acid) varieties containing low and high residual carbon, but designates zirconia a "special material"[4], underlining its less mainstream status. Yet, among the refractory materials, zirconia offers one of the highest melting temperatures (2710 °C)[5] and most stable chemistries against reduction and dissociation (Gibbs free energy of formation -1040 kJ/mol)[6]. These characteristics suggest zirconia will remain a refractory of importance for some time to come. Its usefulness as a

ceramic can be traced from 1929, when metal oxide additives were found to stabilise the higher temperature crystal forms to room temperatures[7]. Over the past six decades, its most exploited characteristic has become the polymorphic transformation of its tetragonal form to monoclinic, which produces a volume change that can be used for terminating propagating cracks. Zirconia is thus not only a material of uniquely high fusion temperature and low chemical reactivity, it offers the highest toughness values of any refractory oxide[6].

The transformation toughening aspect, a *nanometre scale* phenomenon, has meant that most of the investigations dedicated to zirconia have focused on the ceramic, rather than refractory, forms of the material. Fired refractory shapes are composites, comprising a reinforcement phase within a matrix[8]. Their toughness arises from microcracks generated ahead of propagating cracks, crack deflection around heterogeneities or crack bridging in the wake of propagating cracks, due to the reinforcement phase[9] i.e. their toughness mechanisms are triggered by physical features at the *micrometre scale*. The question that arises in the case of a zirconia fired refractory shape then is whether transformation toughening is relevant at all and if so, in the reinforcement phase, matrix phase or interface between them?

1.2. Why use zirconia refractories ?

Recent industry forecasts predict the fastest-growing refractory market to be that of contract engineering with 50,000 tons of production estimated through 2016[10]. Over the past century, development of precision-engineered components, for example those in turbines, has been driven by evolving aerospace and energy applications. These components comprise metal alloys required to withstand ever-increasing extremes of temperature (>1050 °C) and oxidation. From the discovery in the 1930's that Ti and Al additions to standard nickel-cobalt heating elements improved creep, to the release of the first 'superalloy', Nimonic 75, metal alloy improvement has continued to the present[11]. "Superalloys as a class constitute the currently reigning aristocrats of the metallurgical world. They are the alloys which have made jet flight possible"[12]. These nickel-based superalloys are produced to extremely tight chemical specifications, requiring deoxidation, removal of trace elements and modification with almost a dozen trace elements[13]. The process best suited to this metallurgy is Vacuum Induction Melting (VIM).

In VIM furnaces, vacuum pressures of ±1-700 Pa prevent oxidation and enable vaporisation of impurities through pressure-controlled reactions. Because the process exploits the high vapour pressures of unwanted trace elements, zirconia - with its low reduction pressures above 1600 °C ($Pressure_{carbonmonoxide}$ = 133 Pa) - is an ideal crucible material. Only CaO offers better P_{CO} but due to moisture sensitivity, is not as stable[14]. This makes zirconia-based refractories pivotal within the VIM environment.

VIM furnaces are heated to approximately 1700 °C with a superalloy charge held in molten state for several hours to degas C, H, O and N and homogenise after alloy additions[15]. The product ingot may be further refined through vacuum arc remelting (VAR) and/or electroslag remelting (ESR)[14] and the upgraded alloy investment cast, or processed into wrought product or powders[16]. Between charges, crucibles remain at high temperature and cooling to room temperature is only undertaken at the end of a campaign. Small batch processing is possible, enabling fast heats but also placing tremendous thermal strain on the crucibles employed. Here, zirconia's phase change around 1100 °C looms disadvantageously.

1.3. The concept of stabilisation

Zirconia has six crystallographic forms[5], three of them capable of room temperature stability: monoclinic (m), tetragonal (t) and cubic (c). Without stabilisation, the m-t transformation, occurring at approximately 1173 °C, is martensitic (diffusionless) and accompanied by a lattice contraction[17]. This phase "inversion" reverses on cooling, with the t-m transformation, observed around 950 °C, producing a 4-5 vol% increase[18]. These rapid physical changes with thermal cycling make pure zirconia unsuitable as a refractory. However, in 1929, it was discovered that addition of metal oxides (CaO, MgO and oxides of the rare earths such as CeO and Y_2O_3) to pure zirconia would diminish or remove the transformation effects[7]. During the next three decades some confusion arose when complete suppression of the t-m transformation (at doping up to 14 mol% MgO, for example) did not improve thermal shock resistance[19]. It became clear that multiple physical and thermodynamic principles were at play. Garvie[20] provided a stabilisation mechanism that did not involve dopant oxides in 1965: smaller grain sizes were shown to lead to tetragonal phase stability at low temperatures, due to their increased surface energy contribution to the total free energy of the system.

Ongoing phase diagram development indicated that cubic phase stabilisation with metal oxides arises because of oxygen non-stoichiometry. The substituting metal cations trigger charge-compensating oxygen vacancies thereby reducing oxygen coordination numbers for the cubic lattice zirconium. A similar mechanism is not necessarily applicable to the tetragonal phase, which can lower its oxygen coordination number simply through re-organisation of its oxygens into interpenetrating tetrahedra[5].

The exact mechanism/s of stabilisation remain in question today. Heuer[21] has stressed that the process of transformation requires nucleation sites. For magnesia-partially-stabilised zirconia (Mg-PSZ) materials - in which metastable tetragonal precipitates are distributed within a fully stabilised cubic matrix - these sites are likely to be c-t interface dislocations triggered by loss of coherence when the t-precipitates grow during ageing.

After many decades of empirical study, zirconia ceramic and refractory manufacturers now use a variety of heating and rapid/slow cooling combinations to precipitate and grow the exact phase combinations required to produce microstructures of specified strength and toughness, dependent on metal oxide stabiliser. Stabiliser distributions are not necessarily homogeneous throughout the product zirconias as this randomness is in itself advantageous to toughness in some instances[22].

1.4. A knowledge gap

Zirconia *ceramics* are in wide-spread use as dental implants, metal extrusion die nozzles and thermal barrier coatings[6]. A proliferation of combinations of zirconia with alumina (zirconia toughened alumina, ZTA), mullite (reaction sintered mullite zirconia, RSMZ) and cordierite, among other compounds, has given rise to ceramic composites known for retaining their strength to at least 1000 °C[23 24].

Zirconia-based *refractories* are less well documented in the scientific literature and mainly found in the highly corrosive environment of glass furnaces. High zirconia fused cast (HZFC) materials, used in alkali glass campaigns, comprise monoclinic zirconia aggregates in a 6-10 wt% vitreous matrix of silica, alumina and soda/boron[25]. Such high-zirconia materials have been quite thoroughly studied by French ceramicists who have shown that three levels of non-

reversible microstructural damage result with thermal cycling : i) microcracking in the zirconia aggregates due to phase transformation, along with ii) microcracking due to thermal expansion mismatches between the zirconia aggregates and glassy matrix, in addition to iii) delayed cracking at ambient temperatures several days after heating, due to stress relaxation[26 27]. The non-linear mechanical behaviour that results from this microcrack damage is termed 'flexibility' and offers benefits in terms of thermal shock resistance[28]. New developments on HZFC's involve doping with pentavalent oxides to reduce oxygen vacancy sites, which improves electrical resistivity and should allow these refractories to be used as electrode blocks[25]. While some studies have examined the detailed behaviour of alumina aggregates in refractories[29], as can be best ascertained, studies on zirconia aggregates in zirconia matrices remain unknown.

1.5. The research problem

This dissertation is aimed at addressing the gap identified above. What is the refractory performance of mono-mineralic zirconia fired shapes and how central to this performance are the fused aggregates, as opposed to the matrix phase or aggregate-matrix interface? In order to understand this, it was felt necessary to observe the *evolution* of fused zirconia aggregate *microstructure*, with any corresponding *evolution* in its *thermomechanical* behaviour, in order to determine whether and how aggregates alter under service conditions and whether and how this affects their suitability in crucible refractories. By selecting a set of samples representing variable matrix and matrix-interface contexts, it was hoped the role of the aggregate could be isolated.

The sample set chosen comprises three Mg-PSZ crucibles used for VIM (Fig. 2), and constituted of fused Mg-PSZ aggregates bonded with Mg-PSZ fines. These crucibles are routinely cycled above 1500 °C. To minimise thermal shock damage, the refractory remains around service temperatures for several charges but is cooled to room temperature between campaigns. Anecdotal evidence indicates crucible failure after ±9-90 campaigns[30] with some suppliers describing vertical cracking at top perimeters, horizontal cracks along mid-regions and within bases[31]. Establishing the modes and mechanisms of modification with service, for these specialist materials, is critical to engineering design for improved crucible performance. Given

the high value of the melting charges they contain, such study brings direct economic benefits to the metallurgical process.

Figure 2 : Commercial Mg-PSZ refractory crucibles used for VIM of Ni-Co alloys.

1.6. Approaching the research

Expecting the scale at which refractories' microstructure might modify mechanical performance to be micrometres[32], rather than the nanometre environments of ceramics, this project proceeded with the intention of focusing on micrometre-scale features. A threefold methodology was employed :

1. Qualitative evaluation of images was undertaken to identify and describe microstructural modifications.
2. Quantitative study of the chemistry and phase composition was used to interpret the observed microstructural modifications. Two aspects of chemistry were targeted: mobility of the stabiliser and impact of impurity elements. Since m-t and t-m phase changes in zirconia produce dilatational and deviatoric stresses[33] and therefore have direct bearing on mechanical stability, the extent to which these polymorphic transformations are irreversible was of interest. Repeated thermal cycling was expected to reduce material available for subsequent transformations.
3. Mechanical and physical testing focused on thermal expansivity, stiffness, strength and fracture toughness. Since the load born by crucible refractories is mainly thermal, as opposed to structural, creep was considered a lower priority, along with compressive strength.

1.7. Structure of the thesis

Following this introduction (Chapter 1) and a review of published discourse relevant to the microstructure and thermomechanical character of Mg-PSZ (Chapter 2), the Materials and Methodology section (Chapter 3) includes a brief overview of the raw supplies and manufacturing process used to produce fused Mg-PSZ aggregates. This provides context for the chemical characteristics recorded during material evaluation.

With respect to methodology in Chapter 3, greater detail is given on those techniques considered newer and less well-known (image analysis, impulse excitation, confocal Raman) than the established methods of X-ray diffraction (XRD), scanning electron microscopy with energy dispersive spectroscopy (SEM-EDS) and wave dispersive spectroscopy (SEM-WDS), transmission electron microscopy (TEM) and three point bend testing. Some focus is placed on challenges regarding data interpretation (in the case of dilatometry curves, for example) and test specimen geometry (in the case of fracture toughness).

Since there are two narratives implicit in this study - the microstructural and thermomechanical evolutions respectively - it was decided to present them as two distinct themes (Chapters 4 and 5), each with their own Results and Discussion sections. The Discussion in Chapter 5 integrates findings from Chapter 4, in order to establish linking mechanisms between the evolutions.

Finally, the Conclusions (Chapter 6) section evaluates what has been achieved; its relevance and restrictions. Implications for material design are highlighted and further work ideas recommended.

2.1. Microstructural considerations for fused Mg-PSZ

2.1.1. The complexity of Mg-PSZ

As discussed in the Introduction, the advent of metal oxide stabilisation, enabling high temperature polymorph combinations at room temperature, allowed production of viable zirconia ceramics. According to Porter and Heuer[34], magnesia-*stabilised-zirconia* is actually a *metastable* cubic phase at room temperature, being prone to eutectoid decomposition. They describe two possible forms of magnesia-*partially-stabilised-zirconia*: The first is a cubic zirconia ceramic with subordinate levels of tetragonal phase, converted to monoclinic on cooling. (The volume expansion associated with this transformation offsets the large thermal contraction of the cubic phase on cooling, improving thermal shock resistance). The second is a cubic zirconia in which metastable tetragonal precipitates are retained to room temperatures, transforming with stress-triggers, to produce toughening effects.

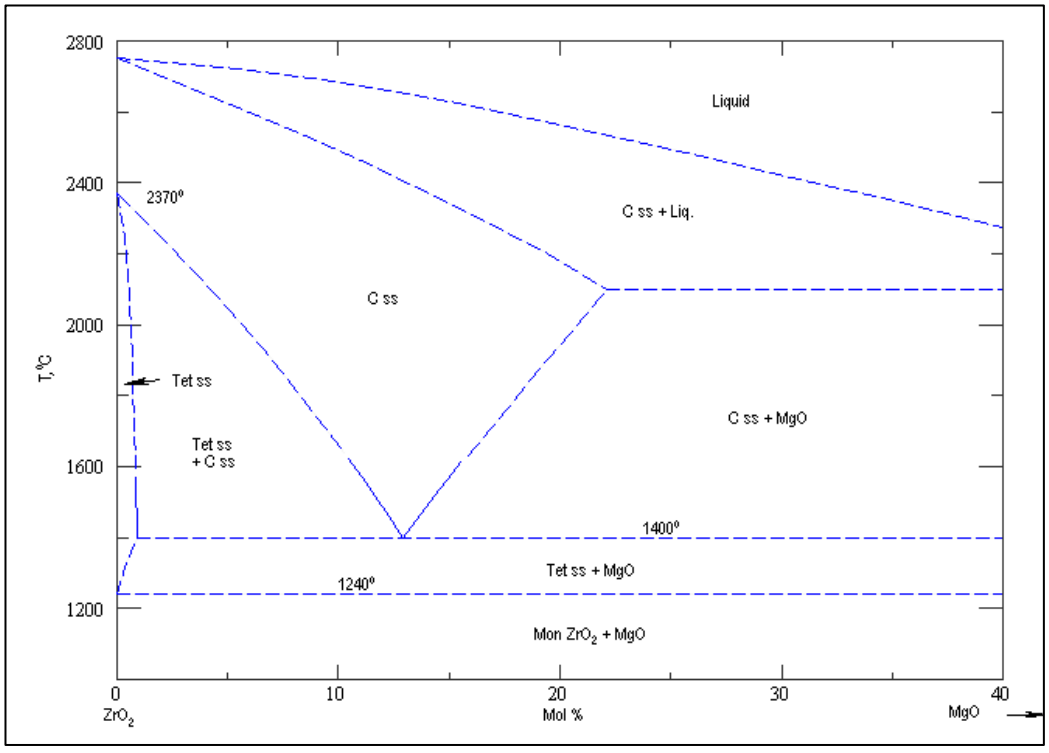

Figure 3 : Phase diagram for Mg-PSZ, developed by Grain[35]. C_{ss} - cubic solid solution; Tet_{ss} - tetragonal solid solution; Mon - monoclinic. Image downloaded from American Ceramic Society-NIST digital database[36].

Multiple permutations of zirconia phase combination, as well as various precipitate forms, are possible, depending on the rate at which, and length of time over which, cooling occurs after sintering / annealing and whether these 'ageing' processes are encouraged before or after the eutectoid temperature of ±1400 °C. Using Transmission Electron Microscopy (TEM), and logical interpretations of the phase diagram developed for the zirconia-magnesia system by Grain[35] (Fig. 3), an understanding of the microstructural evolution of Mg-PSZ ceramics has developed over five decades. It can be broadly summarised as follows :

- At temperatures significantly above the eutectoid temperature (i.e. >1400 °C) a fired zirconia, predominantly cubic, will age and transform to a cubic + tetragonal combination, with the tetragonal precipitates distributed homogeneously and coherently *within* cubic grains. These ellipsoidal (aspect ratio 5:1) tetragonal precipitates (termed 'primary'[37]) may grow to constitute 40-50% of the volume[38] of the ceramic and after several hours of coarsening, spontaneously convert to monoclinic form as coherency with the cubic host is lost[39]. Some tetragonal particles form monoclinic twins, absorbing strain energy this way, but raising interfacial energies. The offset between these energies determines the grain size at which transformation occurs[17]. Hughan and Hannink[37] record multiple forms of pro-eutectoid precipitate with 'large random precipitates' also observed at sites of lattice heterogeneity such as pores, grain boundaries (Fig. 4).

- Close to eutectoid temperatures, cubic grains may age to cubic + tetragonal combinations where the tetragonal phase remains metastable as cooling proceeds all the way to room temperature, or the cubic grains may transform to a combination of tetragonal phase with discreet MgO. The latter is effectively a eutectoid decomposition reaction (Fig. 5), initiating along cubic grain boundaries and with ageing, the tetragonal transforms again to monoclinic. Below the eutectoid temperature (at ±1200-1300 C°) decomposition may produce either a tetragonal+MgO or monoclinic+MgO combination. The cubic host is consumed gradually by eutectoid products with MgO inclusions observed in the monoclinic phase[34]. Volatilisation of the MgO near surface can produce a compressive surface region from the tetragonal-monoclinic transformation that is triggered by this loss of stabiliser. There appears to be some disagreement as to the temperature at which stabiliser sublimation can occur with Heuer and Schoenlein[40]

noting this behaviour just above 1400 °C while Bocanegra-Bernal and de la Torre[38] maintain a minimum temperature of 2000 °C is required.

Figure 4 : Large random precipitates are often associated with lattice discontinuities such as pores. Image reproduced, with permission, from Hughan and Hannink[37]. Scalebar is 5 µm.

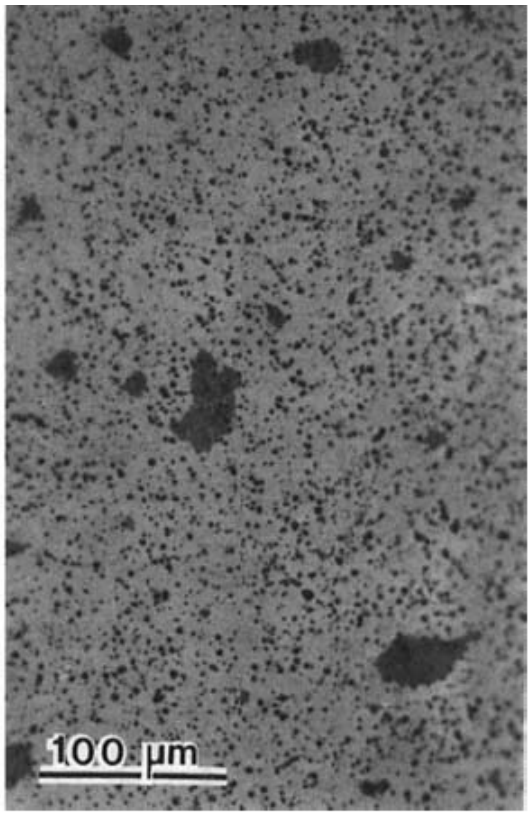

Figure 5 : Eutectoid decomposition is 95% complete in this image, reproduced with permission from Farmer *et al.*[41]. The remnant cubic-tetragonal host is still visible in the random, dark patches. The remaining material represents eutectoid product.

- At very low temperatures (<850 °C), Mg-Zr ion diffusion exchange is no longer possible and no further decomposition occurs. Ageing Mg-PSZ at the other extreme (> 1600 °C) produces extensive grain boundary precipitation, seriously corroding strength[34].

The narrative above does not take into account one further variable, which is the degree of stabiliser doping. For example, if a rapid cooling route is followed for Mg-PSZs with MgO concentrations close to the eutectoid composition (±13 mol%; Fig. 3), metastable tetragonal precipitates with lattice geometry similar to cubic can be produced which do not transform, even under stress at room temperature, because of nanometre-scale domain orientations[6]. In partially stabilised zirconias (PSZ's), concentration gradients of the stabiliser are often present due to the production process, and decomposition of cubic phases further exacerbates local stabiliser heterogeneity. The profile in local stabiliser concentration leads to a continuum of tetragonal to cubic modification and the coexistence of zirconia domains with different degrees of tetragonality, making accurate phase identification and quantification extremely difficult[42]. High temperature, coexisting cubic and tetragonal phases display non-stoichiometry with respect to the oxygen deficiencies created to charge-balance the lattice, when Mg^{2+} substitutes for Zr^{4+}. However, the monoclinic forms at lower temperatures are always stoichiometric.

The microstructural variations created by different ageing processes or stabiliser levels give rise to differences in mechanical properties of the Mg-PSZ ceramics. Annealing at very high temperatures (>1800 °C) has been shown to almost halve as-fired strengths and toughness values[34]. Lower temperature ageing (around 1100 °C) is found to produce improved toughening and crack resistance curves[38]. Thus Mg-PSZ manufacture is significantly empirical, aimed at tweaking microstructure to enhance service performance.

2.1.2. Reheating effects in Mg-PSZ

During service, a variety of processes involving movement of the Mg^{2+} ion are anticipated to further modify microstructure. First, if reheated to temperatures around 1100°C, short range ordering of the oxygen vacancies may be accompanied by formation of a rhombohedral ($Mg_2Zr_5O_{12}$) delta phase[43] at the cubic-tetragonal precipitate interface, with a corresponding increase in the coherence misfit of cubic-delta vs cubic-tetragonal phases[44]. This is a stabiliser concentration-driven reaction, with no real interface. Second, at slightly higher temperatures

(1240-1420°C), continued subeutectoid ageing is expected to produce discreet MgO phases as cubic zirconia decomposes metastably to tetragonal, and stably to monoclinic, forms. Farmer *et al.*[41] interpret this to be an interface diffusion-driven reaction demonstrating that mass transport calculations fit better with this model than bulk diffusion, as cation kinetics are "sluggish". Chaim and Brandon[44] maintain that decomposition above 1200 °C is due to cation diffusion. This does not appear to be a real disagreement but rather the product of a more in depth examination of the mechanism by Farmer *et al.* Decomposition products grow co-operatively with a uniform orientation. The MgO manifests as rods and ribbons, the linear features sometimes disrupted by subsequent Mg^{2+} diffusion or occasionally interconnected along planar faults or rounded with longer ageing times.

In a seminal study, Abe *et al*.[45] experimented with 68 thermal cycles to 1217 °C on a 9.7 mol% Mg-PSZ ceramic and monitored linear thermal expansion to understand *compositional* evolution. Inflections in the dilatometry curves were used to calculate peak transformation temperatures for the m-t and t-m changes in their microstructure and two transformation events were observed: at low numbers of thermal cycles, a low temperature transformation event (m-t ± 657 °C and t-m ± 277°C) was attributed to t-precipitates that had coarsened beyond a stable grain size. From approximately ten cycles onwards, a higher temperature event (average m-t at 1102 °C and t-m at 827°C) was conclusively linked to the transformation of t- and m-phases arising from decomposition with repeated processing of the Mg-PSZ. TEM analysis revealed Mg-rich phases in a MgO-poor monoclinic matrix after 68 cycles, the monoclinic attribution coming from clear bulk XRD results in which no cubic or tetragonal peaks occur. Importantly, they were able to demonstrate that the high temperature transformation event moves to even higher temperatures with increased thermal cycling. This was interpreted to be the result of i) increased stabilisation of the monoclinic phase as repeated cycling produces ever more microcracks (which accommodate the volume increase of transformation and therefore act as preferred nucleation sites), or ii) reducing concentrations of stabiliser in the matrix as decomposition places more and more of the MgO stabiliser in discreet MgO phases.

2.1.3. Zirconia and the MgO-Al_2O_3-SiO_2 (MAS) system

Published data on *fused* Mg-PSZ aggregates (as opposed to the sintered Mg-PSZ ceramics discussed above) are extremely scarce. These aggregates retain silica and alumina impurities after fusion, with the former less of an issue due to silica's higher volatility[46] [47]. There arises the possibility of these trace elements scavenging the Mg^{2+} to form Mg-Al-Si rich secondary phases at areas of discontinuity within the substrate. A study on zirconia-graphite refractories[48] used in continuous steel casting was therefore of interest. These refractories contain fused Ca-PSZ aggregates which were found to develop a Ca-Al-Si rich glassy phase in their centres when located close to working surfaces. Since this secondary phase could not be directly linked to slag composition or penetration, the authors, somewhat at a loss, finally attributed the modification to the entry of "foreign materials". This study did not explore the likelihood of the secondary phase arising from exsolution of impurities within the aggregate material itself. (In contrast, Hino and coworkers[49] [50]were able to explain the evolution of SiO_2-CaO-Al_2O_3 melts in particles of heat treated high-alumina refractory brick using thermodyanamic simulation. Assuming attainment of equilibrium, liquid phase ratios reached 4.6% above 1185°C.)

The impact of interactions between alumina, silica, magnesia and zirconia in the ceramic environment can be gleaned from various angles. Electrical resistivity investigations at the grain boundaries of solid electrolyte yttria-stabilised zirconias doped with alumina, show that alumina segregates strongly to grain boundaries, scavenging impurities such as silica and modifying the density of oxygen vacancies[51]. While evaluating the use of alumina as a sintering aid for yttria-stabilised zirconias, Butler and Drennan[52] confirm, through a thermodynamic exercise, that silica prefers to react with alumina over zirconia in the ZrO_2-Al_2O_2-SiO_2 system. Alumina additives are also used in zirconia manufacturing to improve the fracture toughness of Mg-PSZ ceramics, by scavenging magnesia to form spinel. The accompanying volume increase produces microcracks which supercede those produced from martensitic transformations in terms of energy absorption during crack propagation. This improvement in thermal shock is offset though, by loss of stiffness and strength[53]. The same study notes the tendency of silica to destabilise slip-cast magnesia-stabilised-zirconia by removing the MgO to produce magnesium silicates at grain boundaries. Alumina's solubility in zirconia is limited[54] but alumina is soluble in MgO with up to 10 mol% absorption into periclase documented at temperatures around

1700-1725 °C. The alumina supersaturates during subsequent cooling to recrystalise out as smaller spinel crystals[55].

2.2. Thermomechanical considerations for Mg-PSZ refractories

2.2.1. Fracture mechanics in the field of refractories

Most refractories are exposed to strain-related loads as opposed to gravity-induced stress-related loads[56] i.e. they must withstand thermal stresses, under physical constraint, without failing. Since their microstructures are, by definition, full of flaws (pores), crack initiation is less of an issue than crack propagation. To understand the latter, two key engineering relationships are considered : i) the tension between the energy required to drive a crack (stored elastic strain energy, G) and the energy required to make crack surfaces, which in effect resists crack propagation (surface energy, R) and ii) the balance between strength and toughness. These two relationships are not mutually exclusive but will be discussed as two separate themes here for ease of presentation.

2.2.2. The balance between G and R

A century ago, Griffith presented an energy balance for any ceramic system with a crack (U_c), as an equilibrium between mechanical energy available to drive crack growth (elastic strain and potential energy due to stress loading = U_m) and surface energy (required to break coherent bonds and grow the crack surface = U_s)[57]:

$$U_c = U_m + U_s \tag{1}$$

Irwin extrapolated Griffith's idea and defined a strain energy release rate (G) per unit area of new crack surface (C), with a corresponding resistance force (R) :

$$G = dU_m/dC \qquad \text{and} \qquad R = dU_s/dC \tag{2}$$

When dG/dC exceeds dR/dC, unstable crack growth proceeds. For the reverse situation, stable crack growth occurs[57]. Because the stress-strain curves for loaded ceramics are linear-elastic,

strain build-up leading to crack propagation can be directly related to their bulk stiffness (E, as Young modulus). Thus Irwin showed that :

$$G = \frac{K_I^2}{E} \qquad \text{or} \qquad G = \frac{\pi\sigma^2 C}{E} \tag{3}$$

where K_I represents critical stress intensity and σ failure stress. However, refractories demonstrate non-linearity in their stress-strain behaviour as a result of diffuse damage such as microcracking, and bulk elastic approaches are sometimes less useful than fracture-specific approaches. Nakayama[58] pioneered the latter with development of the term "work-of-fracture" (γ_{WOF}) for the energy expended in stable crack propagation relative to area of fracture surface created.

By the latter half of the twentieth century, Hasselman[59] had linked quasi-stable crack growth (released energy immediately consumed with stepwise crack progress) and kinetic crack growth (unstable / catastrophic failure) to the physical properties of thermal expansion [α], work of fracture [γ_{WOF}], Young modulus [E] and Poisson ratio[υ]. Hasselman defined R_{st} as the minimum thermal gradient at which long stable crack growth would initiate and R"" as the minimum extension from thermal stress, with R_{st} generally applied to quasi-stable crack growth and R"" to kinetic cracking :

$$R"" = \frac{\gamma_{WOF} E}{\sigma^2}(1-\upsilon) \tag{4}$$

$$R_{st} = \left(\frac{\gamma_{WOF}}{\alpha^2 E}\right)^{\frac{1}{2}} \tag{5}$$

Most importantly, Hasselman recognised that crack stability is bounded by two characteristic crack lengths for any thermal shock process[60]. Assuming triaxial stress, constrained boundaries, regularly distributed, rounded Griffith flaws of equal size in the starting ceramic and the simultaneous onset of multiple, radial propagating cracks, Hasselman produced a calculation for final crack length after shock :

$$\ell_f = \left[\frac{3(1-2\upsilon)}{8(1-\upsilon^2)N\ell_0}\right]^{\frac{1}{2}} \tag{6}$$

where N is the number of cracks per unit volume, propagating simultaneously, and ℓ is the crack length. Recently, this ceramic-based model has been modified for refractories. Salvini et al.[61] take account of the interaction between a propagating thermal stress-response crack and the as-fired flaws of a working refractory and using γ_{NBT} to represent the hypothetical energy for crack initiation vs γ_{WOF} for crack propagation, modify Equation 6 to :

$$\ell_f = \left[\left(\frac{\gamma_{NBT}}{\gamma_{WOF}}\right)\frac{3(1-2\upsilon)}{8(1-\upsilon^2)N\ell_0}\right]^{\frac{1}{2}} \quad (7)$$

The recognition that refractory microstructure significantly changes crack behaviour, relative to a purely linear-elastic material is best encapsulated through the concept of an R-curve. Based on work first done by Gogotsi *et al.*[62] in defining the non-linear behaviour of low-strength heterogeneous composites, R-curves were created to demonstrate increasing resistance to crack growth with increasing crack length[63]. Fig. 6 is essentially a scheme reflecting the balance between G and R.

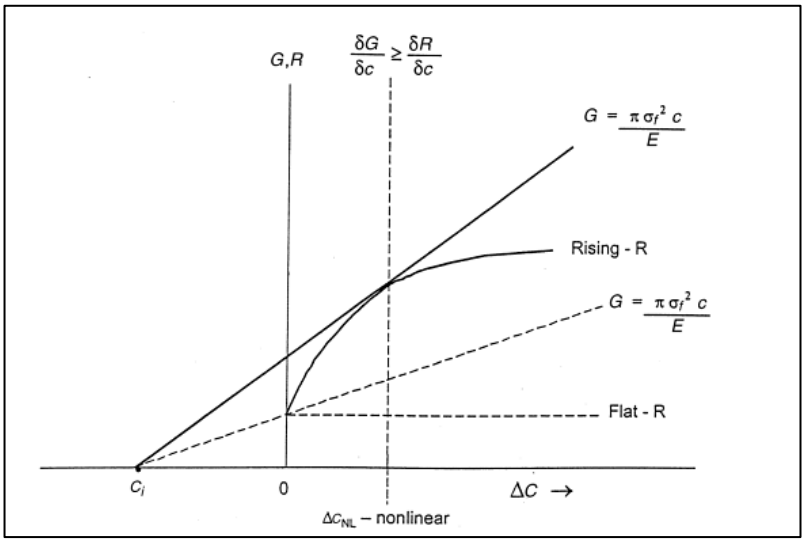

Figure 6: The G vs R relationship associated with rising R-curve behaviour. Reproduced with permission[64].

As strain builds up in a thermally stressed refractory, G increases to the point where a crack begins to extend (c [and C] in Fig. 6 represent crack length). Immediately, the resistance to this extension arises from the energy consumption of not just new surface but the microstructural specifics of the crack tip region and the wake behind the growing crack. R exceeds G and crack growth stops. This process is iterative with the ever-lengthening crack becoming harder and harder to propagate. Eventually, when G equals or exceeds R, failure occurs. Rising R-curve

behaviour is intrinsically linked to microstructures which lend themselves to crack growth resistance[64] i.e. particle-reinforced composites. Increasing size, angularity and surface roughness of aggregates, as well as stronger aggregate-matrix interfaces, all contribute to steeper R-curves.

Since G is dependent on the volume of material under stress and R on the amount of crack surface being created, it is important to link these parameters to dimension. Harmuth and collaborators[65] [66] have done this by defining brittleness, B, in terms of specific fracture energy (G_f) - equal to 2 γ_{WOF} - and based on specimen dimension (L) as :

$$B = \frac{{\sigma_f}^2 L}{G_f E} \tag{8}$$

where the fracture strength (σ_f) and Young modulus (E) are known. For a set of burnt magnesia, magnesia-spinel and magnesia-hercynite brick samples, they found that brittleness was reduced when failure occurred along aggregate-matrix interfaces, as opposed to transgranular fracture, and when the presence of microcracks increased. These experimental findings point to the impact of local heterogeneities surrounding a crack i.e. the crack process zone. At the front of this zone, energy ahead of a growing crack tip can be absorbed by crack deflection, microcracking or microbranching. At the back of the zone, in the wake of the growing crack, energy is consumed by aggregate (or fibre or silicate phase) bridging and the friction associated with pullout of the reinforcement phase. Bradt[9] presents a summary of increasing crack growth energy with crack length, showing that average crystal cleavage energies (10^{-7} J/cm^2) are generally lower than crack initiation energies in Modulus of Rupture (MOR) tests (10^{-6} J/cm^2) which in turn, are much lower than those for total work of fracture in wedge tests (10^{-3} J/cm^2). These data, together with multiple studies showing rising R-curves for long cracks, lend weight to the idea that resistance in the wake of a crack is more efficient than resistance ahead of the crack tip for arresting the propagation of long cracks.

2.2.3. The relationship between strength and fracture toughness in refractories

For a bulk ceramic demonstrating linear stress-strain behaviour, the tensile strength (σ_f) and fracture toughness (K_{IC}) of the material are directly linked as follows :

$$\sigma_f = \frac{3PL}{2bh^2} = K_{IC} Y C^{-1/2} \quad (9)$$

where P is a maximum load on a bar of cross-dimensions b x h, over a span L. Overall geometry is captured through the constant Y and C denotes the critical flaw size for failure[64]. Strength is dictated by extension of a dominant pre-existing flaw at a critical applied stress[67]. In the 1980's it was discovered that for Mg-PSZ ceramics, the relationship between strength and fracture toughness was not a direct correlation however - peak strengths were found to be lower than peak toughnesses, with increasing monoclinic content at test sample surface. Using the equation :

$$\Delta K = \frac{\eta V_f \Delta V E \sqrt{d}}{1-\upsilon} \quad (10)$$

where V_f is the volume fraction of transformable tetragonal phase, ΔV the volume dilation of transformation, E the Young modulus, υ the Poisson ratio and η a constant, Swain[68] demonstrated the linear correlation between increments in toughness (K) and the size of the transformation zone around a crack (d). Then, using the relationship :

$$\sigma = \frac{K}{\sqrt{2\pi d}} \quad (11)$$

Swain showed that the size of the transformation zone could be used to determine the stress at which transformation is initiated. A theory of duality in strength regimes was thus proposed that is summarised in the scheme of Fig. 7. For stresses below a critical stress (σ_c), normal elastic behaviour is observed: strength is dependent on critical flaw size, and high strength is associated with high toughness characteristics. Above this critical stress (and independent of temperature), transformation produces microcracking that begins to limit strength but continues to improve toughness.

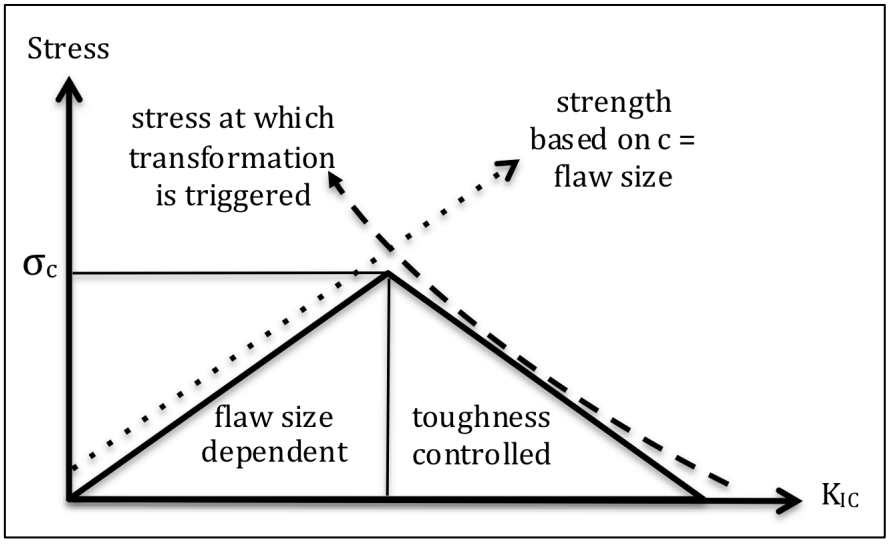

Figure 7 : Simplified summary of Swain's[68] dual strength regime concept.

Marshall[67] builds upon Swain's foundation and highlights the fact that many materials, like Mg-PSZ ceramics, cannot be defined by a single fracture toughness value but rather exhibit the R-curve continuum of increasing toughness with growing crack length. Before fracture (where $G=K_{IC}/E$ touches the R-curve as a tangent in Fig. 8), strength is dependent on the applied stress and the gradient of the R-curve and therefore independent of existing flaws where these are smaller than c_f.

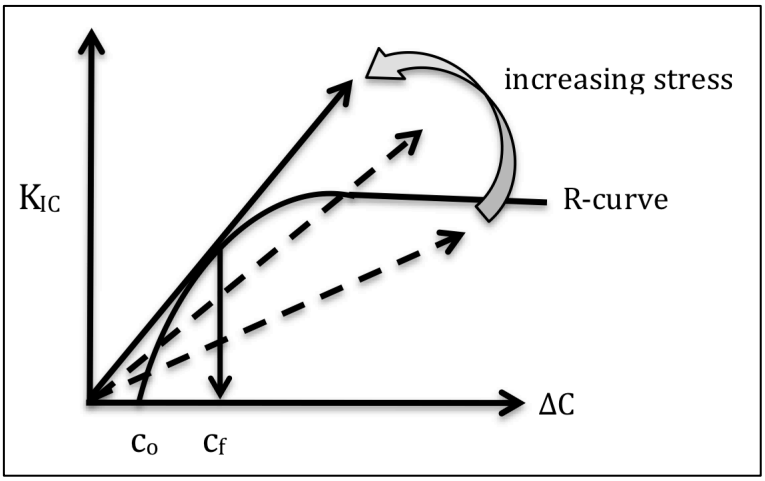

Figure 8 : Simplification of Marshall's[67] link between flaw size and fracture toughness.

The transformation-affected strength-fracture toughness relationship described above for ceramic Mg-PSZ's may be relevant to the aggregate phase of zirconia refractories, where each aggregate could be viewed as a ceramic in isolation. However, refractories have other toughening mechanisms as mentioned. For many refractories, the relationship between

strength and fracture toughness *is* linear, with the slope value of this trend directly comparable to aggregate size[64]. Aggregates are central to the mechanics of refractory failure.

Ribeiro and Rodrigues[69] examined two alumina castable refractories with aggregates of similar composition but different size profiles. The coarser (>0.0108 mm) aggregate sample was shown to demonstrate maximum load strengths and fracture energies of more than double that of the finer (<0.0108 mm) aggregate sample for constant sintering temperatures of formation and almost equal volumes of aggregate (64% vs 67%). The increased fracture energy also correlated with increasing brittleness, supporting the idea that the fracture energy highs were due to strength, not toughening mechanisms. There is thus some evidence within the refractory, as opposed to ceramic, literature for a decoupling of the strength-toughness correlation.

2.2.4. Thermal shock resistance

In the refractory literature, the concept of thermal shock is defined quite broadly from subjecting a material to immediate, large changes in temperature (e.g. quenching) to the outcome of routine thermal cycling during service. Damhof et al.[70] stress the importance of differentiating between damage done due to sudden changes in temperature as opposed to exposure to high temperatures. Both will be considered here. In addition, low-level environmental degradation (usually linked to the presence of moisture[71]) may further modify materials, after shock or cycling, resulting in phenomena such as loss of strength.

In terms of refractory evolution over multiple thermal cycles, Boccacini *et al*.'s[72] evaluation of mechanical resilience *post* cycling can be contrasted with Luz *et al*.'s[73] investigation on mechanical modification *within* thermal cycles. Boccaccini *et al*.[74] define thermal shock resistance in terms of the number of industrial cycles a refractory withstands when subjected to *sudden* temperature change. However, in a comparative study on thermal shock damage in two cordierite-mullite refractories[72] (with large and small aggregates respectively), they quantify loss of mechanical performance over multiple service cycles to 1275 °C at heating and cooling rates of 15 °C/min - not plausibly a sudden temperature change. Their experiments indicate higher frequency microcrack interaction leads to a loss of strength, early large crack initiation and slow crack propagation towards failure. In contrast, where a high density of microcracks occurs but without these microcracks interacting, the refractory experiences loss

of stiffness with increased thermal cycling, leading to delayed but rapid fracture. These observations are aligned with average aggregate size, with the premise advanced that larger aggregates produce greater microcrack interaction than smaller aggregates. Evidence for this link between aggregate size and microcrack density is not strongly presented in their data. However, this study represents a rare attempt to *quantitatively* link aggregate size and mechanical performance in the refractory literature. The overall conclusion - that high densities of microcracks increase cycling resilience through stiffness reduction (R = strength/stiffness) and extensive microcrack connectivity drops cycling resilience through strength reduction - appears useful for application in the present study.

Luz *et al*.[73] also consider the strength-stiffness relationship in a set of alumina- and mullite-based castable refractories with sintering additives, tested to 800 °C over ten cycles. Like Boccaccini et al.[72], they use a non-destructive resonance technique to determine stiffness, but record this data for the duration of the heating and cooling cycles so that they are able to differentiate between interim stiffness increases (due to the rise in liquid phase viscosity on cooling), interim stiffness losses (due to the advent of thermal mismatch microcracks after two cycles), permanent stiffness increases (due to densification on first cycle), permanent stiffness conservation (due to conversion of liquid phases to new crystal compounds) and permanent stiffness losses (due to irreversible microcrack damage). This type of analysis allows for a far more rigorous interpretation of the final room temperature stiffness values, post cycling, as the material's history and phase evolution is taken into consideration.

The damage done during thermal cycling is not necessarily unwanted. In some instances, microstructural damage is specifically engineered in, in order to promote improved toughness. Huger et al.[28] use the term 'flexibility' for refractories with enhanced "aptitude for strain". They demonstrate that for aluminium titanate ceramic composites with large grains and associated large microcracks, bending strength losses (-10%) are lower than for similar samples with smaller grains and correspondingly smaller microcracks (-25%) after water quenches from 1000 °C. In a second experiment, an andalusite castable is shown to increase its strain-to-rupture due to microstructural damage arising from the thermal mismatch between its aggregate and matrix phases.

Aneziris et al.[53] doped a Mg-PSZ slip with pure alumina to produce a sintered product that was tested for thermal damage resistance. The alumina was found to scavenge the stabiliser Mg ions, producing $MgAl_2O_4$ spinel above 1000 °C. In this reaction, a volume change of 5% resulted in microcracks that dropped stiffness and increased strength and fracture toughness. Loss of stabiliser markedly increased the proportion of monoclinic in the material, reducing the thermal expansion coefficient of the modified Mg-PSZ. While the authors attribute catastrophic failure of the material to thermal hysteresis, it is in fact the increased volume of monoclinic, available for polymorphic transformation on cycling, and the consequent increased transformation strain, that is likely to have triggered fracture.

2.2.5. What cement and concrete studies tell us about composites

As mentioned in the section above, published quantitative data on the link between aggregate and flaw size in particle-reinforced refractories is scarce, despite the universally stated premise that the former determines the latter. It is equally challenging to find data comparing the impact of aggregate strength with aggregate-matrix-interface strength, for the purposes of interpreting bulk mechanical performance of such refractories. The cement and concrete approach to failure analysis of particulate composites is therefore illuminating. In a study comparing small (<8 mm) and large (<16mm) lime and gravel aggregate concretes, the strength of the large aggregate concrete for each aggregate type was shown to be 11-15% higher than that of the corresponding smaller aggregate population[75]. Crack development was traced from microcracks (pores adjacent to aggregates) to mesocracks (the full length of a straight boundary on an aggregate) to wing-cracks (straight cracks with end deflections), specifically linked to large aggregates or propagating through matrix alone. Another study looking at the microcracks arising from aggregate restrained shrinkage of the cement, demonstrated that permeability for the coarse aggregate sample (<12.7mm) was 1.5 orders of magnitude in excess of that for the finer aggregate sample (<5mm), because the microcracks produced by the larger aggregates were shorter but wider - width being the determining factor for permeability[76]. Finally, in a comprehensive exercise of modified aggregate-matrix interface samples of concrete, Guinea *et al*.[77], highlights the role of aggregate shape and its impact on interface strength : crushed aggregates (i.e. angular grains) yield higher fracture energies than spherical aggregates, irrespective of interface type (enhanced with silica fume or epoxy or degraded with paraffin or bitumen), due to the role of interlock where friction is created

between the rough crack surfaces after aggregate pullout. Brittleness is shown to increase with increasing interface strength.

3.1. Three commercial Mg-PSZ refractories

The materials forming the basis for this project comprise three commercial Mg-PSZ products. They are refractories, fired as crucible shapes with rounded bases and curved upper rims (Fig. 9), used in small charge (±4kg) vacuum induction furnaces. The crucibles are utilised for melting nickel-cobalt alloys and can be used at service temperatures of approximately 1500-2400 °C[78]. All three refractories are manufactured by firing fused zirconia aggregates with fused zirconia matrix particles at temperatures around 1600 °C, in a method analogous to that used to create the rebonded fused-grain magnesia-chrome bricks of the 1960's[3]. The aggregates and matrix particles, where both are stabilised, represent coarse (>0.15mm) and fine (<0.15mm) screen fractions of the same fused source material.

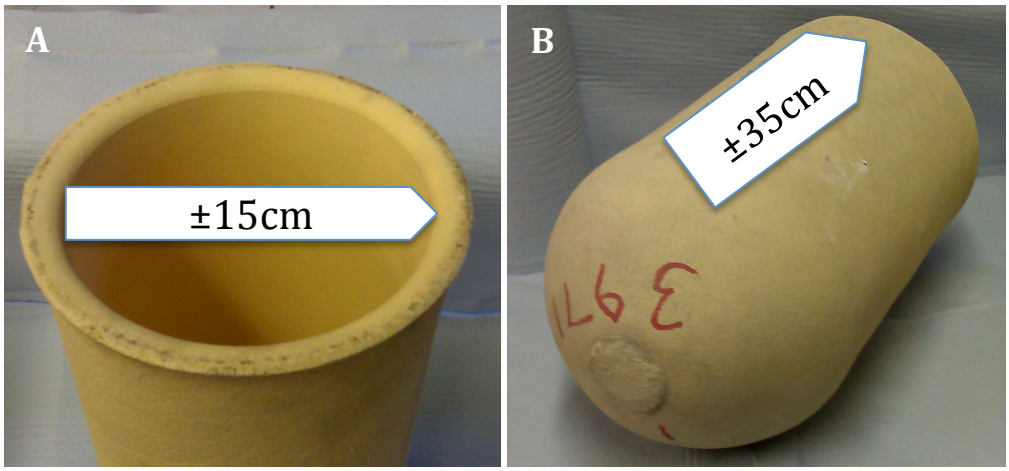

Figure 9 : VIM crucibles comprising fused Mg-PSZ aggregates with fused zirconia matrix. Wall thicknesses are approximately 13mm.

Fused Mg-PSZ aggregates are created in a process involving two fusion steps. First, zircon sand is carbothermally reduced with coke, to zirconia, using an electric arc furnace operated to ±2700 °C. This process does not expel all impurities and in particular, traces of iron, alumina and silica remain[79]. Silica is more volatile than alumina and the former is therefore likely to occur in lower concentrations in the final product[46]. Challenges in the removal of alumina are attributed to the compound being bound in a kyanite phase within the sand[80]. After fusion, the cooled material is blown through air to spherulise it, creating what is nominally baddeleyite but in fact often metastable cubic zirconia, given the speed of cooling[46]. In the second major

process step, zirconia is re-fused, together with high purity magnesia, at 2700-3000 °C, to form a multi-ton ingot in a Higgins furnace. This ingot is slow cooled, yielding crystals of 5-6 cm size which are crushed and sieved to final fractions. Although homogeneity is intended, local magnesium gradients do arise[42].

The three refractories used in this study have been designated 'LP' (for low pressure), 'HP' (for high pressure) and 'SA' (for small aggregates) in order to highlight their key manufacturing differences. Supplier information, which excluded particle sizes, is as follows:

- Sample LP: fused Mg-PSZ aggregates are mixed with fused monoclinic zirconia fines, magnesia fines (to increase the magnesia content of the refractory overall) and a small proportion (±2%) of clay as plasticiser. The green body, formed with a paste binder (mixture of aqueous polymer dispersion, wax emulsion and methylcellulose powder), is cold isostatically pressed at 70 MPa before firing. Supplier datasheets[78] indicate a bulk density of 4.35 g.cm^{-3} and an apparent porosity of 22% with representative composition of 92.5 wt% ZrO_2+HfO_2, 4.6 wt% MgO, 0.15 wt% CaO, 1.5 wt% SiO_2 and <0.15 wt% Fe_2O_3.

- Sample HP: fused Mg-PSZ aggregates are mixed with fused monoclinic zirconia fines (no magnesia fines) and a small proportion (<2%) of clay as plasticiser. The green body, formed with a liquid binder (aqueous polymer dispersion and non-ionic wax dispersion), is cold isostatically pressed at 207 MPa before firing. Supplier datasheets indicate a bulk density of 4.3-4.5 g.cm^{-3} and an apparent porosity of 20-23% with representative composition of 95.2 wt% ZrO_2+HfO_2, 2.71 wt% MgO, 0.17 wt% CaO, 0.74 wt% SiO_2 , 0.56 wt% Al_2O_3 and 0.07 wt% Fe_2O_3[78].

- Sample SA: fused monoclinic zirconia aggregates are mixed with fused Mg-PSZ fines i.e. the phase assemblage of aggregate and matrix is inverted, relative to the two samples above. Binder and pressing details are unknown.

A set of loose Mg-PSZ aggregates of similar grain size range and chemistry to the aggregates in samples LP and HP were also included as test materials in the project. These loose aggregates are understood to be similar in provenance to those within the test refractories and represent likely raw materials used in the manufacture of LP and HP.

3.2. Characterisation methods for microstructure and composition

Sample *microstructure* was evaluated in terms of morphology using SEM. Semi-quantitative analysis and quantitative compositional analysis was undertaken to enable interpretation of the morphology in light of chemical variations and phase transformations. The techniques utilised included SEM-EDS, SEM-WDS and XRD. Microstructural mapping of mineral phases was carried out using Raman confocal microscopy. Thermodynamic modeling was applied to as-fired aggregate SEM-WDS data, using commercial software, in order to evaluate liquid segregation at service temperatures.

Bars of the three sample materials (25 x 8 x 8 mm) as well as several grams of loose aggregate were heated in an elevator hearth furnace from room temperature to 1750 °C at heating rates of 20°C/min (to 1000 °C) and 10°C/min (to1750 °C), and allowed to cool naturally before the cycle was repeated. Eight thermal cycles were completed in air before sectioning and SEM analysis. The target temperature was set to 1750 °C without a soak or dwell period at this maximum. Allowing for a lag time to full temperature equilibration within the material, the aim was to ensure a real sample temperature of at least 1700 °C for further data interpretation. All SEM-based work was undertaken on clear epoxy-mounted sections, finished to a 3 μm diamond finish and gold-coated.

3.2.1. Scanning electron microscopy (SEM) with image analysis

Refractories offer a high degree of heterogeneity in their microstructures. Use of a routine linear intercept technique is therefore not as suitable for measuring grain sizes as it would be for a dense, polycrystalline ceramic. Within the earth science community, novel image analysis techniques have been pioneered for particle measurement in highly non-uniform microstructures[81 82 83]. A similar approach was adopted here. For each of the three refractory samples, a sequence of adjacent backscattered electron image (BEI) was captured by moving the mounted section through fixed 1.5-2mm intervals under a JEOL JSM5610 SEM (20kV accelerating voltage and 14-16 mm working distance). All images were acquired using a standard magnification of 50x.

The choice of magnification was important because the images must be representative of the material and can alter the size-frequency population result if magnification is too high (large grains being scarce in fields of view) or too low (small grains not being resolvable)[81]. Among other factors that may affect whether grain size results using image analysis are representative, the most important is number of specimens analysed (as opposed to number of fields of view per specimen[84]). Given the labour-intensive method employed here, multiple specimens were not considered however.

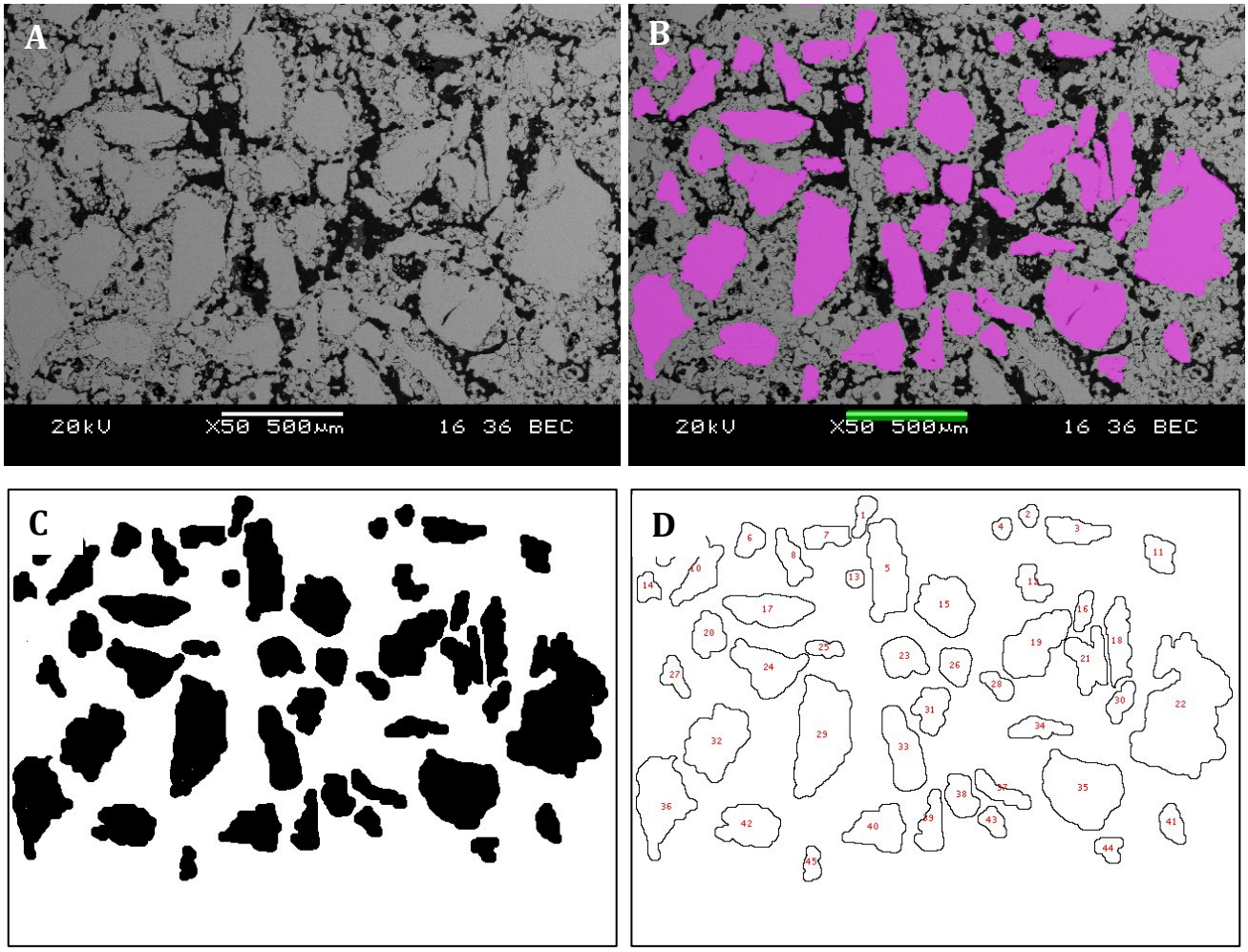

Figure 10 : Example of process used to trace aggregates in SEM (Backscattered electron) images to determine grain size. A - Backscattered electron image at standardised magnification; B - Aggregates traced using transparent cover layer; C - Traced layer removed and converted to binary image; D - Binary image processed for particle size analysis.

A minimum of 300 grains per refractory was aimed for, to ensure statistical viability. Roebuck[85] suggests that at least 300 intercept lengths should be squared to obtain area estimates if area is not measured directly. Muirhead et al.[84] suggest 400 grains for the linear intercept method, to obtain a relative accuracy of 10%. The BEI images (640x480 pixels) were

processed as shown in Fig. 10. Each image was covered by a transparent layer in the GNU Image Manipulation Programme (GIMP)[86] and all aggregates not truncated by the image border were digitally traced. The traced layer was saved as a new jpeg image file, imported into ImageJ[87], converted to an 8-bit picture, subjected to a contrast threshold to produce a black and white image and saved as a binary image file.

The latter was analysed with a particle analysis algorithm[88] which produced a map of grain outlines for all particles larger than 20 pixels and a text file of measured grain areas. Data were graphed in Microsoft Excel using the Statsplus histogram binning plugin. To capture detail in the finer grain sizes and still include the rare, very large grain, the histogram bins were created in a natural log style i.e. doubling of size in each successive bin of cross-sectional area using the following : <0.005; 0.005-0.01; 0.01-0.02; 0.02-0.04; 0.04-0.08; 0.08-0.16; 0.16-0.32; 0.32-0.64; 0.64-1.28; >1.28 (mm^2).

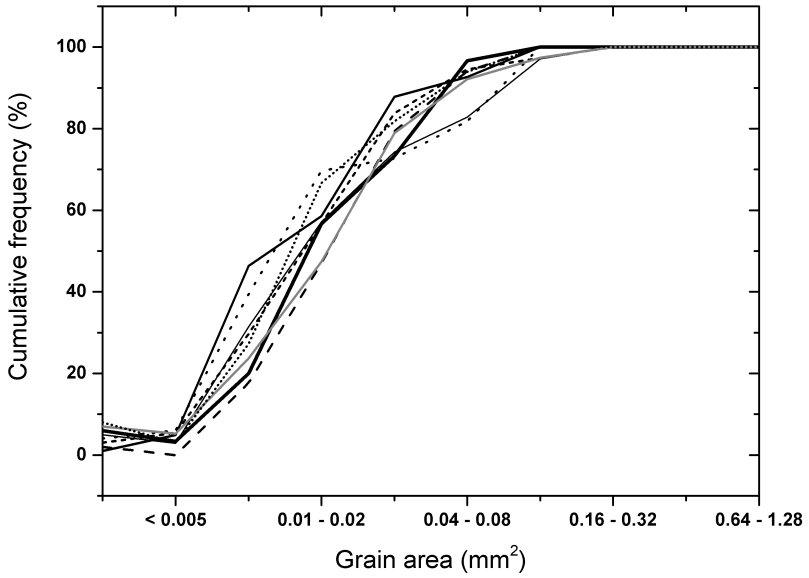

Figure 11 : Data per field of view for eight fields of view across sample HP.

To establish reliability for the technique, one sample was selected (HP) and a cumulative frequency curve generated for each of the eight fields of view used in the grain size analysis (Fig. 11). Although there is up to 50% frequency variation within an individual size bin, the trend across size bins is consistent. Lateral variations in the eight curves indicate that the maximum displacement is one bin size to left or right in the range of eight bins occupied. The method is therefore not rigorously accurate for a size category but is precise (repeatable) in terms of producing a population profile.

3.2.2. Scanning electron microscopy with energy dispersive spectroscopy (SEM-EDS)

Mounted sections of the as-fired and cycled samples (pre- and post-cycling) were imaged using a JEOL JSM5610 or JSM6400 SEM, or FEI Auriga SEM at 20 kV and working distance of ±15mm. Semi-quantitative analyses were undertaken with EDS using a polished, pure cobalt standard to ensure accurate peak positioning only. Standardless EDS does not calibrate the sample result against a standard. It uses only beam energy information to extrapolate - by basic physics principles - equivalent standard intensities. Oxygen stoichiometries are assumed and generally the practice requires automatic normalisation to 100%. Newbury[89] warns that standardless analysis techniques generate a 25% relative error. For SEM-EDS carried out in this project, oxygen stoichiometry assumptions were retained (due to the oxide nature of the materials) but normalisation was excluded so that only relative proportions of elements identified constituted the result for interpretation.

3.2.3. Scanning electron microscopy with wave dispersive spectroscopy (SEM-WDS)

Quantitative element analyses were obtained using a Cameca SX100 instrument with WDS, an accelerating voltage of 20kV and SEM imaging to ensure a spatial resolution between analysis points of approximately 2μm. A combination of synthetic and natural matrix-matched standards from the Natural History Museum collection (London) was used (Table 1) and a ZAF matrix correction applied (see below).

Table 1: Mineral standards used at the Natural History Museum, London, for quantitative EPMA analysis.

Analyte and NHM Standard used	**Composition of Standard (wt%)**
Mg (STD 277: Forsterite)	O: 45.48, Mg: 34.55, Si: 19.98
Al (STD 028: Corundum)	O: 47.0758, Al: 52.9242
Si (STD 097: Wollastonite)	O: 41.04, Si: 23.8, Ca: 34.16, Fe: 0.6, Mn: 0.05
Zr (STD 100: Zirconia)	O: 34.86, Zr: 49.1, Si: 15.15, Hf: 0.89
Hf (STD182: HF3)	Hf: 97, Zr: 3

Quantitative SEM-WDS (also known as electron probe microanalysis or EPMA) is based on the concept of 'zero order conditions' so that only composition is affecting the measured X-ray, and not surface factors[89]. The same X-ray peak is analysed for sample and standard under constant conditions of beam energy, dose (beam current+time), spectrometer setting and X-ray take-off angle. A ratio of intensities from the sample and standard is converted to accurate compositional information, once matrix corrections have been applied, using one of two

common software algorithms (commonly known as ZAF or PAP). These algorithms correct for atomic number (Z), heavier elements have higher numbers of electrons backscattering instead of generating diffracted X-rays, absorption of X-rays by the sample (A) and fluorescence effects (F). EPMA is capable of very narrow error distributions: using element standards, 95% of results should fall within ±5% relative error margins[90].

3.2.4. Transmission electron microscopy (TEM)

Using a Helios NanoLab600 with a focused Ga ion beam (FIB), a thin foil sample (±150 nm thickness) was extracted from an LP aggregate subgrain adjacent to its secondary phase boundary (Fig. 12).

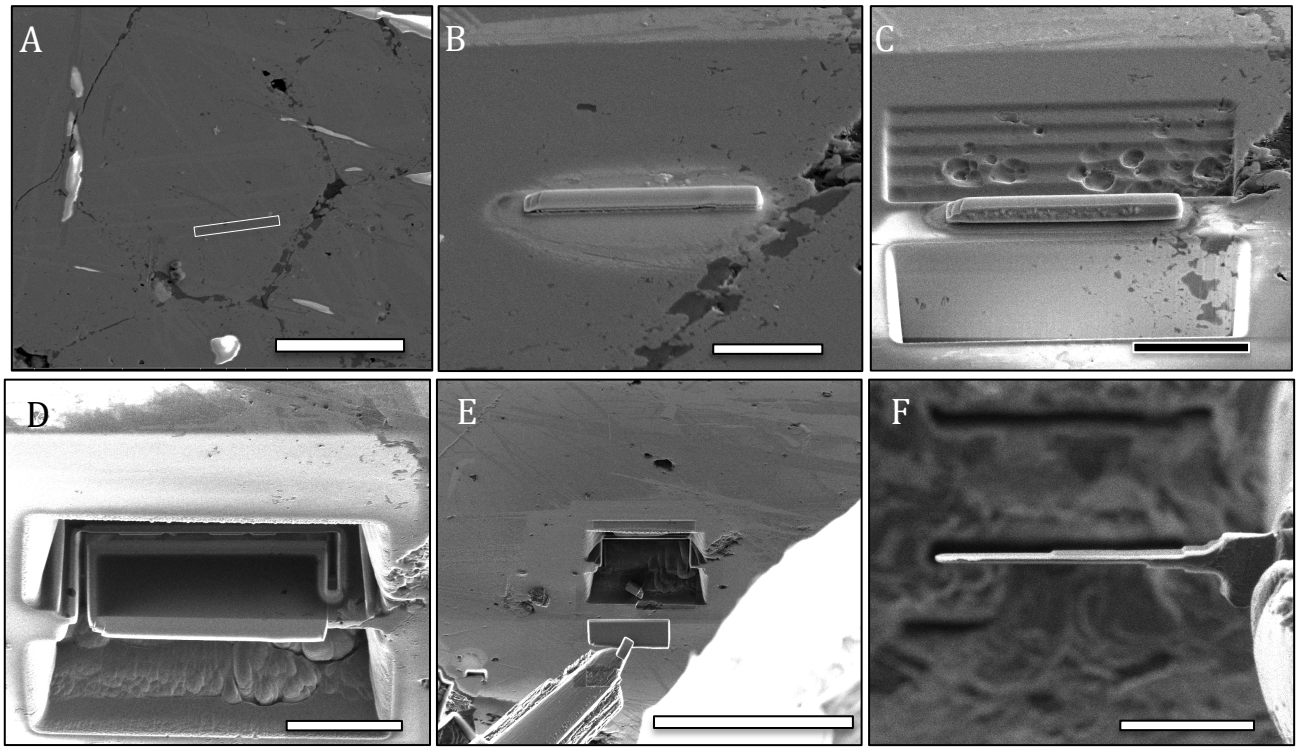

Figure 12 : A- Contextual image for the thin foil extracted adjacent to a subgrain boundary within a cycled LP aggregate; B - A platinum cap is laid down to define the top boundary of the foil. C - Stepwise stripping of material from a distance away, towards the centre of the foil, is undertaken. (The geometry of the domain boundary is visible at depth, along with considerable porosity.) D - The foil section is tilted to cut three sides before needle attachment. E - A platinum needle is attached, the last foil edge severed and the foil removed. F - The foil is attached to a copper holder and thinned repeatedly to produce a stepped cross-section, offering structural robustness. Scalebars from A-F : 40 µm, 10 µm, 10 µm, 10 µm, 50 µm, 5 µm.

A selected area electron diffraction (SAED) pattern was obtained for this foil by TEM, using a FEI Titan 80/300 at 200 kV. Figure 13 provides a simplified overview of the apertures and lenses in the column of a TEM[91]. Thin foil samples are inserted in the objective lens which yields low magnifications (±50x), first stage images and the electron diffraction pattern. The

latter is focused on the back focal plane of the objective lens. A goniometer is used to tilt the sample between 10% and 60%. The area to be analysed for diffraction is selected by inserting a selected area aperture into the plane of the intermediate image. For a thin crystalline sample, electron diffraction can be captured from lattice planes close to the Bragg angle of incidence (cf. Section 3.2.5). The sample is tilted until partial grain blackout indicates that the electron beam is parallel to a zone axis and at this point, a diffraction dot pattern should be visible. Once the diffraction pattern has been acquired on the fluorescent screen, the latter can be removed to allow digital image capture[8].

Dot spacings within a SAED represent the reciprocal lattice of the crystal being analysed. This reciprocal lattice is captured as an Ewald sphere - an artificial construct used to indicate where the scattering vector will lie, if the wave planes incident on, and diffracted from, a crystal lattice are equal[92]. The d spacings of crystal planes and by extrapolation, the unit cell parameters, of the analysed crystal can thus be determined.

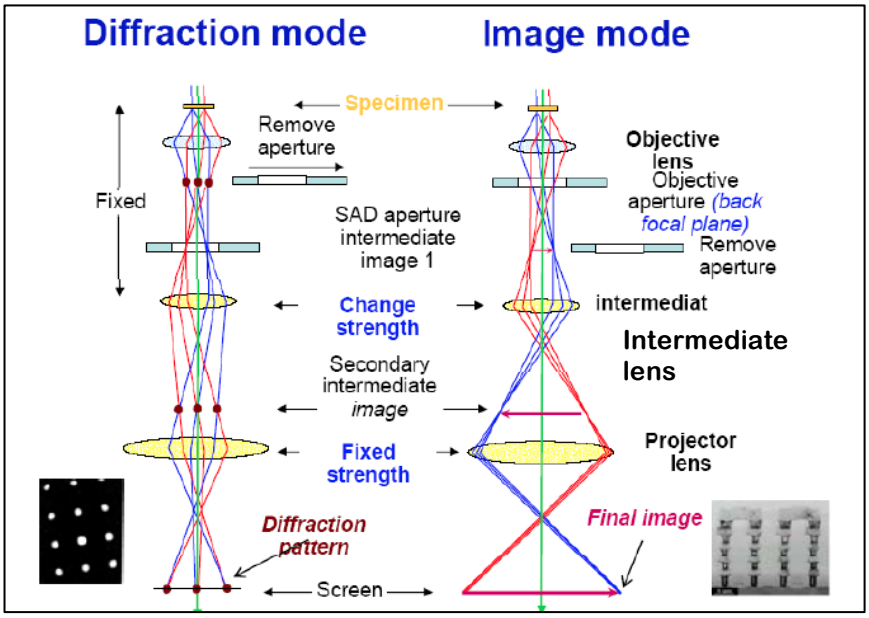

Figure 13 : Overview of TEM components relevant to diffraction and imaging applications. Reproduced, with permission, from Botta[91].

3.2.5. X-ray diffraction (XRD)

Five samples comprising solid segments approximately 3mm in thickness with parallel sides were run on a Panalytical X'Pert Pro X-Ray Diffractometer, using a Cu-K_α source at 40 kV and 40mA. Scan speed was 20 seconds per step and step size was set to 0.02° over the 2θ range of

10° to 100° (equating to a scan speed of 0.1078°/sec). These settings were based on the XRD experimental set up reported by Pittayachawan[93] for analysis of dental zirconia and to ensure information was obtained over two regions of interest (26-36° and 71-76° 2θ). Beam penetration depth was assumed to be in the region of 5 microns. Acquired spectra were processed in Panalytical's X'Pert Plus software to allow background subtraction (after Sonneveld and Visser[94]), peak search and match, and comparison against international database standards.

This well known technique makes use of the fact that crystalline materials can act as diffraction gratings for electromagnetic waves of wavelength similar in size to the d-spacings between the crystal lattice planes. If the wavelength (λ) of an incident X-ray beam is known - for this project, Cu Kα (1.5406 Å) - a scan across all incident angles (Θ, theta) of the beam directed at the sample should reveal those d-spacings producing constructive interference of the reflected (diffracted) beam. Scan results are presented on a spectrum with axis of 2Θ, with peaks positioned according to Bragg's relation :

$$n\lambda = 2dsin\theta \tag{12}$$

where n is an integer. Although it is possible to use XRD peaks for quantitative compositional analysis, determination of lattice parameters and strain analysis, its purpose for this project was only to qualitatively determine the presence of mineral phases. It has been demonstrated that it is possible to ratio the peaks of the monoclinic, tetragonal and cubic forms of zirconia in order to establish relative proportions of these phases[95 96]. However, the outcomes of such exercises are often compromised by the transformation of surface tetragonal phases to monoclinic, during sample preparation, and the continuum between tetragonal and cubic lattice parameters in Mg-PSZ's, due to Mg^{2+} substitution distorting the lattice[5].

In this project, the presence / absence of monoclinic and tetragonal peaks and the relative peak ratios allow for a good qualitative indication of the degree to which martensitic transformation has affected a cycled bulk sample.

3.2.6. Raman confocal microscopy

Confocal microscopy utilises a double pinhole system so that only light reflected or transmitted from the specific area of interest in a test sample reaches the eyepiece / camera. Scattered light from the wider sample is filtered out, as are image components that are out of focus. Because the area of interest is spatially limited, mapping scans are required for large sample areas[97]. Linked to Raman spectroscopy, this technique involves the generation of a unique spectrum for each mapping point, creating what is known as a data cube and requiring advanced software for data integration across the sample.

Raman spectra are generated from the modification of incident photons from a monochromatic light source (such as a laser): molecular vibrations within a test material absorb energy from the incident light, releasing photons with shifted frequency as result. A Raman spectrum therefore comprises peaks representing frequency shifts that are characteristic of molecular compounds.

Raman mapping was undertaken on the same epoxy mounts used for SEM work and additional mineral references from the Natural History Museum, utilising a WITec Alpha 300R system, with 50x microscope objective, 532 nm laser source and a spectrometer with 1800 lines/mm grating. Spectra were acquired with a spacing of 1-2 μm to create maps and average spectra calculated by the WITec software for selected regions within these maps. Background subtraction was completed in Origin 9.1 (OriginLab, Corporation, Northampton, USA), using a spline and snap-to-spectrum method based on user-selected anchor points. For small areas of averaging and 'noisier' spectra, a 5 point adjacent-averaging technique was applied to smooth the curves.

Gazzoli et al.[98] have convincingly demonstrated that hybrid spectra for zirconia doped with 6.19 - 13.95 mol% Ca can be directly linked back to the spectra for pure tetragonal and cubic forms. If end-member spectra for pure phases can be acquired, solid-solutions should therefore be quantifiable. Also, a micro-Raman mapping study by Bowden et al.[99] showed promise at identifying phases within and around Mg-PSZ grain boundaries. However, recent Raman work on zirconia[100] has highlighted the fact that there is still significant ambiguity around peak assignments in the zirconia Raman spectrum, especially for the tetragonal form.

3.2.7. Optical microscopy / stereoscopy

The positive and negative features of fracture surfaces were examined using a Novex RZ-range optical stereomicroscope at 50x magnification with a cold light source in ring illumination form. Images were captured with a Motic 580 camera inserted into the beam path. and controlled by Motic Images Plus 2.0 software.

3.2.8. Thermodynamic modeling using composition data

To test the viability of liquid generation from sample aggregates heated to service temperatures, a thermodynamic calculation was carried out, using FactSage 6.2. The latter is an integrated database and software package utilising Gibbs free energy as the central mechanism for predicting thermodynamically equilibrated chemical assemblages[101]. Its "Equilib" module was used in this instance to predict final reaction products and their concentrations, after one heating cycle. Using the SEM-WDS data for as-fired aggregates that did not display microstructural modification at 1 micrometre resolution, an average composition for the LP and HP refractories' aggregates was calculated. This composition was reacted at 1700 °C, with the assumption that Mg solubility in zirconia is superceded by magnesium's preference for reaction with Al and Si (a valid stance; cf. Chapter 2.1.3) as the FactSage database used did not include facility for the Mg-Zr solubility curve. The composition of the calculated liquid was then normalised without ZrO_2 values (due to the low levels and solubility of zirconia in a MgO-Al_2O_3-SiO_2 glass). Similar exercises have been undertaken by other refractory investigators[102].

The FactSage database utilised was "FToxid" which contains stoichiometric compounds (and their complementary solution data[103]) for twenty common elements. Specifically, within this database, the FToxid_SLAG A component, which includes CaO, SiO_2 and Al_2O_3, is described as having been thermodynamically optimised for all composition ranges in this ternary subsystem. The FToxid_SLAG A component was stipulated as one of the key 'ingredients' from which products of the simulated equilibration run should be derived.

3.3. Characterisation methods for thermomechanical properties

Thermomechanical properties were investigated at bulk material level using temperature ranges analogous to service conditions. Linear thermal expansion was monitored using dilatometry. Stiffness was measured by impulse excitation and the capture of resonance

frequencies. Three point bend tests were used to determine strength and fracture toughness. A double cantilever rig microtest rig was operated under SEM conditions to record R-curve behaviour.

3.3.1. Dilatometry

Sample bars (25 x 5 x 5mm) were placed in the graphite sample chamber of a Netzsch DIL402E (Figs. 14 and 15), and nested on two graphite buffer rings. A graphite push rod was placed up against the sample and the temperature increased systematically from ambient to 1950°C at a rate of 10°C/minute under helium atmosphere (flow rate of 250 ml/min), used because of its high thermal conductivity. After a 10 minute dwell time at the maximum temperature, the furnace was cooled at 10°C/minute and the samples were therefore cool before removal. A graphite blank (25mm length) was run before the samples, using identical run conditions, and used to auto-correct for pushrod behaviour during data acquisition (at 40 points / minute).

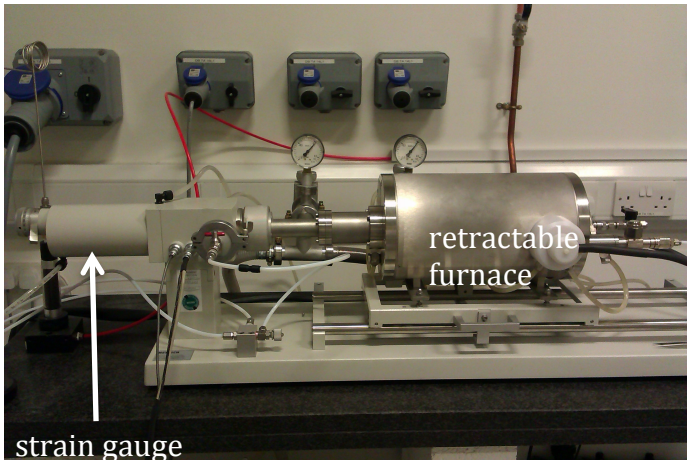

Figure 14 : Netzsch DIL402E bench top dilatometer.

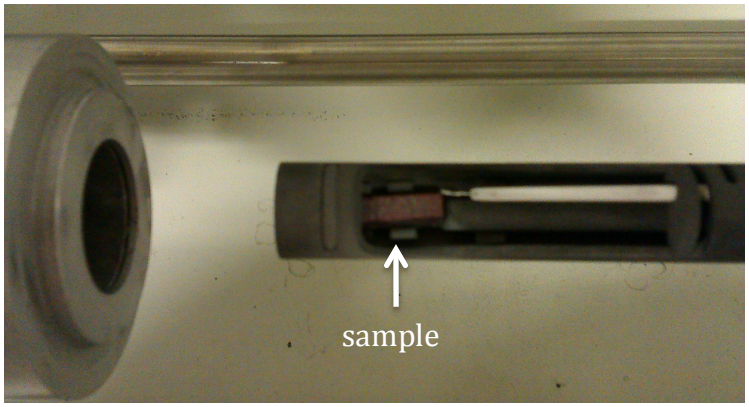

Figure 15: Sample chamber with W-Re thermocouple on right (white tube) and discoloured sample, after heating, in centre. Graphite chamber inserts into strain gauge unit on the left.

Dilatometry curves were analysed in a variety of ways to obtain m-t and t-m onset and end temperatures :

1. Tangents were hand drawn against the traces where marked slope change was observed. The intersection of these tangents was used to obtain a single onset/end temperature. (This approach is well established but is somewhat subjective.)
2. A differential of each trace was plotted in order to obtain the peaks/troughs indicating maximum rate of slope change (Fig. 16 is an example). These were used to identify a single inflection temperature, characteristic of the m-t or t-m transformation.
3. Using change in sample length (dL) over original length (L_o), a maximum dL/L_o value was identified on the expansion trace (and a minimum dL/L_o value on the contraction trace) and the corresponding temperature recorded as another way to obtain an objective characteristic value for m-t or t-m onset or end.

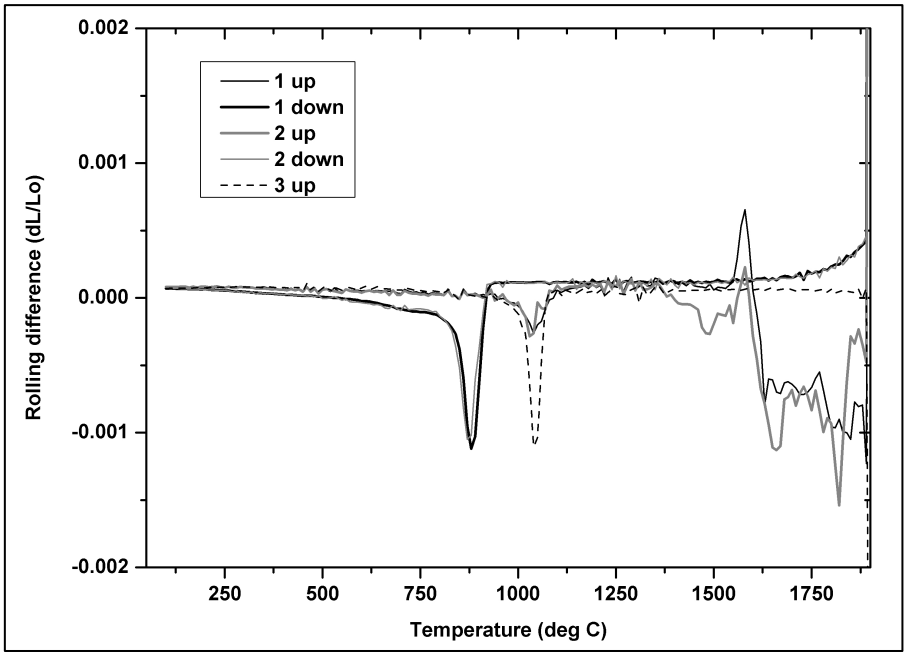

Figure 16 : A differential (rolling difference between two successive data points) was calculated for each dilatometer curve. The peaks and troughs highlight the points where slope change/ inversion is fastest. Data are for Sample LP.

The ratio dL/L_o was also plotted against temperature (T) so that the slope of each graph provided the mean coefficient of linear thermal expansion (CTE or alpha, α), as follows:

$$\alpha = \frac{dL}{L_0}\ x\ \frac{1}{dT} \tag{13}$$

The CTE can be obtained from a median point on the slope or a selected interval of the slope. Using the latter approach, CTE's were determined for all of the samples. Two CTE's were obtained per slope, whenever a polymorphic transformation was recorded: pre-transformation and post-transformation.

3.3.2. Impulse excitation and resonance frequency and damping analysis (RFDA)

Young modulus values were calculated, using the ASTM method for impulse excitation of vibration[104], from frequency values obtained on rectangular bars (±10 x 20 x 60mm) subjected to impulse excitation. Bars mounted on alumina struts inside a RFDA 1650 (IMCE, Diepenbeeck, Belgium) furnace were struck every 60 seconds over a thermal cycle of 10 hours, with a ceramic striker (Fig. 17). The resulting resonant vibration was captured as a sound wave by a microphone mounted inside the furnace roof. Heating and cooling rates were 7 °C /min and each thermal cycle comprised heating to 1750 °C and cooling back to room temperature. Modification of the Young modulus data to take account of thermal expansion produced average differences of 0.03 GPa and this aspect of data processing was therefore discarded. Damping peaks were used as supporting evidence for features evaluated in the stiffness curves.

Figure 17 : A - Sample bar mounted on alumina hearth furniture at node points to ensure minimum damping of resonance. Ceramic striker tube centrally oriented beneath. B - Sample mount illustrated in A sits on elevator hearth which is raised into the furnace. Argon gas cylinder in background, used for inert gas atmosphere inside furnace.

The vibration measured in the samples is a transient and natural vibration, meaning that it acts as a restoration of equilibrium in what is assumed here to be an elastic system. Among the various modes (shapes) of vibration, a principal mode exists, in which all parts of the test

specimen move through maximum and minimum velocities simultaneously. By equating the maximum kinetic and potential energies for this mode, it is possible to determine the natural frequency of the material[105].

Through iteration, the RFDA software obtains a best fit to the actual signal obtained, to isolate the fundamental resonance frequency[106]. From this frequency (f_r), the elastic modulus can be calculated from sample mass (m), length (L), breadth (b), thickness (t) and Poisson ratio (μ):

$$\mathrm{E} = 0.9465 \left(\frac{m(f_r)^2}{b}\right)\left(\frac{L^3}{t^3}\right)T \tag{14}$$

once a constant (T) has been determined as follows:

$$T = 1 + 6.585(1 + 0.0752\mu + 0.8109\mu^2)\left(\frac{t}{L}\right)^2 - 0.868\left(\frac{t}{L}\right)^4 - \left[\frac{8.340(1+0.2023\mu+2.173\mu^2)\left(\frac{t}{L}\right)^4}{1.000+6.338(1+0.1408\mu+1.536\mu^2)\left(\frac{t}{L}\right)^2}\right] \tag{15}$$

The ASTM method[104] has been shown to yield a coefficient of variation of 0.3% for the mean flexural frequency of a standard alumina bar across ten tests.

In addition to resonance, the impulse excitation method can be used to determine internal friction or damping, arising from dissipation of the mechanical energy introduced. Vibration damping is calculated from the energy dissipated in one stress (loading) cycle relative to the maximum stored elastic energy in that cycle[107]. For viscoelastic materials, the time delay between stress and arising strain (mechanical loss angle) can also be attributed to damping[108] [109]. Damping data give useful information on bulk microstructure and phase transformation as increases in crystallinity or decreases in glassy phase viscosity immediately reduce the amount of energy absorbed by a test sample. Damping peaks have been shown to widen at high temperature[110] and to decrease in amplitude with repeated thermal cycling of samples[107] [111]. The relationship between stiffness and damping also yields useful microstructural evolution analysis for ceramics. Importantly, when aliovalent dopant ions are added to ceramic lattices (e.g. Mg^{2+} in zirconia), causing charge compensating oxygen vacancies, the elastic dipoles that arise re-orientate, on sample heating, in order to reduce lattice strain. Such relaxation events

absorb energy and yield distinct drops in stiffness and peaks in the damping data[108 111 109]. Calculations of Young modulus (E) from the resonance frequency can be modified to take into account thermal expansion during high temperature testing or the presence of high levels of porosity in test samples. For porous samples, E in impulse excitation work has been modified to: $E = E_o^{-bP}$, where E_o is the zero-porosity modulus, P the porosity and b a material constant[112].

3.3.3. Three point bend testing

Bars were cut from vertical sections of the three commercial crucibles for three point bend testing on a Zwick-Roell universal testing machine (Fig. 18A). In keeping with industry quality control practice, these bars were used in their curved form (Fig. 18B) with original inner and outer surfaces intact and bar thicknesses in the range 11.7 - 13.7 mm (as opposed to the Standard requirement of 25mm[113]). In all other respects however, the standard method for modulus of rupture (MOR) testing of refractories was followed: Bars conformed to the 25mm width and 152mm length stipulations and were placed across the regulation 127mm span. As recommended, crosshead approach was regulated to ensure a constant stress of 0.15 MPa/s (9MPa/min), as opposed to constant speed. To accommodate bar curvature, 5 test specimens were mounted convex side up and 5 specimens concave side up, for a total of 10 tests per sample. Standard deviation was calculated for the 10 specimens using the square root of the variance, with the latter calculated as the average [using n-1=9] of squared differences from the mean.

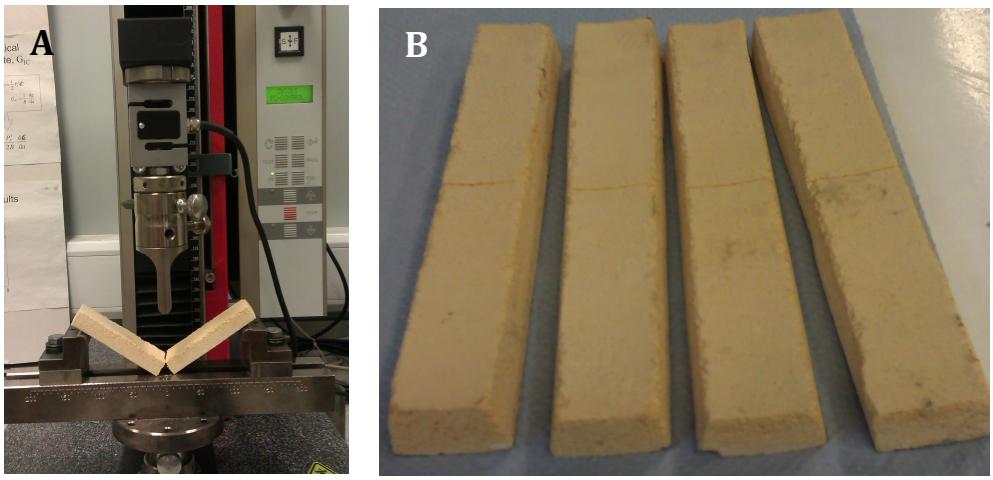

Figure 18 : A - Zwick-Roell universal testing machine. Test bar here was broken across a 127mm span with crosshead approach regulated to ensure constant stress. B - Typical test bars used for the three point bend tests. Slight curvature is evident in the cross-section. Bars are 152 x 25 x 12.5 mm.

This practice was repeated for single-edge notch bend (SENB) fracture toughness testing, in which bars were notched using a diamond wheel of 0.5mm thickness. Because of expected R-curve behaviour, single value fracture toughness measurements are not considered a fully quantitative result for a refractory sample[64], but the intention in this test was to compare pre- and post-thermal cycling results and therefore a relative response was the aim.

Due to bar curvature, notch depths were not constant across bar widths. Notch extent was measured in the breakage surface after testing, and ranged from 10-40% of sample depth. The average notch depth was used for K_{IC} calculations, according to the equation:

$$K_{IC} = \sigma\sqrt{\pi a}\,.\left[1.12 - 0.23\left(\frac{a}{b}\right) + 10.6\left(\frac{a}{b}\right)^2 - 21.7\left(\frac{a}{b}\right)^3 + 30.4\left(\frac{a}{b}\right)^4\right] \quad (16)$$

where a is the notch depth, b the total bar depth and σ the failure stress. For this equation to hold, $a/b < 0.6$ must be satisfied[114].

Because of the relatively stable nature of the SENB fractures, the area under the force-displacement curves - obtained by 'mathematical area' integration in Origin 9.1 (OriginLab Corporation, Northampton, USA) - can be used as a measure of the fracture energy. Work-of-fracture (WOF) values were calculated by dividing this fracture energy by the rectangular area assumed for each bar's fracture surface (the box in Fig. 19, with the loss of the 'y' regions being compensated for by the material in the 'x' regions).

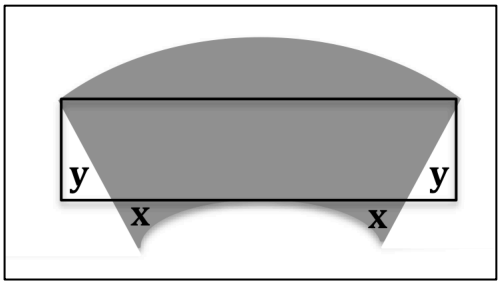

Figure 19 : Schematic cross-section of a SENB specimen (curved, grey bar). The fracture surface used in WOF calculations is represented by the black rectangle - a simplification achieved by assuming 'x' compensates for the loss of 'y'. The bar area above the box is the notch region.

3.3.4. Double cantilever fracture testing

Small bar samples were notched to a double cantilever geometry and loaded into a micromechanical rig as described by Sorensen et al.[115] The rig enables application of pure bending moments to the sample via a metal ribbon running through symmetrical grips applying tension (Fig. 20). The rig is mounted on a SEM stage so that crack propagation can be monitored and imaged *in situ*, under secondary electron imaging mode. Loading was recorded using a 300N load cell. With each cantilever beam defined by thickness (H) and width (B), and Young modulus (E) and Poisson ratio (ν) known, the plane strain energy release rate, G, can be determined from the moment (M), as follows :

$$G = 12(1-\nu^2)\frac{M^2}{EB^2H^3} \tag{17}$$

and the moment is calculated from the tensile force (P), radius of the rig rollers (R) and the distance between the centre of these rollers (d):

$$M = P(2R+d) \tag{18}$$

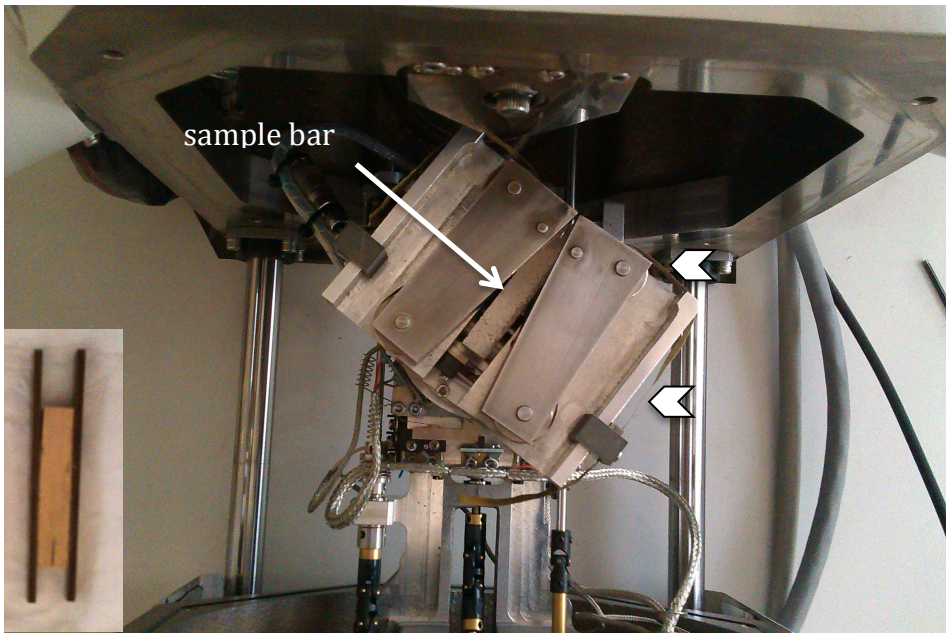

Figure 20 : Micromechanical rig mounted on SEM stage. View from above. Arrows indicate metal ribbon producing equal moment. Inset : example of cantilever bar with steel buttressing.

Heuer et al.[116] found that placement of a central groove down double cantilever test bars - initially suggested in order to prevent cracks veering off to the side of specimens - did not give rise to full through-thickness cracks, perpendicular to the polished surface being monitored. They overcame this problem by using shorter bars, ungrooved, with longer starting notches, to create "compact tension" specimens.

A similar approach was taken for this project's samples, with bars of 10 x 5 x 45 mm used. Because of low strength, test bars repeatedly failed at the base of the cantilevers and a modification was made such that low-width sample bars (5 mm instead of 10mm) were buttressed either side with steel plates (each 2.5 mm wide) of similar thickness (5mm) to the test bar.

4. MICROSTRUCTURAL EVOLUTION

The three commercial refractories were first characterised in terms of as-fired microstructure and aggregate grain size distribution, using SEM imaging. Microstructural evolution in aggregates was then evaluated in terms of morphology changes down to ±1 micrometre resolution (again using SEM imaging) after two, four, six and eight thermal cycles. A natural continuum of features was observed to exist in the aggregates, but distribution of these features did not necessarily evolve in a systematic way and some were already evident on as-fired aggregates. Thus, instead of presenting the results in a chronological sequence, *modes* of modification are discussed. Compositional triggers for the microstructural changes were evaluated through analysis of stabiliser and impurity element trends.

In this chapter, first level interpretation of results (e.g. comparison between observed phenomena; links between results and known manufacturing information) is included with the presentation of the data so that, in the discussion section which follows, emphasis is placed on the broader narrative of aggregate evolution and the development of a model for those mechanisms leading to the most radical alteration of overall refractory microstructure.

4.1. Results

4.1.1. The as-fired microstructure

Representative microstructures are presented for the refractories in Fig. 21. The LP microstructure, manufactured at standard pressures with additional MgO fines in the matrix, is characterised by a strong interface between aggregate and matrix (centre region of Fig. 21A) with large pores mainly concentrated in the matrix phase. The HP microstructure, manufactured at high pressure with no additional stabiliser in the fines, displays a denser matrix than that of LP, with large pores mainly concentrated at the interface between aggregate and matrix where debonding has occurred during firing (Fig. 21B). The SA refractory, comprising monoclinic zirconia aggregates with stabilised fines, and whose manufacturing details are unknown, yields a more homogeneous microstructure, relative to LP

and HP. Its pores are smaller and do not preferentially align with either aggregate or matrix phase (Fig. 21C and D).

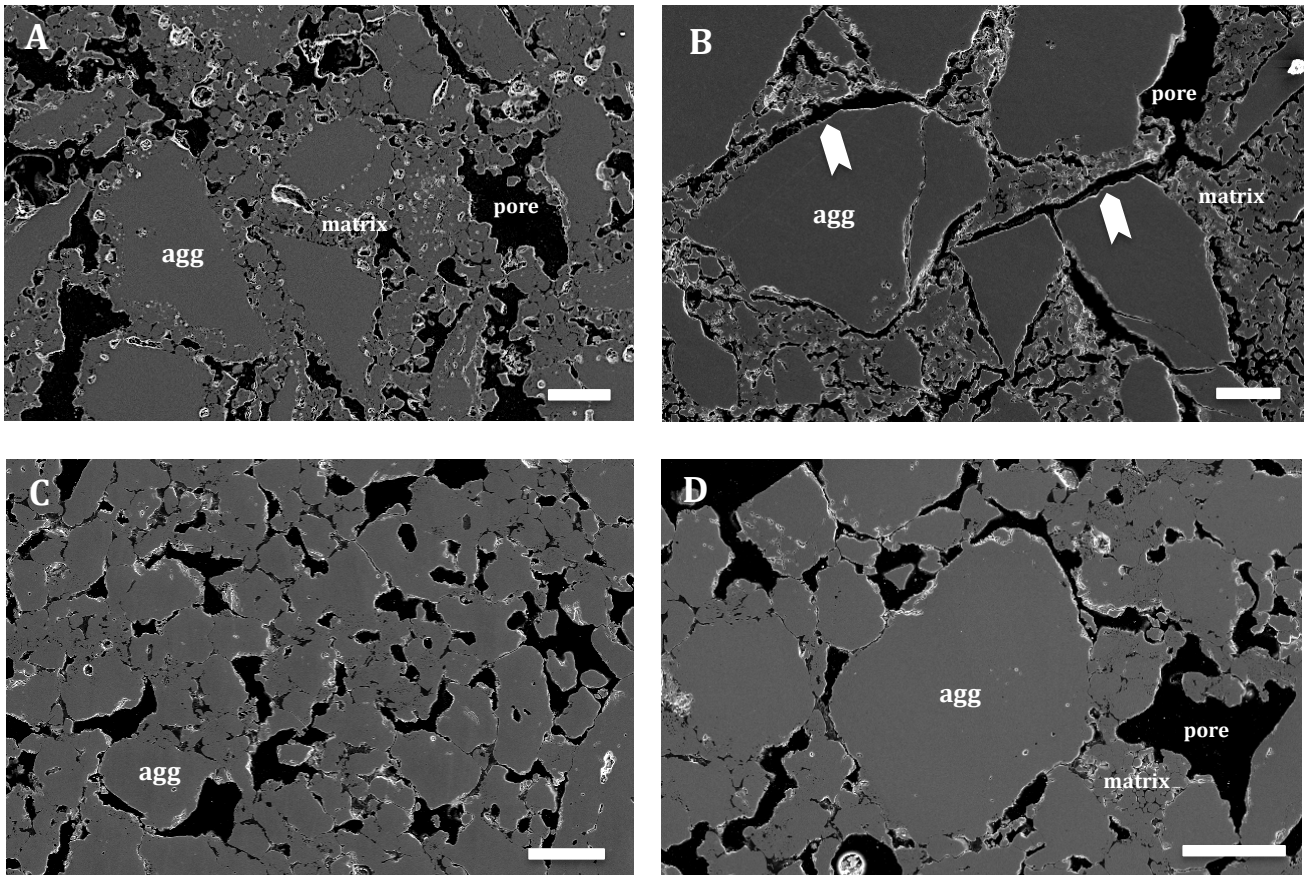

Figure 21 : Representative fields of view (Secondary electrons) of the LP sample (A), HP sample (B) and SA sample (low magnification in C and higher magnification in D). 'agg' = aggregate. Aggregate-matrix debonding in HP indicated by white arrows. Scalebars are 100 µm.

LP and HP have similar grain size profiles for their aggregate populations (Fig. 22) with LP containing a slightly higher proportion (53%) of larger aggregates (≥0.02 mm^2) than HP (43%). The aggregates of SA are significantly smaller: 96% are ≤0.02 mm^2. Grain sizes are presented as two-dimensional (cross-sectional) areas in Table 2 with diameter equivalents calculated by assuming the aggregates to be spheres.

Table 2: Grain size characteristics for the refractories, determined by image analysis of SEM backscattered electron images at 50x magnification. 'n' indicates number of aggregates analysed per sample.

Sample	A_{50} (mm^2)	d_{50} (mm)	A_{90} (mm^2)	d_{90} (mm)	A_{10} (mm^2)	n=
LP	0.0209	0.163	0.0763	0.312	0.0078	311
HP	0.0166	0.145	0.0695	0.298	0.0065	287
SA	0.0040	0.071	0.0124	0.126	0.0019	328

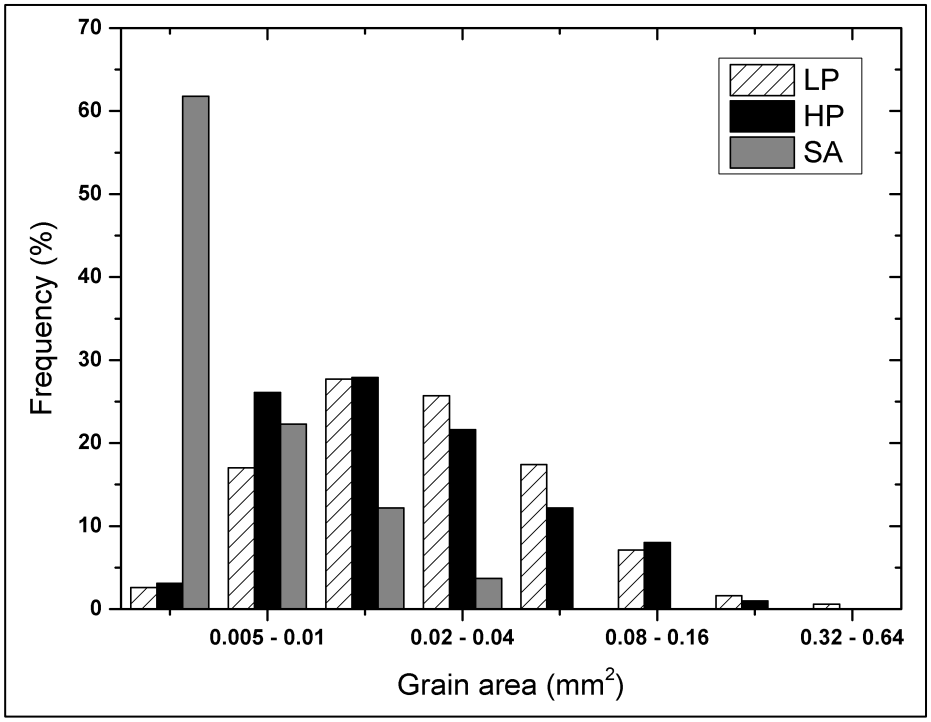

Figure 22 : Grain size profiles for the aggregate populations in samples LP, HP and SA, based on image analysis of ±300 aggregates per sample at 50x magnification.

4.1.2. Observed microstructural changes

In all three as-fired refractories, many aggregates appear 'intact' at micrometre scale i.e. they display no cracks, pores or precipitates within their boundaries when viewed in secondary, or backscattered, electron images. Relative to this 'baseline', similar microstructural modifications are observed for other aggregates in the fired and cycled LP and HP refractories. Microstructural modifications include, but are not limited to, stippled cross-sections reminiscent of subeutectoid decomposition[41], linear fractures, large internal pores, areas covered in micropores, microcracks and the breakdown of aggregates into subparticles (termed 'subgrains' for the remainder of this document).

Micropores are observed throughout some aggregates (Figs. 23A and B) and are partially present across others (Figs. 23C and D). They are also observed in the SA refractory aggregates (Fig. 23E) which do not contain MgO stabiliser and a direct link to volatilisation of the stabiliser is therefore not obvious. In many instances, these fine pores occur as linear features (Fig. 23F).

Microcracking is often associated with microporosity (Figs. 24A and B). Microcracks are evident in both the LP and HP aggregates and range from small (±20 μm) fissures (highlighted

in Fig. 24C) to parallel cracks extending almost entirely across individual aggregates (>50 μm; highlighted in Fig. 24E). In some instances, a crystallographic control is evident with fissures oriented ±109° to each other (highlighted in Figs. 24D and F).

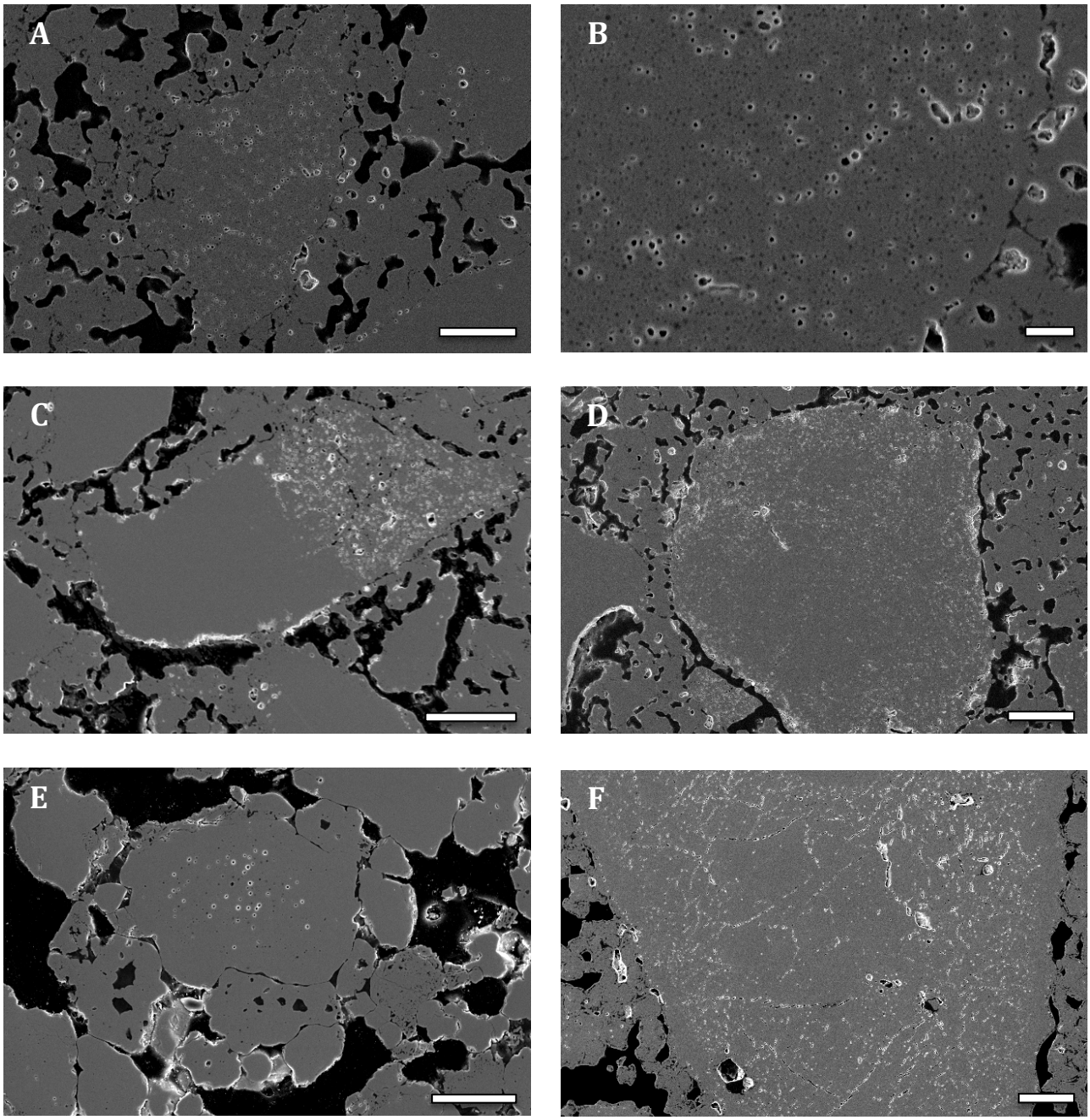

Figure 23 : A - HP aggregate after 4 cycles; B - same aggregate as A at higher magnification; C - HP aggregate after 8 cycles; D - HP aggregate after 8 cycles; E - SA aggregate as-fired; F - LP aggregate after 6 cycles. Scalebars - 50, 10, 100, 100, 50 and 100 μm respectively.

The microcracking is attributed to volumetric strains arising from monoclinic-tetragonal-monoclinic transformations during heating and cooling. Evidence for these strains was

obtained in dilatometry studies (cf. Section 5.1.1.) in which both LP and HP samples display a clear linear expansion of ±0.3% during cooling between 850 °C and 1000 °C, following a corresponding contraction (±0.5%) on heating over the range 960-1100 °C for their first service cycles. The linear extent of these parallel features (±10-100's μm) correlates with those of the linear transformation bands that Marshall and Swain[117] have documented in Mg-PSZ samples subjected to indentation tests.

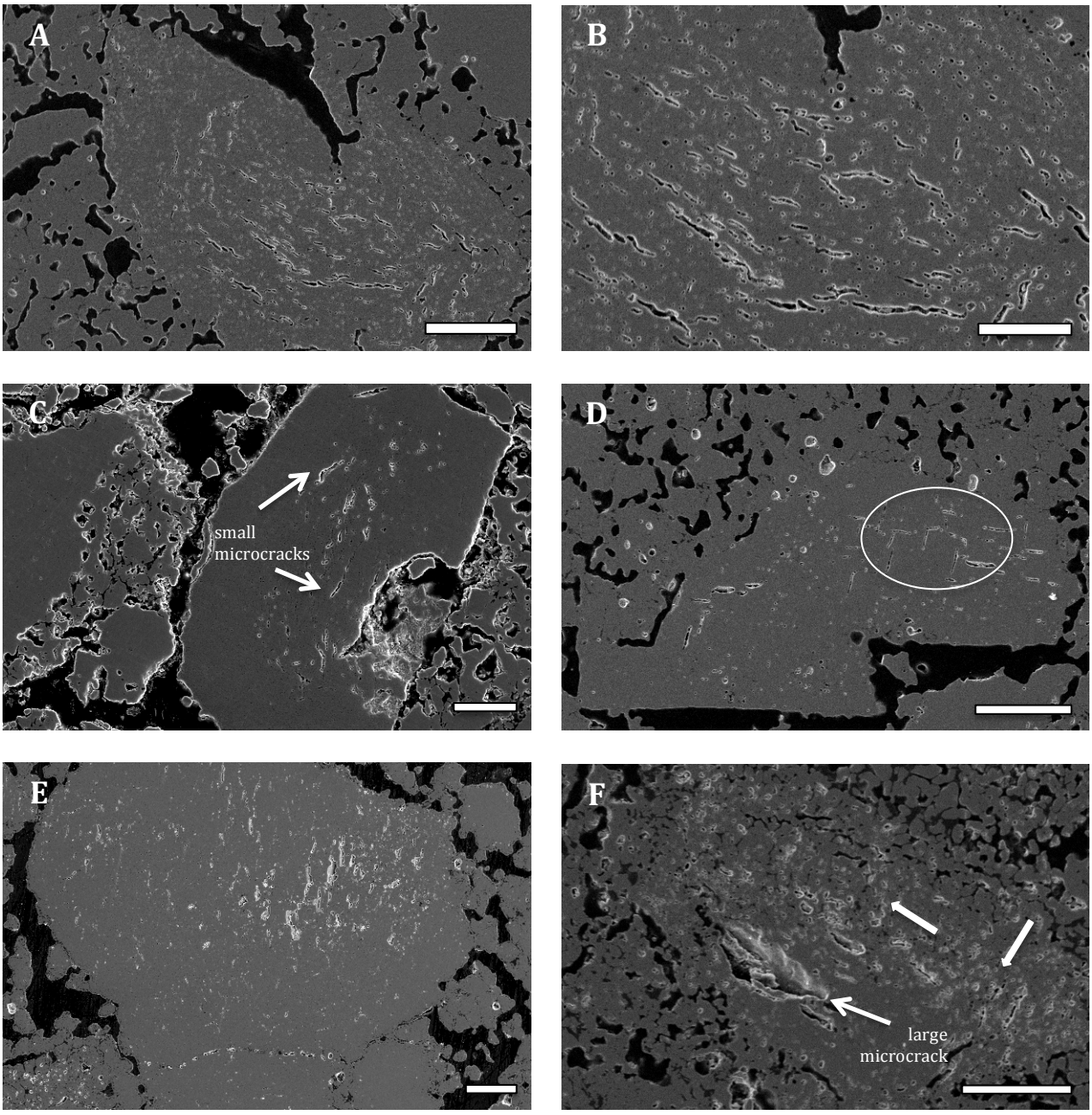

Figure 24 : Secondary electron images; A - HP aggregate after 4 cycles; B - same aggregate as A at higher magnification; C - HP aggregate as-fired; D - HP aggregate after 8 cycles, with crystallographic control evident (circled features); E - LP aggregate after 8 cycles; F - HP aggregate after 6 cycles with two prominent orientations as indicated by arrows. Scalebars - 100, 50, 50, 100, 100 and 100 μm respectively.

The third dominant form of aggregate modification, **subgraining**, occurs extensively within the LP refractory and less frequently in the HP refractory (Table 3). A spectrum of features is observed: some aggregates are just starting to show break-up by virtue of curvilinear traces of pores (highlighted in Fig. 25A); some display clearly identifiable subgrains (Figs. 25B-D) bounded by secondary phases, fractures or triple junctions and others are completely transformed to a cluster of subparticles. In some fields of view, subgraining was observed at aggregate edges only.

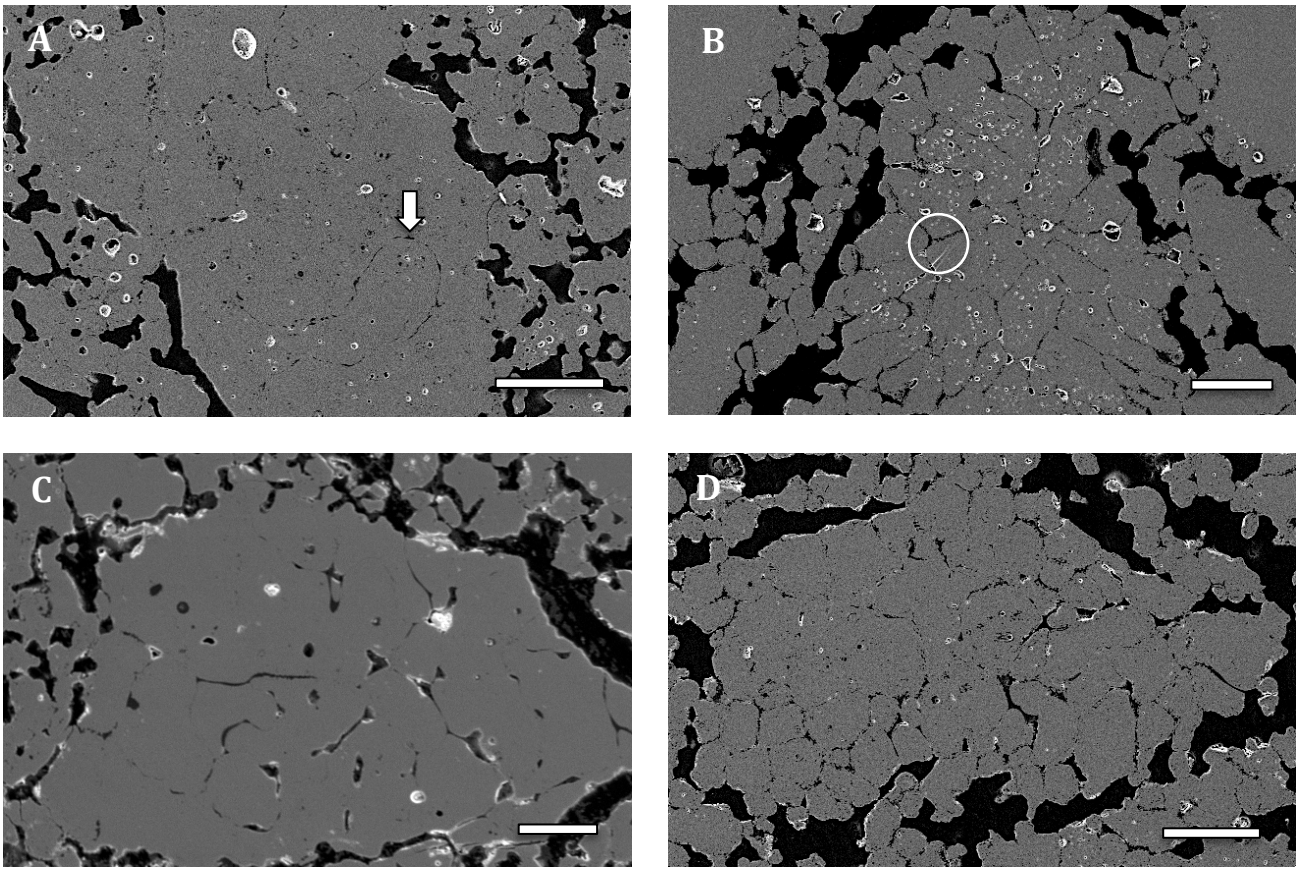

Figure 25 : Secondary electron images; A - HP aggregate after 8 cycles (arrow shows curvilinear pore trace); B - LP aggregate after 8 cycles (triple junction circled); C - HP aggregate after 2 cycles; D - LP aggregate after 2 cycles. Scalebars - all 100 µm except for C which is 50 µm.

Table 3 provides a semi-quantitative, comparative summary of the frequency of occurrence of the dominant forms of aggregate modification in the LP and HP refractories, based only on those fields of view acquired at 50x magnification. In the LP refractory, subgraining leads to extensive degradation of the microstructure as a whole (Fig. 26A) after just eight thermal

cycles. For the HP refractory, aggregate evolution is dominated by microcracking and microporosity (Fig. 26B) but the microstructure remains relatively intact after eight thermal cycles.

Table 3 : Semi-quantitative analysis of frequency of aggregate modification, using a broad classification of features derived from study of 329 fields of view.

	LP sample		HP sample	
	As-fired	**Cycled**	**As-fired**	**Cycled**
% frequency of aggregates displaying microstructure at 50x magnification	±10	±25-50	±2	±15
Microstructures listed in decreasing dominance	1) microcracks, often with associated microporosity 2) early subgraining	1) subgraining (ranging from semi-continuous traces of pores dividing aggregate interiors, to completely separated subunit clusters) 2) microporosity 3) through-cracks	1) microcracks, often with associated microporosity 2) early subgraining 3) through-cracks	1) microcracking - reaching the level of open fissures running parallel across aggregates 2) aggregate cross-sections covered in micropores 3) early subgraining

The aggregates of the SA refractory display occasional through-fractures and micropores but are otherwise undamaged at micrometre scale, with heat treatment during firing and early service cycling. The most noticeable microstructural change observed is that of the relationship between aggregate and matrix. Distinct boundaries at aggregate-aggregate, aggregate-matrix and matrix-matrix interfaces are evident in the as-fired refractory (examples are arrowed in Fig. 27A). After thermal cycling, aggregate and matrix particle boundaries become less distinct. A more bonded microstructure is evident, with inclusion of what is interpreted to have been a liquid phase at high temperatures (Fig. 27B).

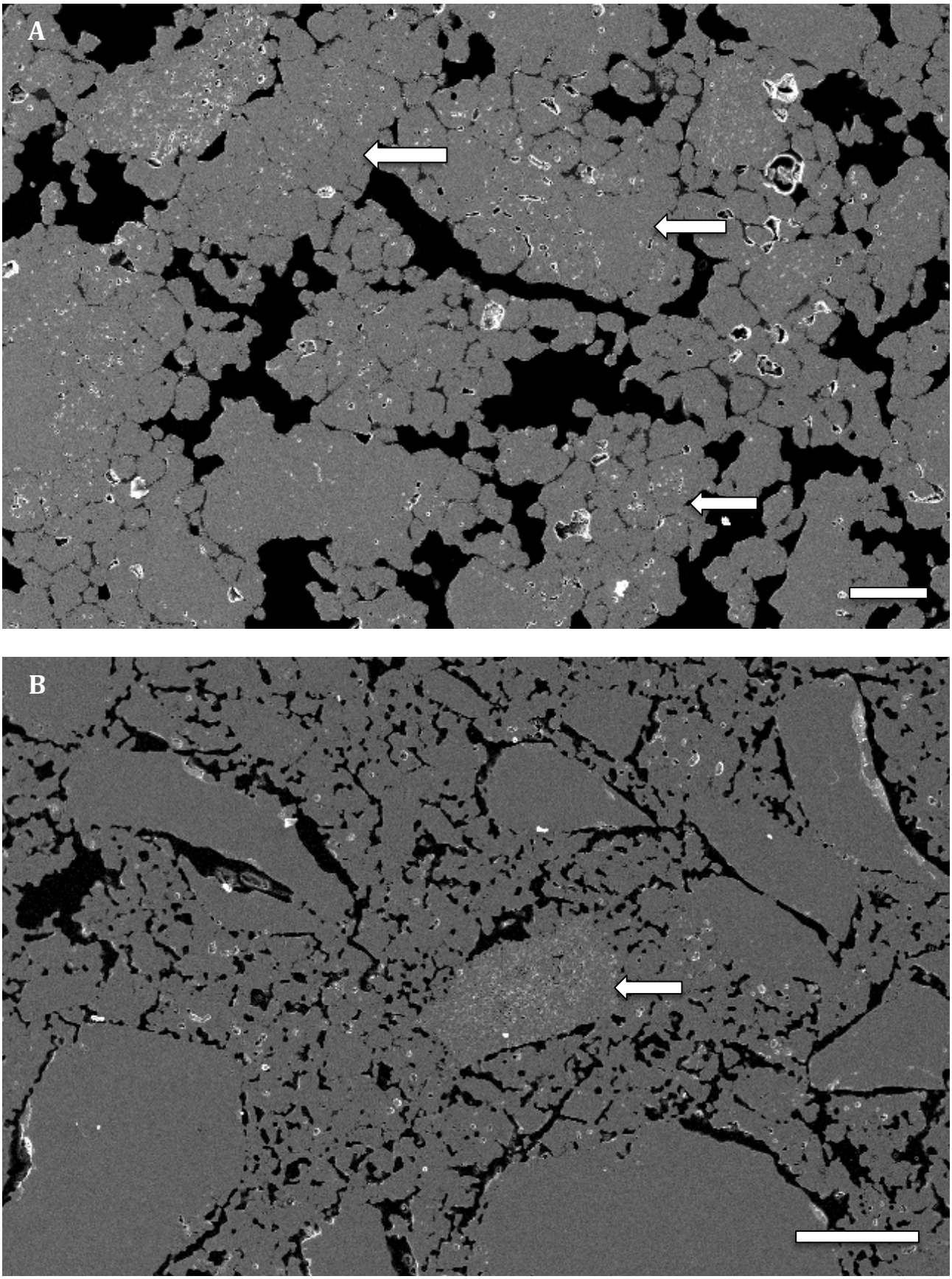

Figure 26 : Secondary electron images; A - LP refractory after 8 cycles (significant breakdown evident in arrowed aggregates); B - HP refractory after 8 cycles (micropore hazing on arrowed aggregate). Scalebars are 100 and 200 µm respectively.

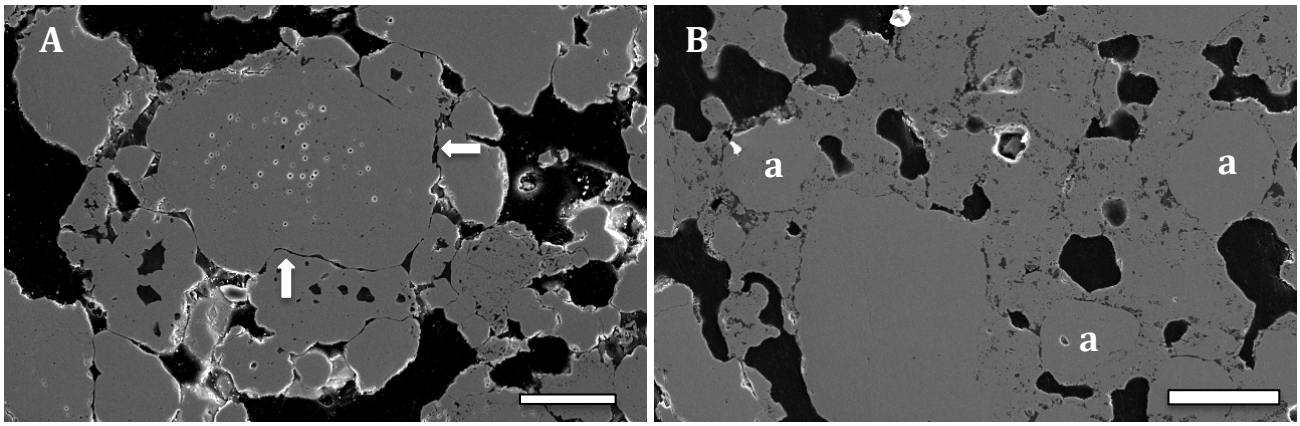

Figure 27 : Secondary electron images of the SA refractory microstructure before (A) and after (B) eight thermal cycles. 'a' denotes typical aggregates. Arrows in A show distinct interface boundaries which are missing in the microstructure of B.. Scalebars are 50 µm.

4.1.3. Compositional evolution : stabilizer

Four aspects of stabiliser distribution were evaluated :

i. differences between the refractories
ii. extent of inter-aggregate gradients within refractory
iii. extent of intra-aggregate gradients within refractory
iv. the link between stabiliser levels and aggregate microstructural modification

4.1.3.1. Differences in aggregate stabiliser distributions between the refractories

The range of MgO values reflected in the LP and HP as-fired and cycled aggregate populations is presented in Fig. 28 (determined by SEM-WDS). It is evident that MgO minimum concentrations are elevated in the LP refractory aggregates, relative to those in the HP refractory, by approximately 1 wt%, from the stage of refractory firing. This may be due to cation diffusion from MgO fines, present in the LP matrix and absent in the HP refractory. However, data acquired for a sample set of loose aggregates representing typical raw material inputs to the manufacture of Mg-PSZ crucibles, also have an elevated minimum MgO value and closely resemble the results for the LP aggregate population. This suggests that the difference between the stabiliser signatures for the LP and HP refractories might be attributable to stabiliser ranges in different batches or combinations of raw material inputs.

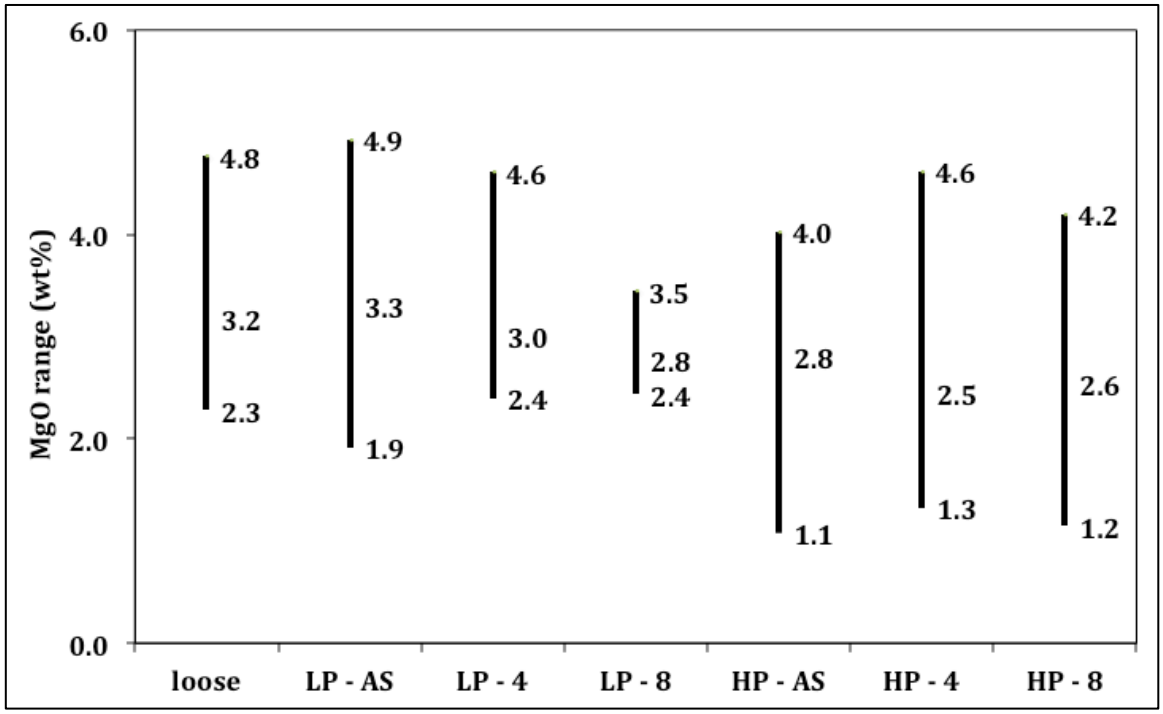

Figure 28 : Results for 468 SEM-WDS analyses on 75 aggregates. Samples are LP refractory in as-fired form (LP-AS), after 4 cycles (LP-4) and after 8 cycles (LP-8); HP refractory in as-fired form (HP-AS), after 4 cycles (HP-4) and after 8 cycles (HP-8); 'loose' represents data from typical Mg-PSZ raw material aggregates prior to incorporation in a refractory. Minimum, average and maximum range value cited for each population.

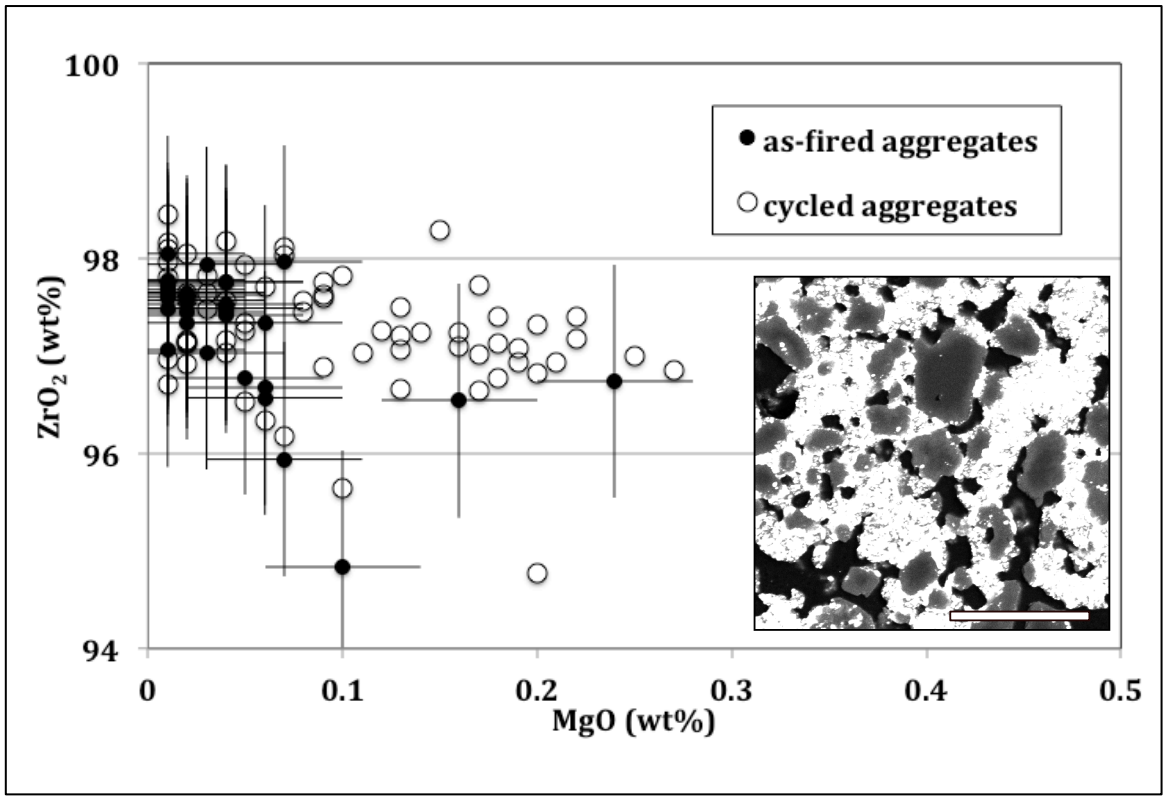

Figure 29 : SEM-WDS data for SA refractory aggregates. Error bars for the cycled aggregates have been removed for clarity but are of the same order of magnitude as those for the as-fired aggregates. Inset SEM-WDS MgO map shows rim zonation on the aggregates (dark particles) in surrounding matrix (white phase). Scale bar is 200 µm.

SEM-WDS results for aggregates in the as-fired and cycled samples of the SA refractory are presented in Fig. 29. Unstabilised monoclinic zirconia (baddeleyite) is used in the manufacture of this refractory and the MgO results for the as-fired sample reflect this fact, with the majority of analyses yielding a value within error of zero. However, over eight cycles, MgO diffusion from the Mg-PSZ matrix phase *into* the aggregate population leads to stabiliser values between 0.1 and 0.3 wt% in the latter. By enhancing the image contrast in the Fig. 29 inset, this diffusion gradient becomes apparent as rim zonation in the aggregates.

4.1.3.2. Extent of inter-aggregate gradients

MgO concentrations vary by up to 3 wt% within the as-fired aggregate populations of the LP and HP refractories and this mirrors the variability in stabilizer content in the raw supply (loose) aggregates (Fig. 28). Thermal cycling was expected to remove early MgO gradients between aggregates through diffusion processes. However, the reduced range of MgO concentrations for the LP aggregate population after eight cycles does not appear to reflect homogenisation, as the average and maximum MgO values both decrease. Rather, the data point to a loss of MgO from those regions of microstructure used in the SEM-WDS analyses, which were selected specifically to be clear of secondary phase or structure.

Gradients remain almost fixed between aggregates of the HP refractory. The higher matrix density of HP should facilitate solid state diffusion and it is assumed that the extensive debonding between HP aggregates and their surrounding matrix prevents Mg^{2+} ion movement out of the aggregates.

Several LP and HP aggregates (as-fired and cycles varieties) were analysed multiple times, at different locations. Fig. 30 contains the first ten analyses, for each of fourteen aggregates, taken from across the sample set. Even after eight thermal cycles, MgO variation between aggregates can remain significant (up to ±1.5 wt% for the cycled HP samples here) and in general, exceeds intra-aggregate variation (±0.5-1.5 wt%).

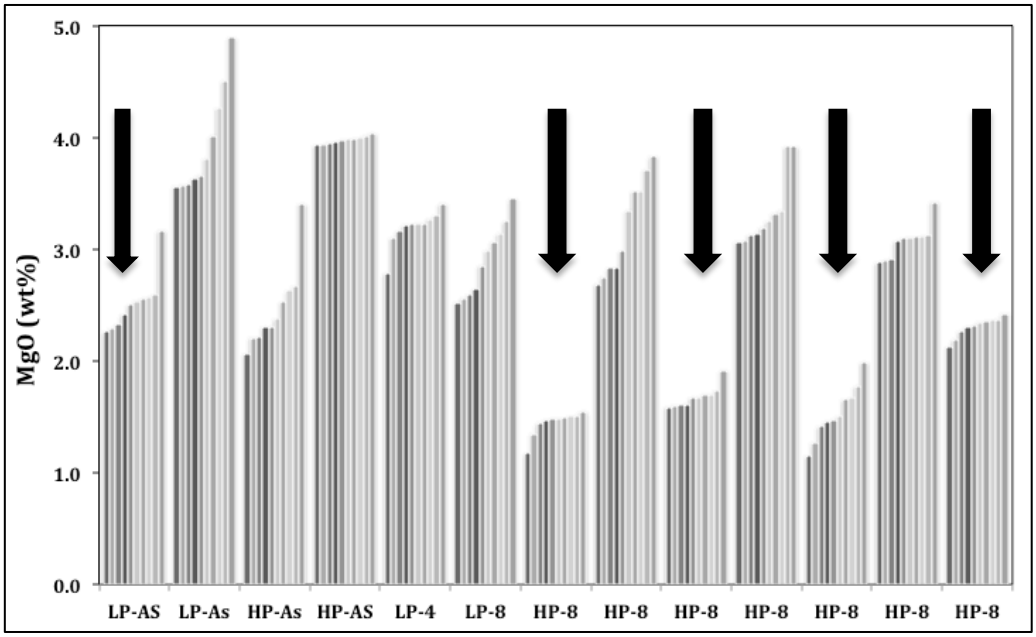

Figure 30 : A selection of data for those aggregates analysed multiple times at different locations by SEM-WDS. Samples are LP refractory in as-fired form (LP-AS), after 4 cycles (LP-4) and after 8 cycles (LP-8); HP refractory in as-fired form (HP-AS) and after 8 cycles (HP-8). Arrowed aggregates did not display visible microstructure at micrometre scale. Error bar for MgO concentrations on WDS is ±0.02 wt%.

Fig. 31 illustrates the microstructural scale at which inter-aggregate stabiliser contents may vary. Adjacent aggregates, spaced 200 micrometres apart in an as-fired HP sample, display MgO concentrations that differ by approximately 3 wt%. This observation strongly supports the conclusion that stabiliser gradients are due to variations in MgO in the aggregate material used to manufacture the refractories, rather than cation diffusion during firing.

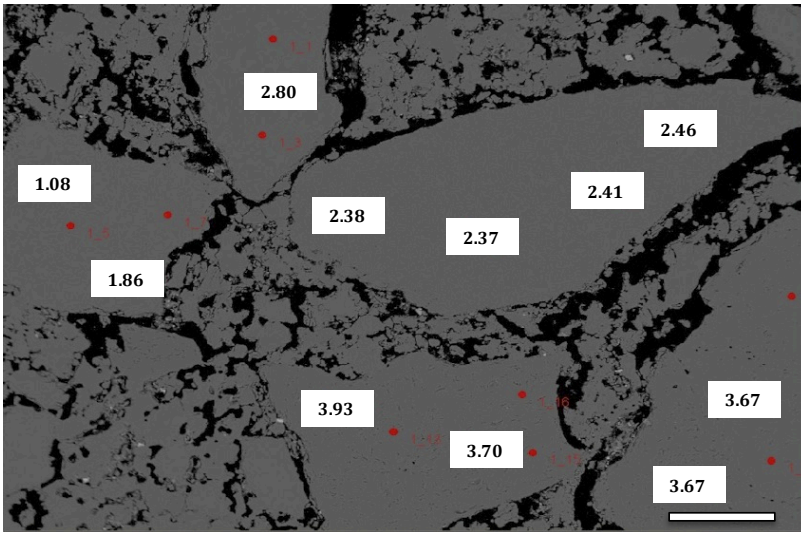

Figure 31 : Backscattered electron image of HP aggregates as-fired. Multiple SEM-WDS analyses were acquired (red spots), some of which are highlighted here with the MgO value located over the analysis point. MgO errors are ±0.02 wt%. Scalebar is 100µm.

4.1.3.3. Extent of intra-aggregate gradients

Two LP aggregates are shown in Fig. 32. Multiple SEM-WDS analyses were performed across their microstructures. In the as-fired aggregate (Fig. 32A), stabiliser concentrations vary from ±3.2 to 4.9 wt% - a difference of 1.7 wt%. After eight cycles, the aggregate in Fig. 32B still shows a gradient of ±1 wt% between constituent subgrains.

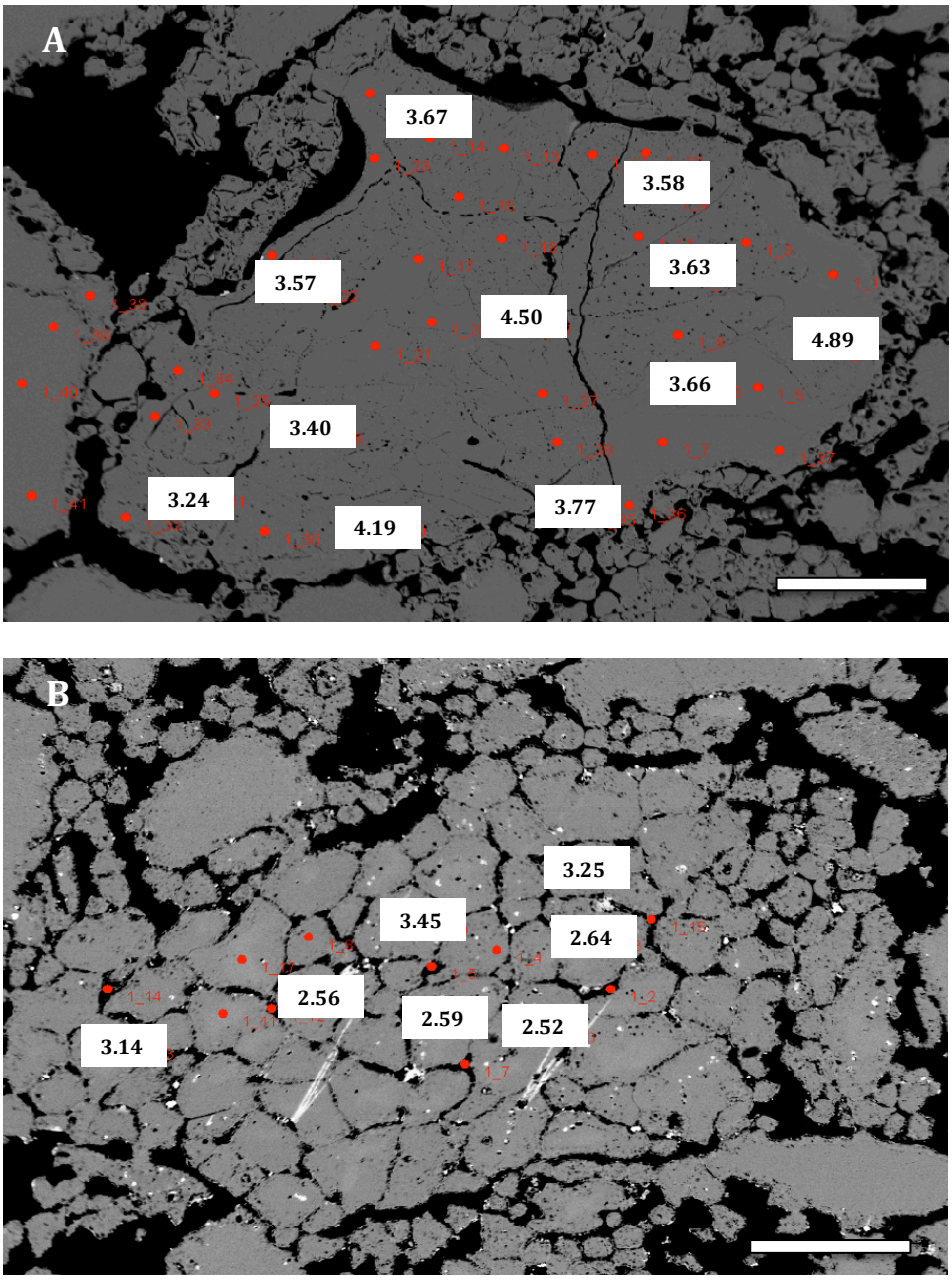

Figure 32 : Backscattered electron images of LP aggregates. A - As-fired aggregate; B - A different aggregate, after 8 cycles. Multiple SEM-WDS analyses were acquired (red spots), some of which are highlighted here with the MgO value located over the analysis point. MgO errors are ±0.02 wt%. Scalebars are 200 µm.

A typical field of view across a cycled HP microstructure is presented in Fig. 33, with MgO profiles determined through lines of point analyses using SEM-WDS.

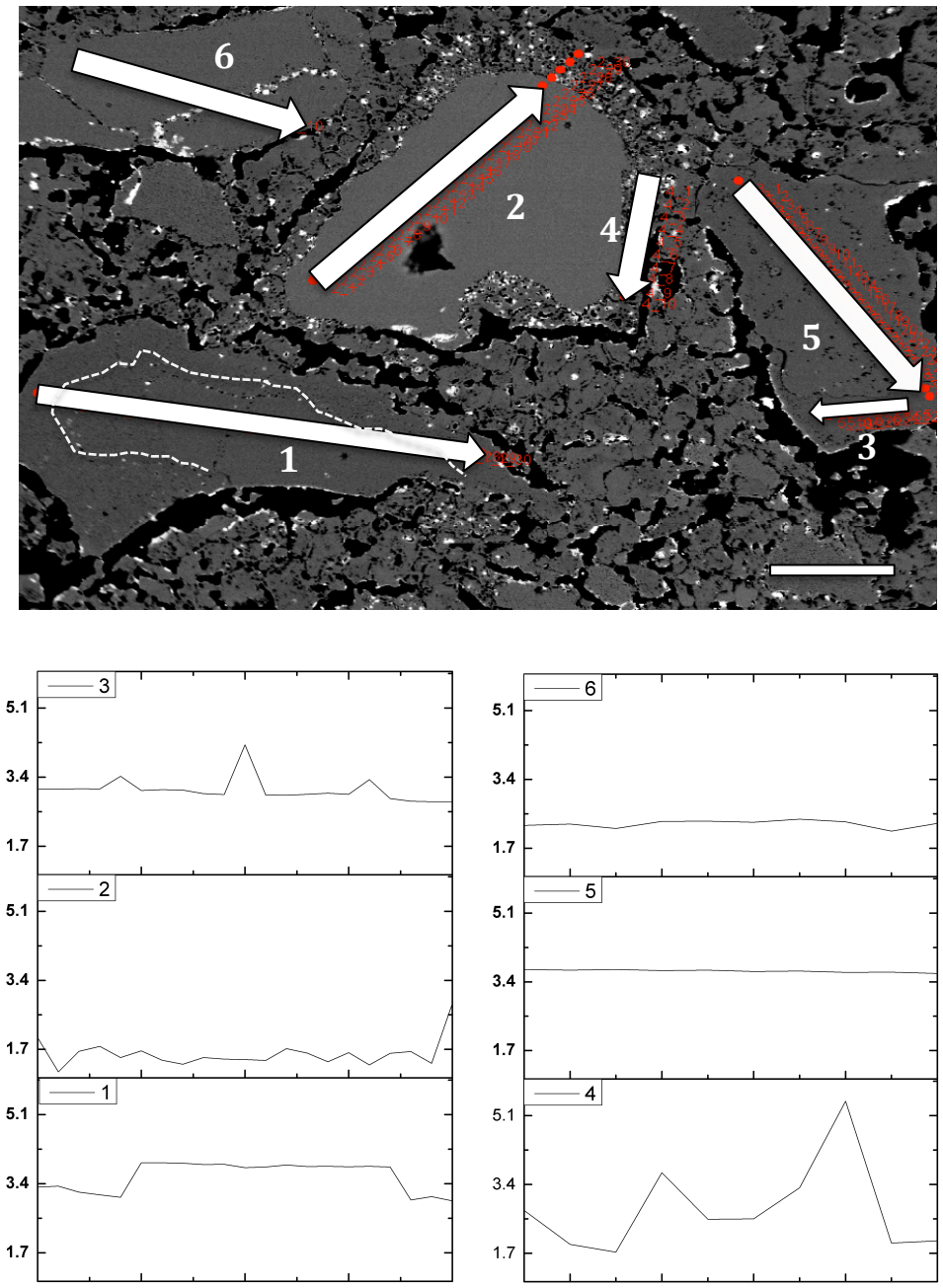

Figure 33 : Backscattered electron image of HP aggregates after 8 cycles. SEM-WDS analyses were acquired as linear arrays of 30 (graphs 1-3) or 10 (graphs 4-6) point analyses (red spots). Those portions of each array covered by white arrows in the micrograph are plotted below as MgO trends. X-axes from left to right correspond with arrow directions in micrograph. MgO errors are ±0.02 wt%. Scalebar is 200 µm.

Profiles 1 and 3 were acquired across aggregates displaying microstructural modification at micrometre scale. Profile 2 represents an unmodified aggregate at a similar scale of

observation with relatively constant stabiliser values. Profile 1 shows a drop in stabiliser at both edges of the aggregate, consistent with observed microstructural modification of the aggregate rim. Profile 3 shows intermittent elevations in MgO content, interpreted to be due to the presence of discrete Mg-rich phases.

It is known that subeutectoid decomposition and low temperature ageing processes during slow cooling give rise to Mg-rich discreet phases and remove Mg^{2+} from the zirconia lattice[41]. Homogenisation across an aggregate is then prevented by phase transformations. First, with conversion of the cubic host phase to tetragonal forms, there is decreased solubility of the stabiliser as the tetragonal lattice is less accommodating of the dopant ion. This process is reversible on reheating. However, as cooling continues, some of the tetragonal formed converts to monoclinic, with further expulsion of stabiliser, and this transformation is not fully reversible[118]. Thus thermal cycling is expected to lead to cumulative cation heterogeneity rather than homogeneity across aggregates.

4.1.3.4. The link between stabiliser levels and aggregate microstructural modification

In Fig. 33, profiles 2 and 6 were acquired across aggregates relatively free of microstructural modification at micrometre scale. These MgO gradients are flat and lie below 2 wt%. Profiles 3, 5 and 6, acquired over modified regions of the aggregates, reflect MgO concentrations around 3.4 wt%. Similarly, in Fig. 30, arrowed aggregates, representing unmodified microstructures, exhibit stabiliser values a full weight percent lower than those with morphology changes.

The link between microstructural evolution and elevated stabiliser levels is fairly consistent for all 75 aggregates in the dataset and two mechanisms may be invoked:

i) Those aggregates with MgO concentrations close to eutectoid values (>4 wt % or >12 mol%) are the first to decompose through subeutectoid reactions. Documented microstructures[41] for samples in advanced stages of subeutectoid decomposition are characterised by a stippled appearance, consistent with some of the degradation noted here (e.g., profile 3 aggregate in Fig. 33).

ii) Other processes (such as the formation of secondary phases) lead to a loss of stabiliser and produce associated microstructural changes. This aspect is pursued further, below.

4.1.4. Compositional evolution : impurity elements

SEM-EDS element maps (Figs. 34 and 35) and linescans (Figs. 35 and 36) across typical microstructural features in the as-fired sample aggregates of the LP and HP refractories reveal three repeatable element associations: Mg-Al, Mg-Al-Si and Mg-Si. In Figs. 34 and 35, elevated concentrations are revealed for Mg and Mg-Al, along subgrain boundaries.

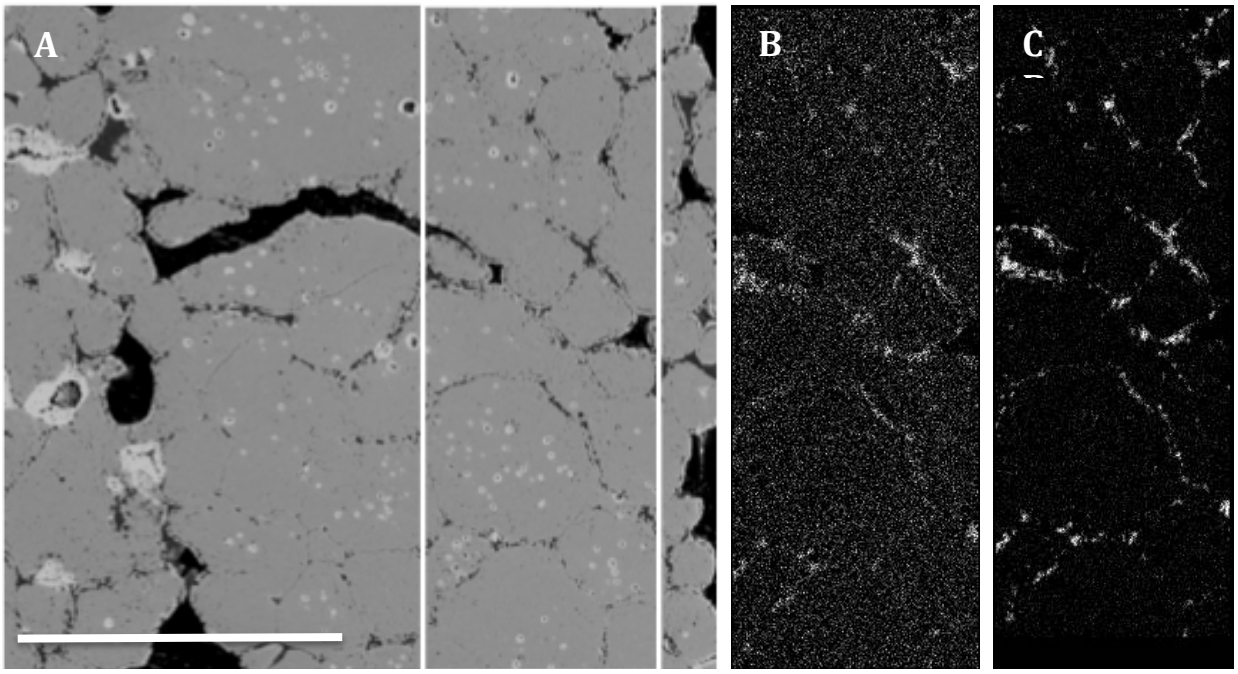

Figure 34 : Secondary electron image of an as-fired LP aggregate with subgraining. The corresponding SEM-EDS element maps for Al (B) and Mg (C) are presented. Scalebar 200 µm and scale maintained in element maps.

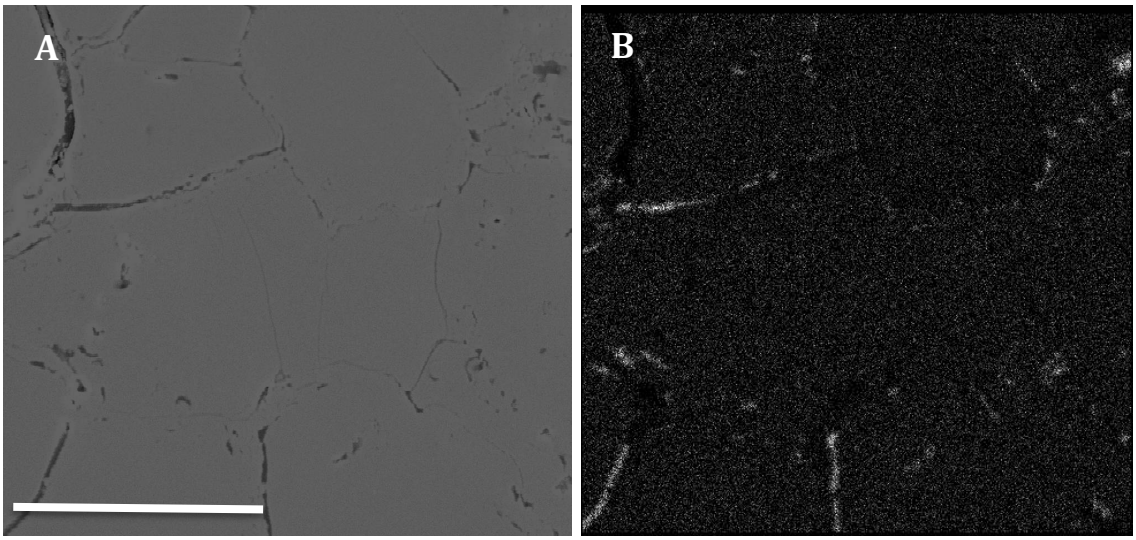

Figure 35 : Secondary electron image of an as-fired LP aggregate with break-down to subgrains (A). The corresponding SEM-EDS element map for Mg (B) is shown at the same scale. Scalebar 200 µm.

In Fig. 36, the association of elevated Mg with increased Al levels is recorded across a microcrack. Fig. 37 is included to demonstrate that in some instances, elevated impurity levels correspond with a complete loss of Zr, clearly indicating the presence of discrete secondary phases. In this example, elevated Mg is associated with elevated Si.

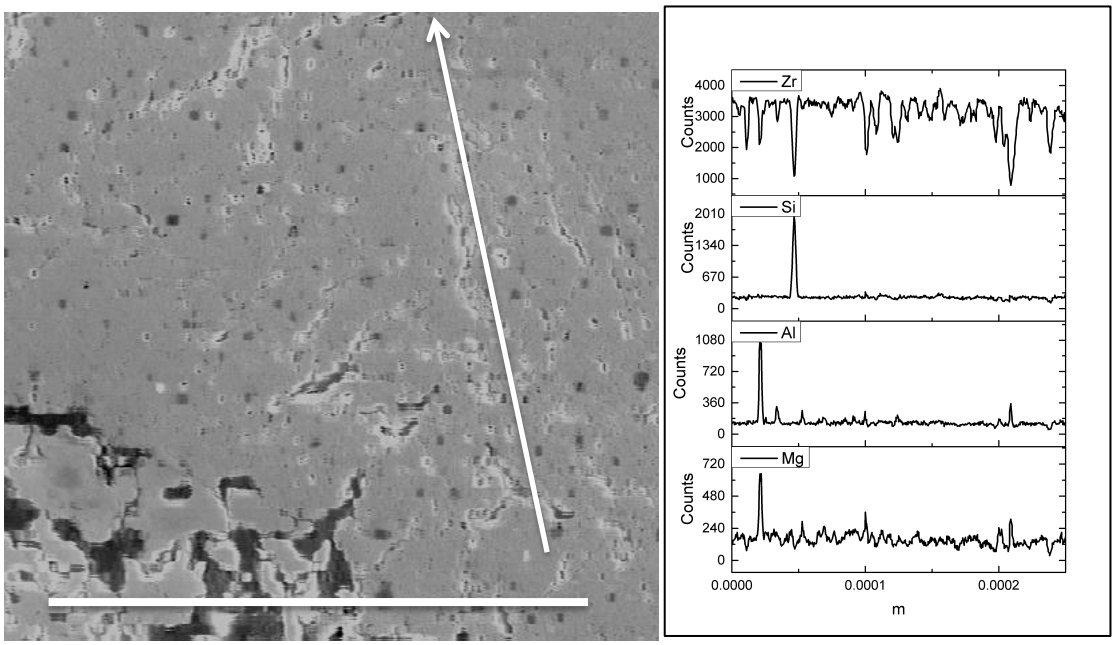

Figure 36 : SEM secondary electron image of an as-fired HP aggregate with microcracks. The corresponding 600s SEM-EDS linescan is plotted from left to right, corresponding to the arrow direction Scalebar 200 µm.

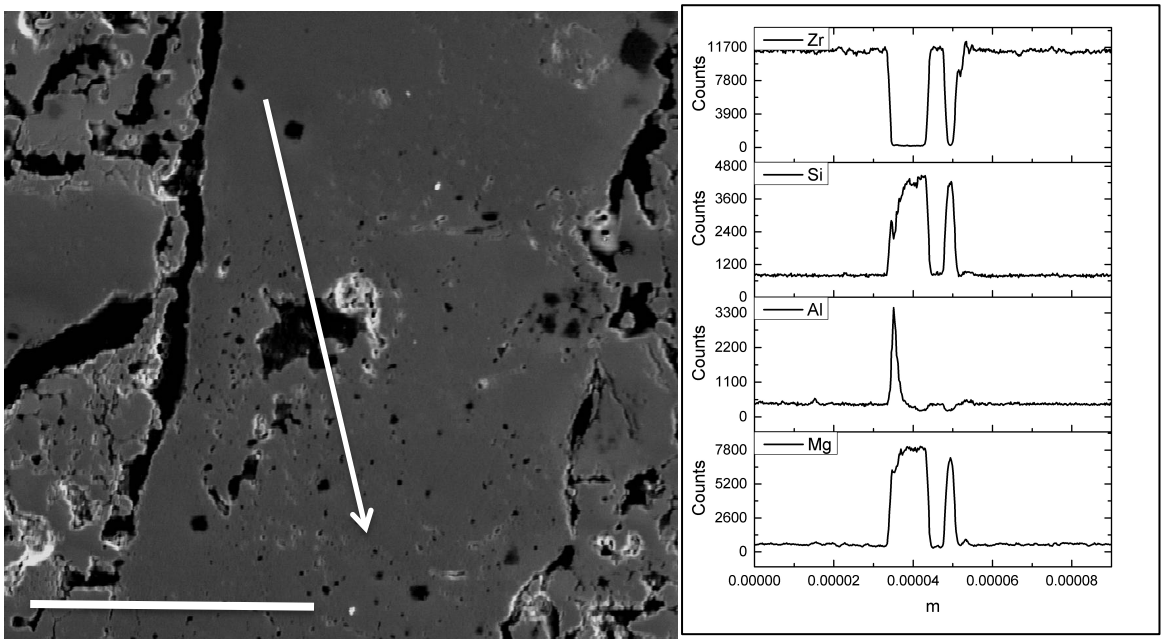

Figure 37 : SEM secondary electron image of an as-fired HP aggregate with large interior pore with secondary phase. The corresponding 600 s SEM-EDS linescan is plotted from left to right, corresponding to the arrow direction. Scalebar 80 µm.

Mg-Al, Mg-Si and Mg-Al-Si element associations were quantified in seventeen SEM-EDS point analyses of the interstitial material between subgrains in both as-fired and cycled aggregates of the LP and HP refractories. In Fig. 38, these data are plotted within a 1300 °C isotherm of the ternary MgO-Al_2O_3-SiO_2 phase diagram due to insights gained from a thermodynamic modeling exercise (see 4.1.4 below). The compositions of the interstitial material straddle five regions of phase co-stability, with the stable phases including periclase (MgO), spinel ($MgAl_2O_4$), forsterite (Mg_2SiO_4), cordierite ($Mg_2Al_4Si_5O_{18}$), pyroxene ($Mg_4Al_{10}Si_2O_{23}$) and an unidentified phase ($Mg_4Al_{10}Si_2O_{23}$).

Allowing for the high relative error on SEM-EDS data (±25%)[89], the results in Fig. 38 can be interpreted to fall roughly into two groups, denoted "forsterite group" and "spinel group" in recognition of the Mg-Si dominance in the former and Mg-Al dominance in the latter. Fig. 39 illustrates the degree of variation in secondary phase compositions obtained within a single aggregate. It is possible to observe a forsterite-like and spinel-like phase within 70 µm of each other.

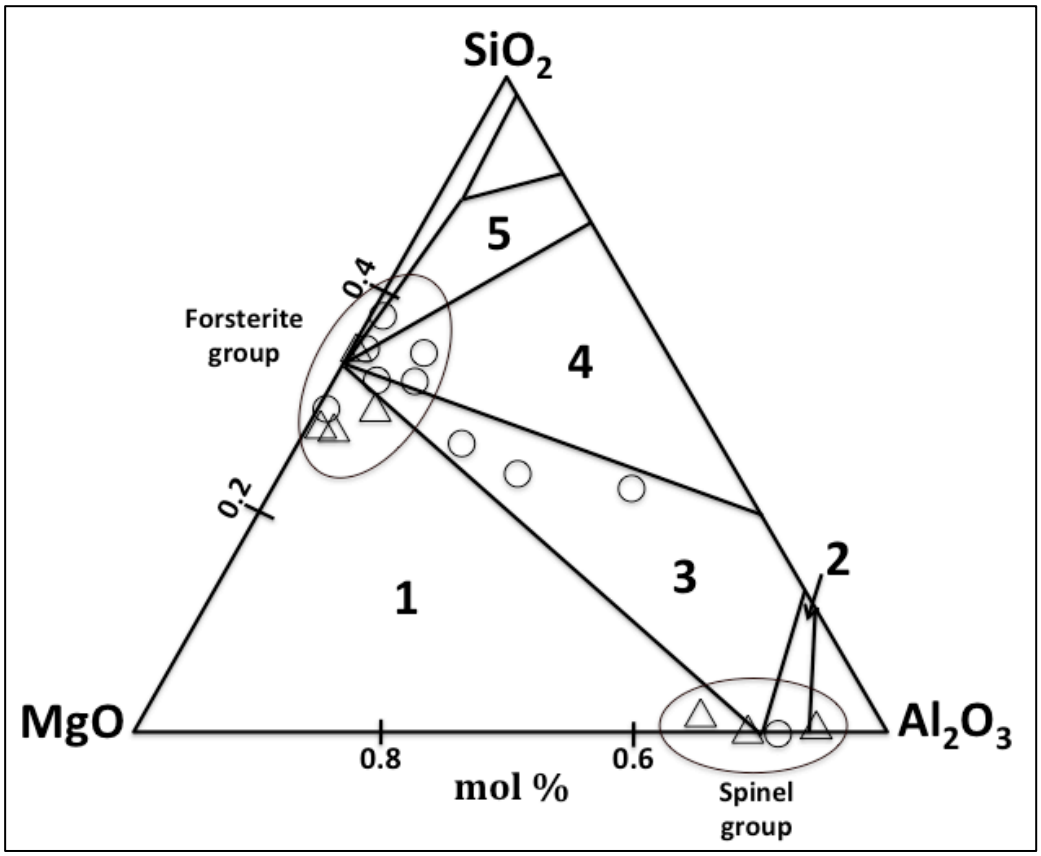

Figure 38 : SEM-EDS analyses for interstitial secondary phases plotted in a 1300 °C isotherm of the ternary MgO-Al_2O_3-SiO_2 phase diagram (generated by FactSage 6.2; cropped at >40% MgO). Circles - LP refractory; triangles - HP refractory; Co-stability regions: 1 - spinel + periclase + forsterite; 2 - spinel + $Mg_4Al_{10}Si_2O_{23}$; 3 - spinel + forsterite + $Mg_4Al_{10}Si_2O_{23}$; 4 - forsterite + cordierite + $Mg_4Al_{10}Si_2O_{23}$; 5 - pyroxene + forsterite + cordierite. Data appear to fall within two (circled) groupings.

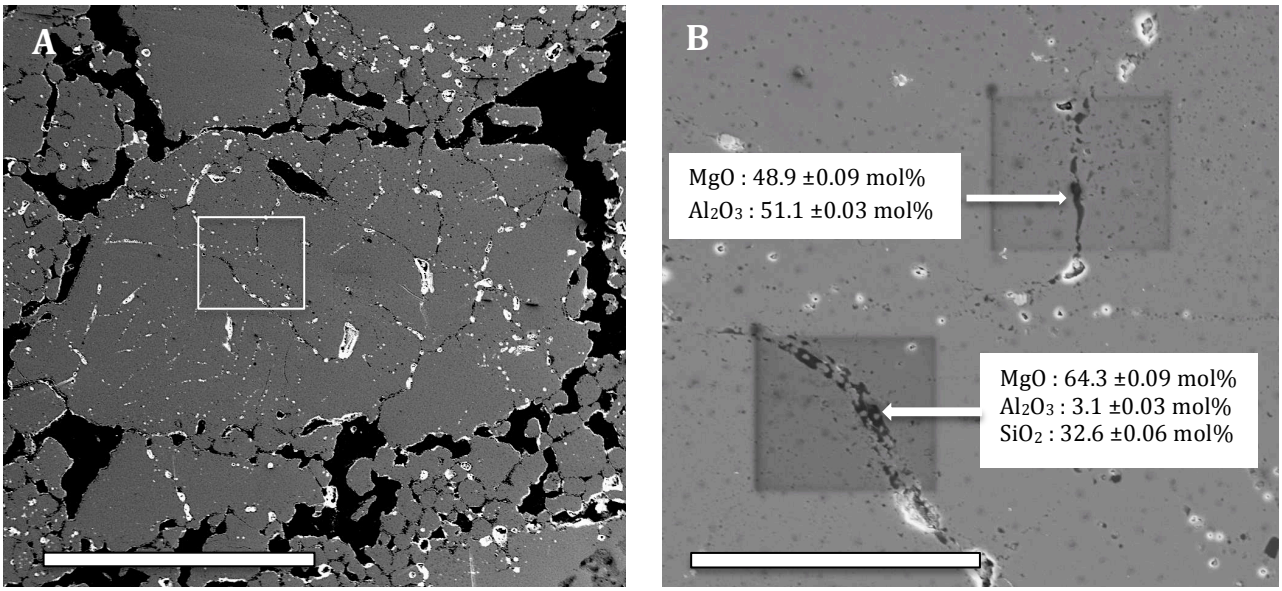

Figure 39 : Secondary electron images of an aggregate from a cycled LP sample, displaying extensive subgraining (A). Boxed area is shown on the right (B) as higher magnification section across two subgrain boundaries. SEM-EDS compositions are displayed, the upper one being spinel-like and the lower forsterite-like. Scalebars : 500 µm (A) and 70 µm (B).

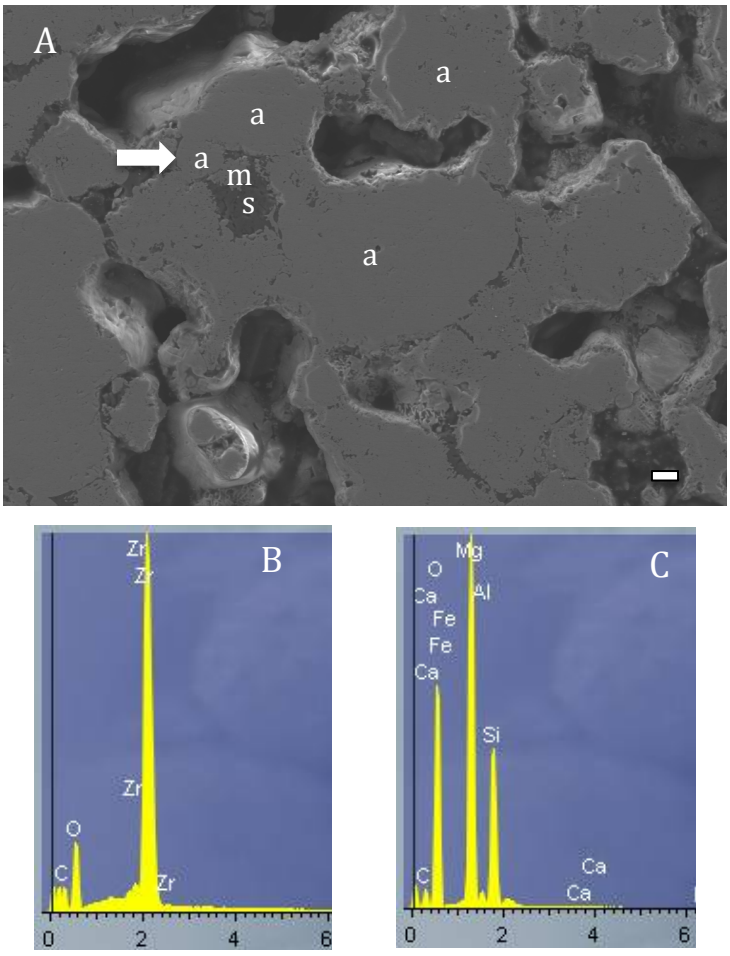

Figure 40 : A - Secondary electron image of SA refractory after 8 cycles; 'a' denotes aggregates, 'm' a matrix particle and 's' a secondary phase. Scalebar : 10 µm. B - SEM-EDS spectrum for the aggregate marked with arrow. C - SEM-EDS spectrum for secondary phase. X axes on SEM-EDS spectra are keV and Y axes are intensity.

Secondary phases are also observed in the SA refractory; not within the aggregates, but at the interface between aggregates and matrix particles (Fig. 40). SEM-EDS analysis of these secondary phases yields elevated Mg, Al and Si levels once again(Fig. 40C).

4.1.5. Thermodynamic modeling

Table 4 summarizes the inputs for, and outputs of, a thermodynamic calculation in which an average aggregate composition for the LP refractory and the HP refractory was equilibrated at 1700°C, to determine whether a liquid phase would be generated.

Table 4 : SEM-WDS inputs and FactSage 6.2 outputs in modeled equilibration at 1700 °C.

Sample	FactSage inputs	FactSage outputs	
	Average aggregate composition for as-fired aggregates without microstructural modification (wt%) = C	**Average composition C, equilibrated at 1700 °C, produces this liquid (wt%) = L**	**Composition of liquid L converted to mol % while removing the Zr component**
LP (n=14)	ZrO_2 - 96.7 MgO - 2.57 HfO - 2.12 Al_2O_3 - 0.176 SiO_2 - 1.45	ZrO_2 - 1.98 MgO - 39.1 Al_2O_3 - 5.33 SiO_2 - 53.5 **in 2.7 g of liquid**	MgO - 50.7 Al_2O_3 - 2.73 SiO_2 - 46.6
HP (n=46)	ZrO_2 - 97.1 MgO - 2.41 HfO - 2.11 Al_2O_3 - 0.30 SiO_2 - 0.09	ZrO_2 - 2.17 MgO - 35.5 Al_2O_3 - 12.9 SiO_2 - 49.4 **in 0.18g of liquid**	MgO - 48.1 Al_2O_3 - 6.91 SiO_2 - 45.0

n is the number of aggregates averaged. SEM-WDS typical errors : ZrO_2 - 1.6 wt%, MgO - 0.05 wt%, HfO - 0.06 wt%, Al_2O_3 - 0.02 wt%, SiO_2 - 0.02 wt%; note that SEM-WDS total may not add to exactly 100% but relative proportions are carried through the calculations.

Results from the modeling indicate that small quantities of liquid will form (with more liquid formed in the LP aggregates than the HP aggregates). The liquids comprise predominantly magnesia and silica, with lesser concentrations of alumina and around just 2 wt% ZrO_2. Since the solubility of zirconia is low (<10 mol%) in a MgO-Al_2O_3-SiO_2 glass at 1700 °C[38], these liquid compositions were normalized to remove the zirconia component. The two resulting liquid compositions, which are predictably similar, are plotted in a ternary MgO-Al_2O_3-SiO_2 phase diagram (Fig. 41) and fall within the forsterite stability field.

In a separate thermodynamic calculation, isopleths were generated for the liquid stability phase in the equilibrated MgO-Al_2O_3-SiO_2 system from 1800 °C to 1300 °C. The results are presented in Fig. 42. A liquid phase is present from 1800 °C to approximately 1373 °C. Below ±1370 °C, all stable phases are solid.

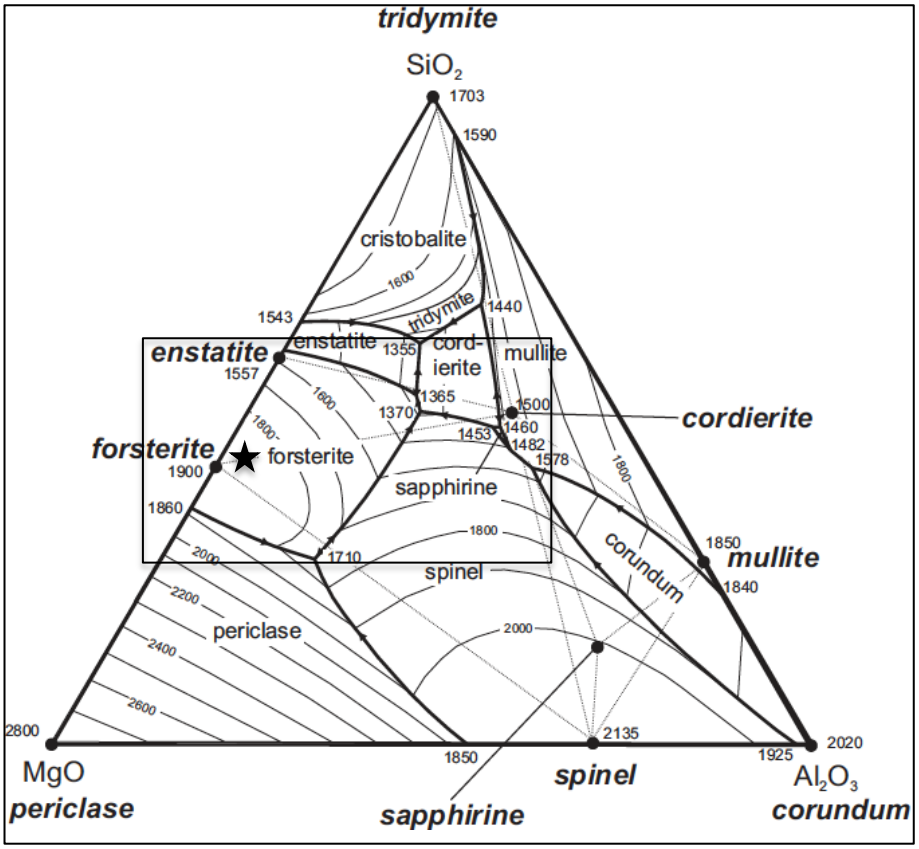

Figure 41 : The MgO-Al_2O_3-SiO_2 phase diagram developed by Osborn and Muan[119] and modified from Levin[120]. Star indicates average liquid composition generated by the LP and HP aggregates at 1700 °C. The boxed section is magnified in Figure 52 in Section 4.2.1. below.

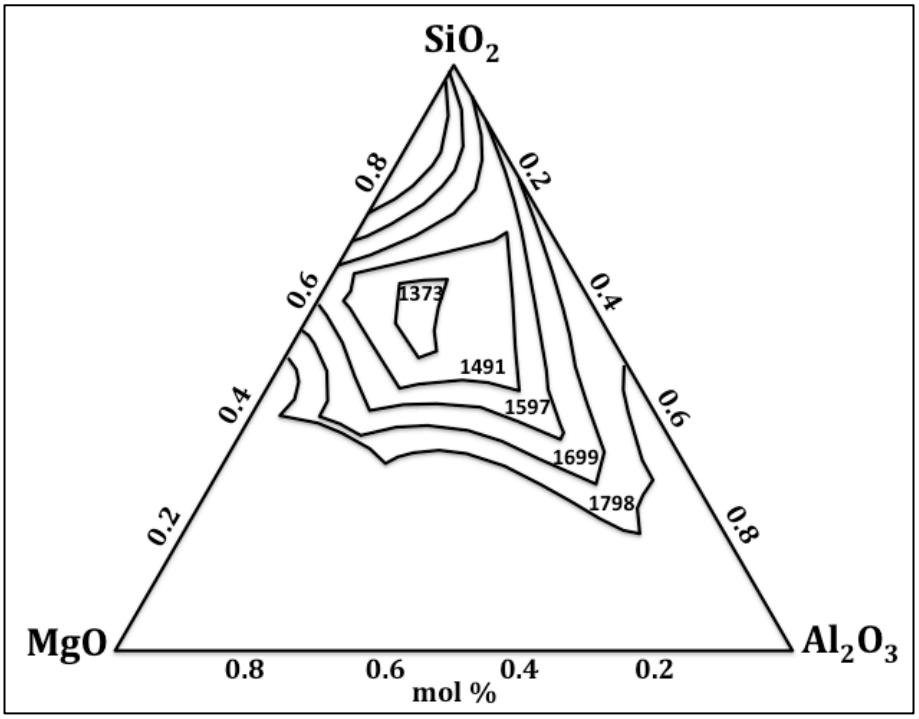

Figure 42 : Projected liquid stability field from 1800 °C to 1300 °C C for the equilibrated MgO-Al_2O_3-SiO_2 ternary system. Isotherms are labeled in degrees Celsius.

4.1.6. Phase variation

Having investigated local composition gradients, it was deemed useful to evaluate local variations in phase (using XRD, Raman and TEM) to establish whether, and to what extent, loss of stabiliser had triggered zirconia polymorph transformation. Distinguishing between the monoclinic, tetragonal and cubic phases of zirconia proved challenging in the resulting Raman and TEM data but these techniques usefully revealed other local variations in mineralogy.

4.1.6.1. X-ray Diffraction

XRD spectra acquired before and after eight thermal cycles for all three refractories are presented in Figure 43. Using the method of Garvie and Nicholson[95], the intensities of the monoclinic peaks at 28° (11$\underline{1}$) and 31.5° (111) were ratio'd against total intensity for both the monoclinic peaks and the combined tetragonal/cubic peak at 30° (111) to establish the proportion of monoclinic polymorph present in the samples (Table 5). Consistent with its microstructure dominated by baddeleyite aggregates, the SA refractory comprises 92% monoclinic zirconia in its as-fired state and this proportion remains roughly constant at 90% after cycling. The HP refractory has roughly half this amount of monoclinic polymorph after firing (56%) and the microstructure remains surprisingly constant during thermal cycling (57% monoclinic after 8 cycles). In contrast, the as-fired LP refractory starts with 62% monoclinic zirconia and loses tetragonal/cubic constituents to transformation, resulting in a 26% increase in overall monoclinic content after 8 cycles (to 78%).

Table 5 : Measured XRD intensities in the 28-32° two theta range, used to calculate monoclinic proportions.

Sample	Monoclinic (111) intensity (counts)	Monoclinic (11 ī) intensity (counts)	Tetragonal / cubic (111) intensity (counts)	Total monoclinic intensity (counts)	Total intensity (counts)	Proportion of monoclinic polymorph (%)
uncycled SA	4406	5772	882	10178	11060	92.03
cycled SA	3755	3981	888	7736	8624	89.70
uncycled HP	10408	10489	16270	20897	37167	56.22
cycled HP	1488	1618	2359	3106	5465	56.83
uncycled LP	5334	6120	6989	11454	18443	62.10
cycled LP	1803	1018	780	2821	3601	78.34

Peak fitting of reference ICDD (International Centre for Diffraction Data) diffraction peak files for forsterite (e.g. 01-071-0792, 00-001-1290) magnesia aluminate spinel (00-001-1154 and delta phase (01-080-0967) against the acquired spectra did not yield any matches. Nor did a cordierite ideal diffraction spectrum, generated from a crystal information file for this mineral

(9007016.cif). This suggests that any secondary phases present are either amorphous (glassy) or fall below detection thresholds (±5%) for this bulk surface technique.

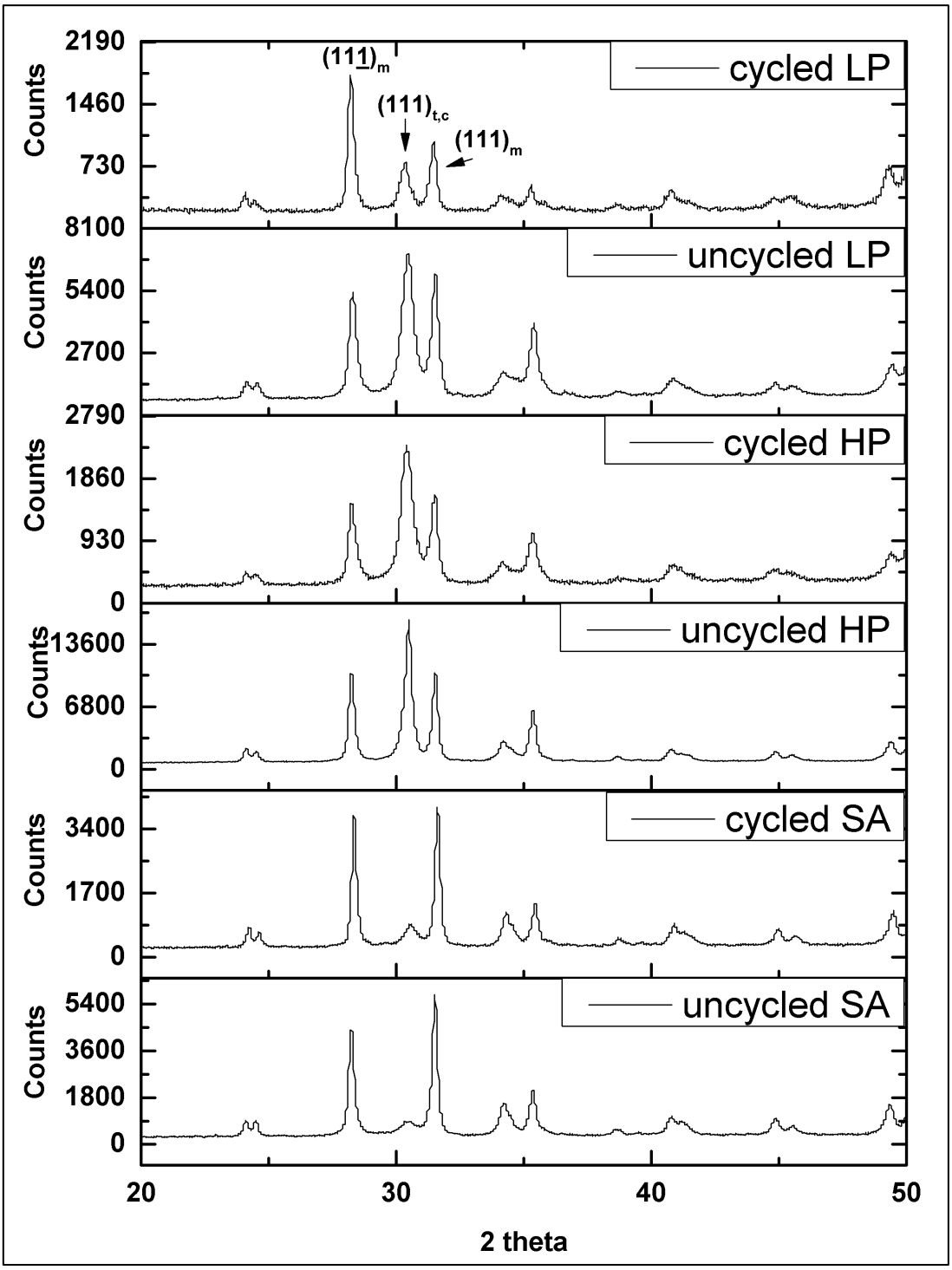

Figure 43 : XRD results, pre- and post-cycling, for thin solid samples of the three refractories. Peak attributions in the 'cycled LP' spectrum apply to all subsequent spectra at the same 2 theta values.

4.1.6.2. Confocal Raman Microscopy

Because Micro-Raman mapping has shown promise at identifying polymorph changes within and around zirconia grain boundaries[99], the technique was applied here in the hope of achieving similar outcomes. Raman mapping across several dozen LP and HP aggregates, as-fired and cycled, yielded two repeatable Raman signatures ('High wavelength' and 'Low wavelength' respectively, in Fig. 44A) as well as various mixtures (e.g. 'Mixed 1,2', Fig. 44A) of these two distinct spectra. It has previously been demonstrated[98] that hybrid Raman spectra for zirconia doped with Ca stabilizer can be directly linked back to the spectra for pure tetragonal and cubic forms but these two 'end-member' signatures and their 'hybrids' do not correspond with documented Raman spectra for pure monoclinic, tetragonal and cubic zirconia polymorphs (Fig. 45). A number of reference minerals were analyzed, to try and identify other mineral phase/s which might contribute, especially to the low wavelength (i.e. high wavenumber) signature.

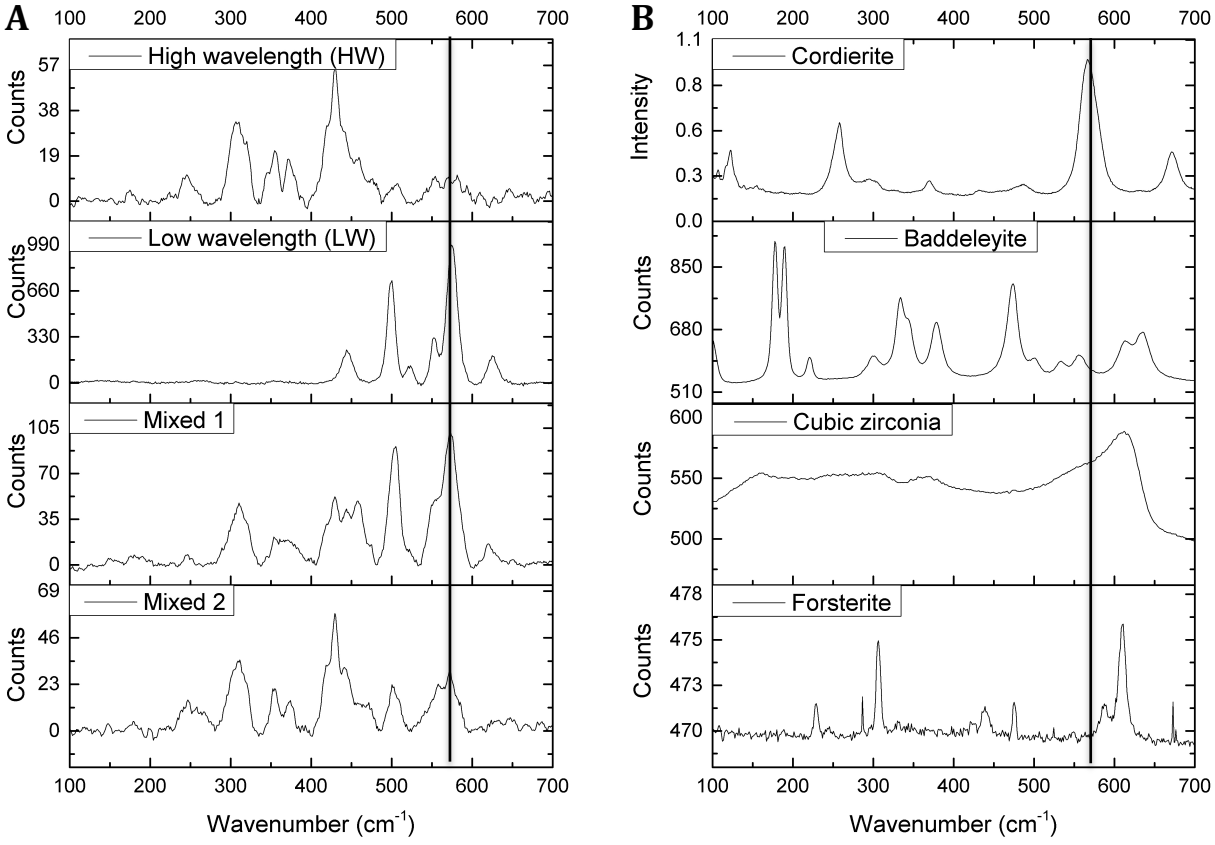

Figure 44 : Raman spectra obtained with 532 nm laser source. Spectra in A are representative end-members (HW and LW) and examples of the type of mixed spectra obtained, representing hybrids of the end-members. Spectra in B were acquired for three Natural History Museum reference minerals (baddeleyite = monoclinic zirconia) and a published dataset for cordierite[121]. The latter is the only spectrum collected here using a 514.5 nm source. The vertical lines allow comparison of the 572 cm^{-1} peak between zirconia and reference materials.

Raman spectra acquired on loaned specimens of baddeleyite (monoclinic zirconia), cubic zirconia, and forsterite, as well as a published Raman dataset for orthorhombic cordierite[121], are presented in Fig. 44B. Evaluating the reference and refractory results, the following is noted :

1. The baddeleyite result corresponds well with the reference monoclinic spectrum in Fig. 45, suggesting that no peak shifting has occurred at low wavelengths on the Raman system used here.
2. A dominant and characteristic peak at 572 cm^{-1} in the LW and 'Mixed' spectra results is consistent with published spectral images and peak tables for cordierite[122] [123], and corresponds well with the 570 cm^{-1} peak in the published dataset plotted for cordierite in Fig. 44B. In light of the SEM-EDS results in Section 4.1.4., this peak is therefore attributed to cordierite in the zirconia results.
3. A possible contribution to the low wavelength peak at 620 cm^{-1} in the refractories' spectra might come from the peak of the same wavelength for forsterite.

Recently published, high quality Raman spectra for magnesia-aluminate spinel[124] and enstatite[125] show dominant peaks below 400 cm^{-1} and above 600 cm^{-1}, overlapping several of the zirconia peaks but distinct from the cordierite spectrum.

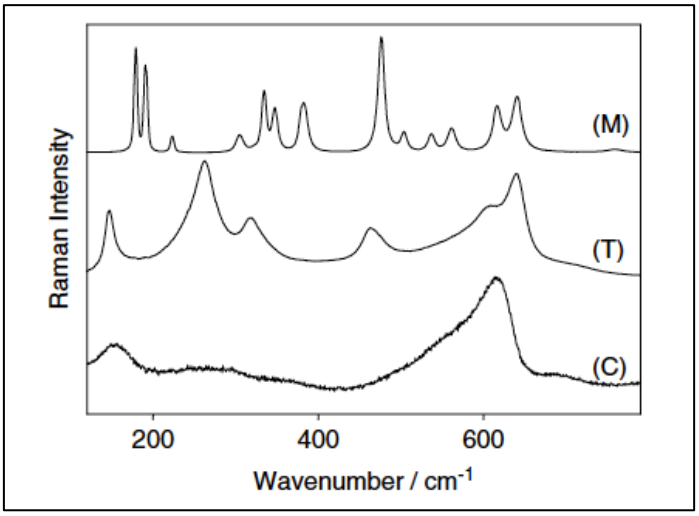

Figure 45 : Characteristic Raman spectra for the three zirconia polymorphs : C - cubic, T - tetragonal, M - monoclinic. Reproduced, with permission, from Gazzoli et al[98].

It is possible to obtain more than one apparently unique Raman spectrum from a material, due to multiple orientations of the crystals within that material[126]. However, the Raman signatures

acquired correlate consistently with microstructural features and therefore appear to reflect the link between composition and microstructure.

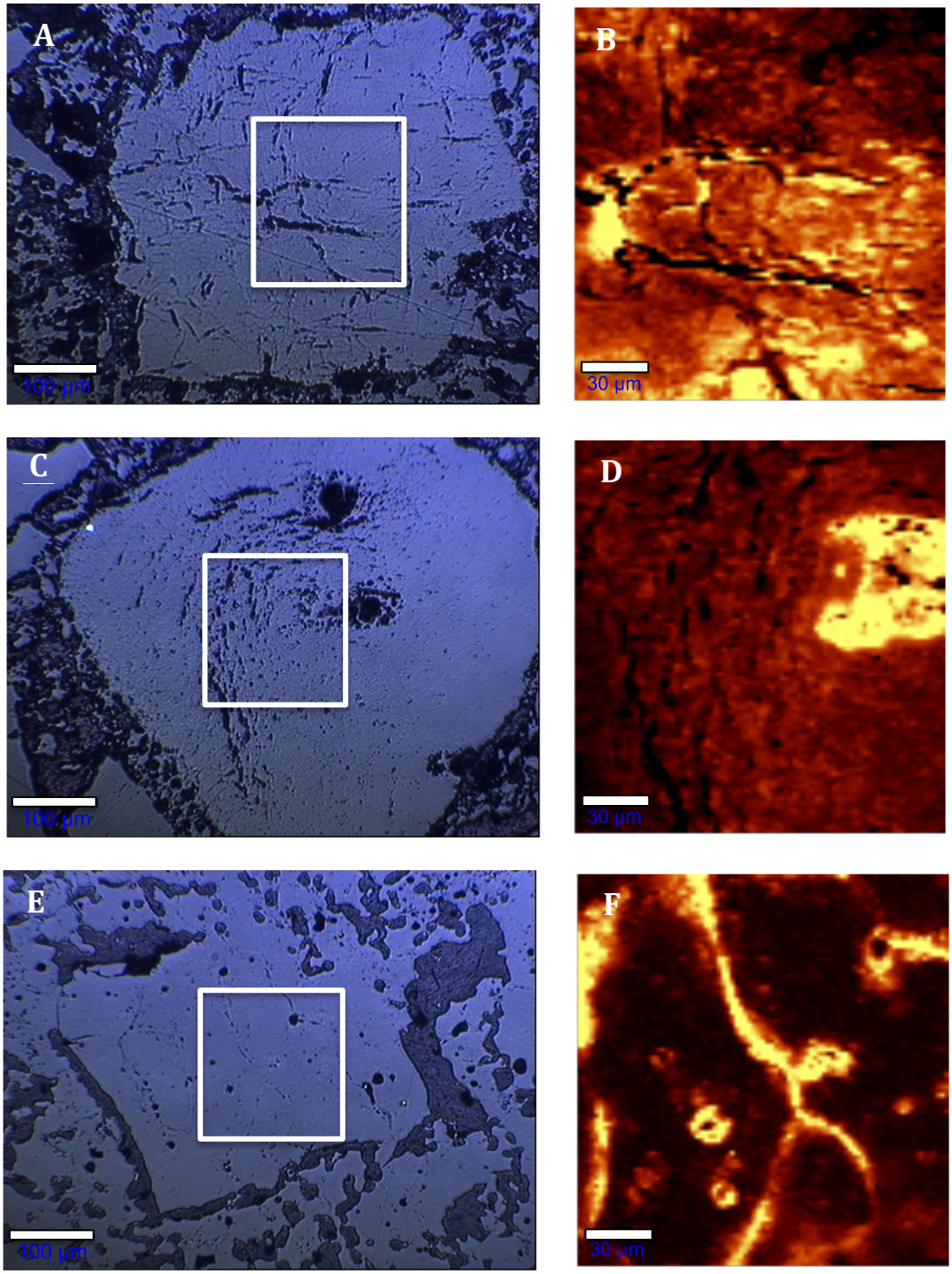

Figure 46 : Optical microscope images with the corresponding Raman map for each highlighted region. A - as-fired HP aggregate with microcracking; C - HP aggregate after 8 cycles, with large internal pores; E - HP aggregate after 8 cycles showing internal grain boundaries as secondary phases . The bright phase in Raman maps B, D and F represents the integrated intensity in the 560-590 cm^{-1} region of the Raman spectra, attributed to cordierite. Scale bars are 100 µm for optical images and 30 µm for the Raman maps.

Mapping of the 560-590 cm^{-1} spectral region across many of the aggregates reveals a clear association between this cordierite peak and areas of microstructural discontinuity (Fig. 46). Around internal fractures (microcracks), the cordierite is widely dispersed (Figs. 46 A and B), but adjacent to pores (Figs. 46 C and D), there is a more limited concentric distribution (±30 microns), indicative of cordierite diffusion into or out of these pores.

Where cordierite defines internal grain boundaries (Figs. 46 E and F), it has a width of approximately 10 microns and similarly sized 'haloes' are evident around small pores within these subgrains. In Figures 47 A and B, a zone of pores is observed to run parallel with the aggregate rim, again suggesting a diffusion front. Cordierite straddles the pore zone with a 30-40 micron wide continuous Raman signature.

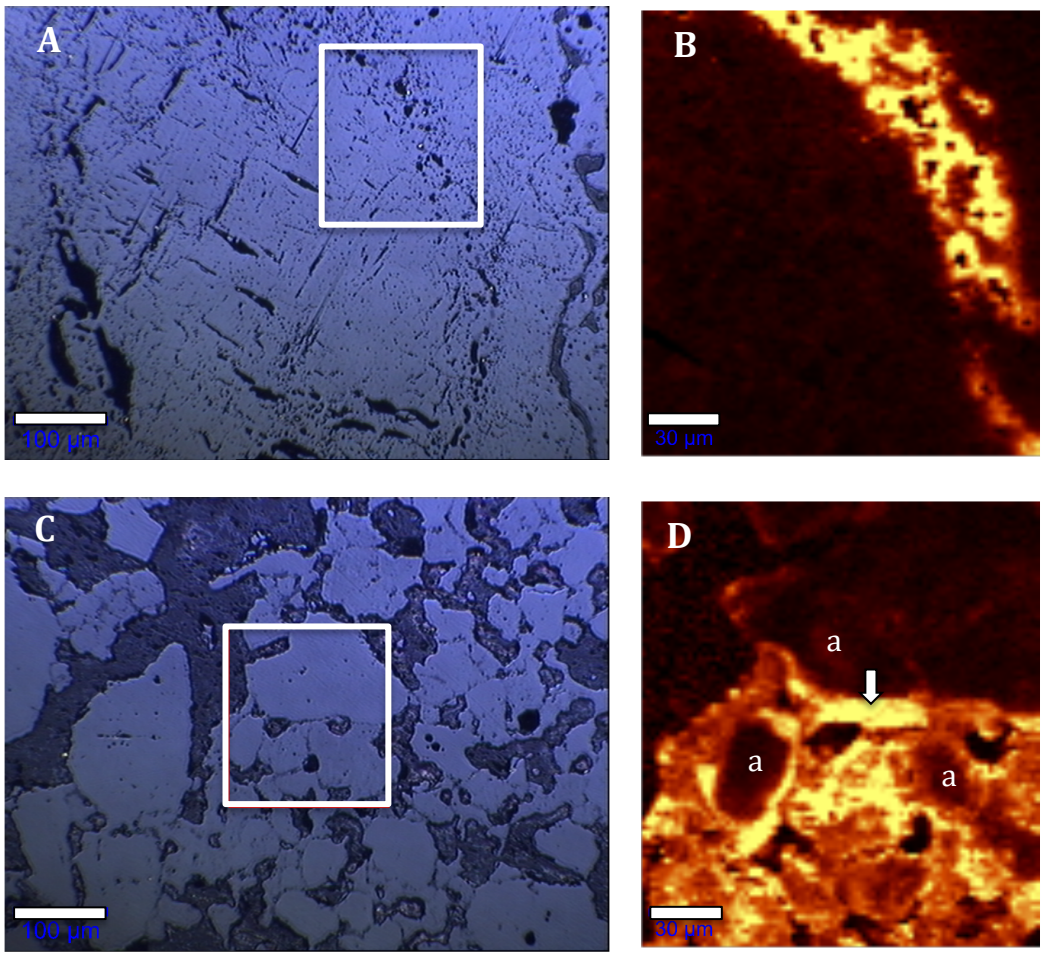

Figure 47 : Optical microscope images with the corresponding Raman map for each highlighted region. A - LP aggregate after 8 cycles, with central microcracks and a peripheral ring of concentrated pores; C - SA refractory after 8 cycles showing cluster of aggregate ('a') and matrix phases in centre. The bright phase in Raman maps B and D represents the integrated intensity for the 560-590 cm^{-1} region of the Raman spectra, attributed to cordierite. The bright region highlighted by arrow in image D is not matrix, but rather a rim area of the large aggregate, believed to have been modified by secondary phases. Scale bars are 100 µm for optical images and 30 µm for the Raman maps.

Cordierite is also detected in the SA refractory (Figs. 47 C and D), at the interface between Mg-PSZ matrix particles and the baddeleyite aggregates (marked 'a' in Fig. 47 D). The Raman spectra for these aggregates (Fig. 48) reflect the fact that these grains do not contain stabiliser and are therefore monoclinic, with characteristic peaks at 180 and 192 cm^{-1} .

In Fig. 47D, the *relative* absence of a cordierite signature across the baddeleyite aggregates provides strong confirmation that the "low wavelength" Raman spectrum does not derive from pure zirconia. In the SA refractory, magnesia is present only in the matrix phase to begin with and, as has been noted in Section 4.1.3., gradually moves into the baddeleyite aggregates. The "low wavelength" signature must therefore derive from either Mg modification of the zirconia lattice or a secondary phase. Bauer et al.[127] produce an identical "low wavelength" Raman spectrum for a Ca-PSZ in an Al- and Si-modified steel refractory environment apparently devoid of Mg but open to Fe diffusion. Since the Fe-rich cordierite ($Fe_2Al_4Si_5O_{18}$) Raman spectrum yields the same 575 cm^{-1} peak as its Mg-rich counterpart[122], the cordierite attribution is felt to be sound.

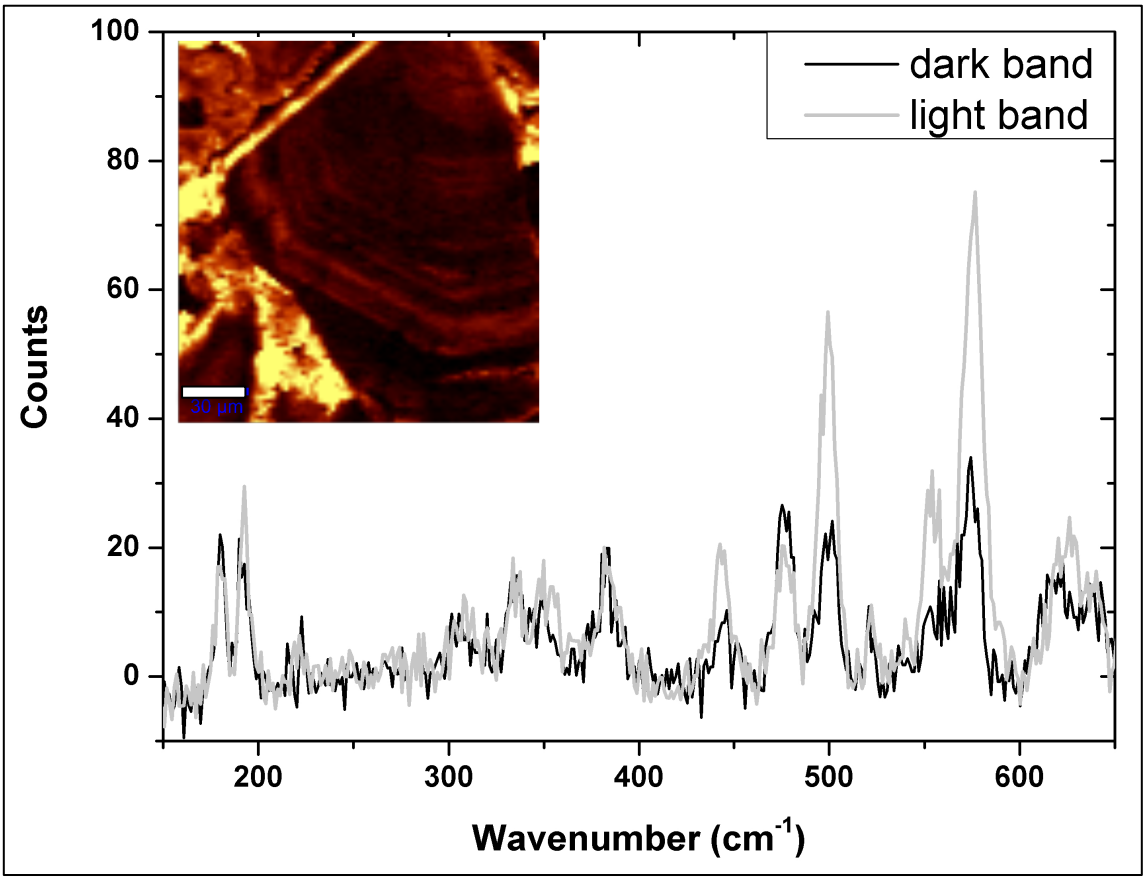

Figure 48 : Raman spectra for internal bands from an as-fired aggregate from the SA refractory. Inset : Raman map across an aggregate displaying internal banding.

Nevertheless, Fig. 48 (with very low count rates on the Y axis) also indicates the *marginal* presence of the 575 cm^{-1} peak in some SA aggregates, associated with fine banding that is suggestive of diffusion or stress gradients within the aggregates. The presence of trace amounts of cordierite in this situation could only be invoked through a process whereby Mg diffusing into the aggregates encounters slightly Al- and Si-enriched layers and undergoes a local reaction. It is noted that the banding inside the aggregate does not run parallel with its boundaries but is terminated on two sides. Within the aggregate, banding suggests an almost circular zonation that is not concentric with the aggregate borders.

Fig. 48 also demonstrates that whenever the cordierite peak is present, the zirconia peak at 500 cm^{-1} is also enhanced i.e. a true "low wavelength" (high wavenumber) signature, covering the 500-600 cm^{-1} spectral region appears to exist for these fused aggregates. The 500 cm^{-1} peak, usually carrying a monoclinic attribution, would be expected in regions of microstructural discontinuity and this link between monoclinic concentrations and secondary phases appears feasible.

4.1.6.3. Transmission Electron Microscopy

In Section 4.1.4., evidence is provided for segregation of the MgO stabiliser into secondary phases. It therefore becomes relevant to examine the phase evolution of the aggregates, with cycling, to determine whether this stabiliser removal triggers widespread polymorph transformation as has been noted elsewhere[53].

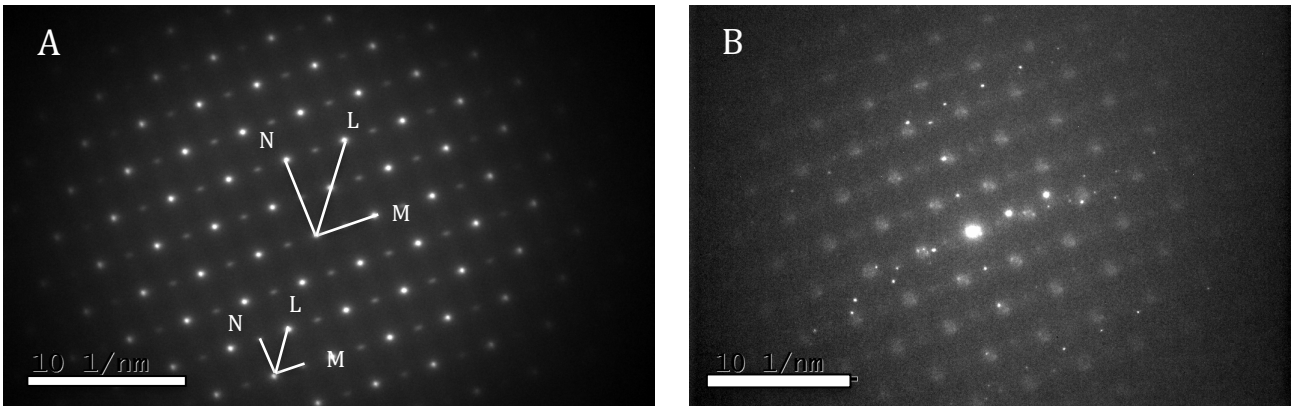

Figure 49 : SAED patterns for subgrain interior (A) and discrete phase within this subgrain (B) in disaggregating cycled LP aggregate. Scalebars : 10 nm^{-1}.

A selected area electron diffraction (SAED) pattern was found to be repeatable across a ±5 x 5 μm thinned area of a TEM foil extracted close to a subgrain boundary in a cycled LP aggregate (Fig. 49A). This region of the foil yielded a SEM-EDS spectrum comprising predominantly Zr with minor traces of Mg (Fig. 50A). Using reciprocal pairs of dots across a chosen centre dot, dot spacings from the SAED were used to calculate four potential d-spacings of 5.043, 3.625, 2.937 and 2.495 nm for the material.

Table 6 lists those d-spacings most closely matched to the calculated d-spacings, for phases expected to be present in the cycled aggregate, namely monoclinic, tetragonal and cubic zirconia and the delta phase, $Mg_2Zr_5O_{12}$. The similarity in d-spacings for these phases makes an unambiguous identification difficult.

Ratios of the dot spacings in Fig. 49A produce N/M = 1.4 and L/M = 1.72 with the angle between N and M approximately 54°. These geometries are characteristic of a body-centred cubic lattice configuration viewed from the [011] axis (ideal configuration[92] N/M=1.414 and L/M=1.732 with NM angle 54.7°). However, Kisi and Howard[5] have shown that a continuum in MgO concentrations in Mg-PSZ produces a sliding scale in unit cell parameters, with tetragonal phase 'c', and cubic phase 'a' converging as MgO values approach the eutectoid composition. Using equations (19) and (20), where 'x' is the mol fraction of MgO, the stabiliser range of 8-13 mol% for all cycled aggregates in this study produces a variation in tetragonal c-parameter of 5.121 - 5.080 nm and range of cubic a-parameters from 5.097 to 5.081 nm respectively. Under these circumstances, distinguishing between cubic and tetragonal lattices becomes challenging.

$$c_{tetragonal} = 5.1872 - 0.8246x \tag{19}$$

$$a_{cubic} = 5.122 - 0.3140x \tag{20}$$

One further observation is possible: The SAED result here gives no indication of the presence of a delta phase. The latter produces a distinctive rosette dot configuration in the SAED diagrams (Fig. 51), along with associated diffuse diffraction arising from the local ordering of oxygen vacancy sites[43].

A second SAED pattern (Fig. 49B) was obtained from a bright phase located at the edge of the thinned section of the TEM foil (Fig. 50B). This phase produces a SEM-EDS spectrum containing elevated levels of Mg, Al and Si, suggesting the presence of cordierite once more. The SAED pattern yields calculated d-spacings of 3.615, 2.686, 1.709 and 1.393 nm, which are compared with reference data for spinel, forsterite and cordierite in Table 6.

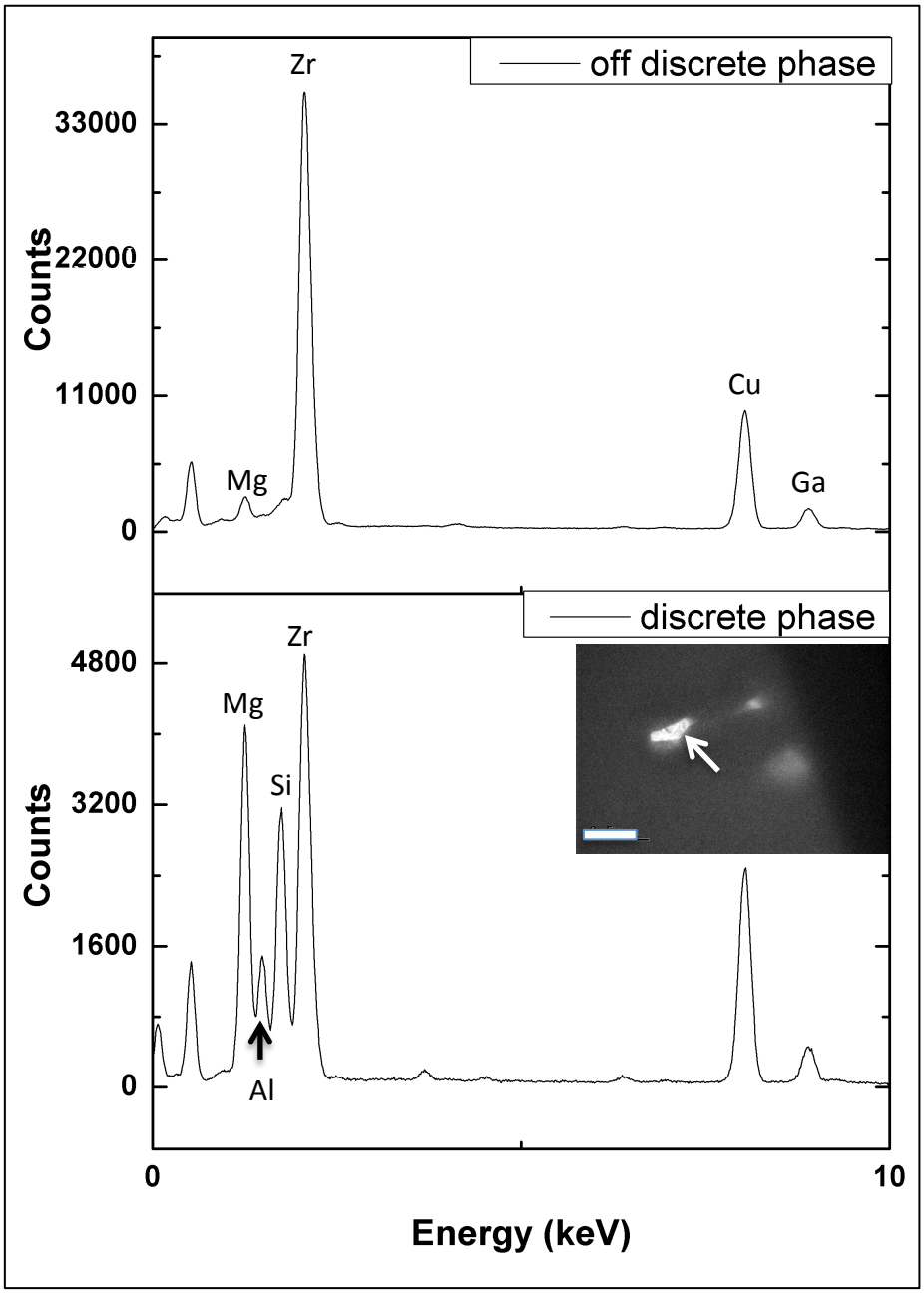

Figure 50 : SEM-EDS results from TEM selected areas. Inset micrograph shows plan view of region analysed with thinner section of foil in lighter grey on left. Three small, bright, discrete phases are present. The arrowed phase yields the 'discrete phase' spectrum with elevated Mg, Al, Si levels. Scale bar in micrograph is 0.5 µm.

Three possible matches to cordierite are noted although all three cannot be simultaneously true for one SAED pattern (i.e. a single crystal axis orientation). The diffuse nature of the majority of dots in the SAED pattern in Fig. 49B may indicate a thinner section of foil for this analysis, consistent with an internal pore[128]. Fig. 12 in Section 3.2.4. shows that internal pores filled with secondary phase can be found adjacent to those subgrain boundaries comprising secondary phases. This further supports the notion that it is the secondary phase cordierite that is represented in the SAED pattern of Fig. 49B.

Table 6 : Reference mineral powder diffraction data used to identify d spacing information relevant to SAED interpretation.

Mineral	hkl	d spacing (A°)
Monoclinic zirconia (00-003-0515)	011 100 110 a	3.64 5.10 3.70 5.21
Tetragonal zirconia(00-002-0733)	111 200 a c	2.93 2.52 5.07 5.18
Cubic zirconia (01-080-0964 /00-007-0337)	111 200 a	2.93 2.54 5.07
$Mg_2Zr_5O_{12}$ (delta)	003 21-2	2.93 2.52
Forsterite (01-071-0792)	130 060 233	2.76 1.70 1.39
Magnesia alumina spinel (00-001-1154)	422 531	1.64 1.36
Orthorhombic cordierite (9000545.cif from COD)	6 6 1 10 0 0 3 3 1	1.39 1.71 2.70

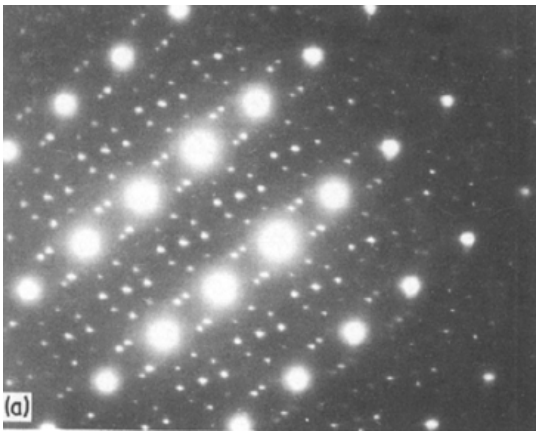

Figure 51 : Example of the diffuse electron diffraction pattern resulting from local anion ordering associated with delta phase formation. Reproduced, with permission[44].

4.2. Discussion

4.2.1. Secondary phase formation and distribution

Using well-constrained thermodynamic data for the MgO-Al_2O_3-SiO_2 system, it has been shown that the fused Mg-PSZ aggregates in LP and HP are capable of generating a liquid phase when cycled above 1700 °C (Section 4.1.5). Average LP aggregate compositions are slightly higher in Mg (by 0.1 wt%) and Si (±1.3%), relative to those in HP, but the liquids generated are similar enough, that a single representative composition can be plotted in the MgO-Al_2O_3-SiO_2 phase diagram ('L' in Fig. 52) to establish the sequence of phases that would be derived upon cooling. The first liquid formed would fall within the forsterite stability field and as the liquid cooled, it would therefore crystallize out this phase.

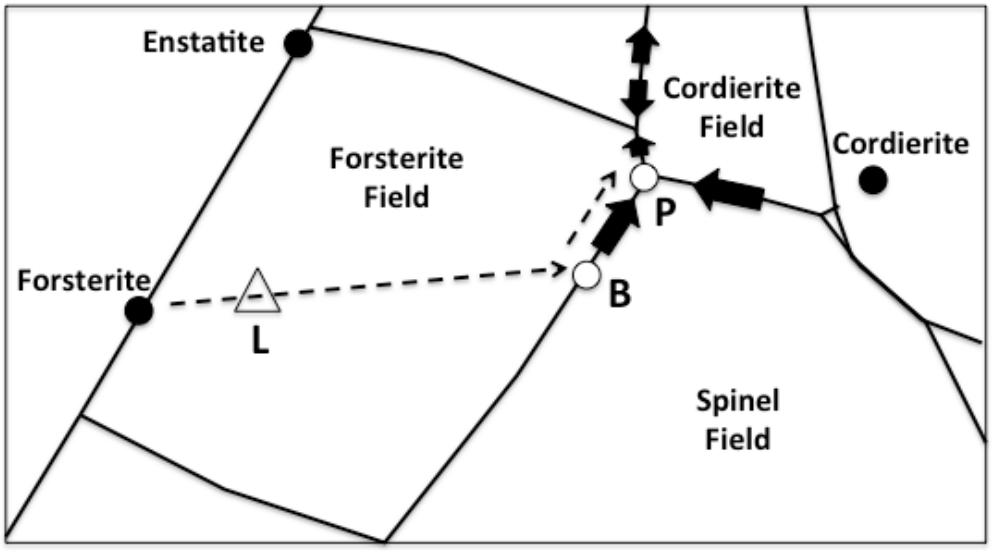

Figure 52 : Magnified section of the phase diagram in Fig. 13. Triangle L denotes a typical starting liquid composition for the as-fired LP and HP aggregates in ternary MgO-Al_2O_3-SiO_2 space at 1700 °C.

With forsterite removed, the liquid's composition moves on a chemical trajectory away from the forsterite end-member composition, down the thermal gradient of the ternary system (see Fig. 41), towards point 'B', which is the boundary curve between the forsterite and spinel stability fields. As the liquid composition reaches this cotectic, it resorbs forsterite and crystallizes spinel as a solid. Not all of the forsterite is consumed however, and both phases would be present in an aggregate around 1500 °C. The evolution path of the remaining liquid traces the cotectic line, down the temperature profile towards the peritectic point ('P' in Fig. 52). At approximately 1365 °C (see isopleths in Fig. 41), cordierite is crystallized at the further

expense of forsterite and all three phases should be found present. Thermodynamic equilibrium data for the MgO-Al_2O_3-SiO_2 system also showed that a liquid phase is only present to around 1350 °C, suggesting that no further crystallization would occur below this temperature.

The composition of the aggregates and the liquids they give rise to therefore indicate that forsterite, spinel and cordierite phases are to be expected in those regions of the aggregates where liquid segregation occurs. This is indeed what is found. In the secondary phases analyzed from subgrain boundaries within the LP and HP aggregates, compositions are consistent with forsterite, spinel and cordierite stability fields around 1300 °C and appear to cluster on either end of the phase boundary line linking forsterite and spinel, with some intermediate compositions along this line. This is consistent with the process described above, for cooling below 1500 °C: crystallization of spinel occurs at the expense of forsterite, producing a continuously changing ratio of the one phase, relative to the other.

Just as the liquid reaches cordierite compositions, it is also about to solidify. The last vestiges of liquid would not have had time to crystallize large grains and this phase might be expected to be finely disseminated between the larger remaining spinel and forsterite crystallites. This may explain why the latter two mineralogies dominate the secondary phase SEM-WDS results while cordierite presence only becomes substantial under the Raman technique which is capable of greater 'amplification' of minor physical and chemical units. Forsterite and spinel presence is not distinct within the Raman spectra but it is not precluded either. Raman mapping has shown secondary phase distribution to be wide within the LP and HP refractory aggregates - at microstructural 'edges' such as pores, subgrain boundaries and microcracks - and this distribution pattern is consistent with liquid segregation.

4.2.2. The impact of secondary phases

Formation of a secondary phase requires a change in molar volume, creating strain in the vicinity of newly crystallising minerals. Where spinel and cordierite are formed, the volume change is expansive (Table 7) whereas the creation of forsterite from the reaction between magnesia and silica results in a molar volume contraction, relative to the constituent components.

Table 7 : Summary of calculated volume expansions / contractions during secondary phase formation.

Precipitating phase	Reaction	Molar volume of reagents ($cm^3.mol^{-1}$)	Molar volume of reaction product ($cm^3.mol^{-1}$)	Volume difference (%)
Cordierite	$2\ MgAl_2O_4 + 5\ SiO_2 = Mg_2Si_5Al_4SiO_{18}$	193.5	225.0	13.99
Spinel	$MgO + Al_2O_3 = MgAl_2O_4$	37.01	40.08	7.651
Forsterite	$2\ MgO + SiO_2 = Mg_2SiO_4$	45.06	43.97	-2.497

In addition to volume expansion differences during phase formation, the newly formed phases themselves, behave differently in terms of their volume expansion coefficients in a thermal cycling environment. Table 8 contains linear thermal expansion coefficients for the secondary phases observed at subgrain boundaries in the LP and HP aggregates. Forsterite and cordierite both exhibit reduced expansion and contraction, on heating and cooling, relative to zirconia.

Table 8 : Comparison of linear thermal expansion coefficients for secondary phases observed.

Mineral phase	Coefficient of thermal expansion ($10^{-6}K^{-1}$) above 1000 °C
Zirconia	5 - 10 (determined for pre- and post- martensitic transformation)
Forsterite (Mg_2SiO_4)	2.8 – 4.5 (ave 3.7)[129]
Spinel ($MgAl_2O_4$)	7.6 – 9.2 (ave 8.4)[55]
Cordierite - ($Mg_2Si_5Al_4SiO_{18}$)	1.8 – 2.3 (ave 3)[130]

The (volume) shrinkage mismatch (S) between zirconia and these secondary phases can be calculated from Equation 21 where α_s and α_z are the coefficients of linear thermal expansion for the secondary phase and zirconia respectively[131].

$$S = 3(\alpha_s - \alpha_z)\,\Delta T \tag{21}$$

Taking into account the difference in crystallization temperatures in the liquid evolution sequence discussed in Section 3.3, the shrinkage mismatch is 3.1% for cordierite cooled from 1300 °C, 0.7% for spinel cooled from 1500 °C and 3.0% for forsterite cooled from 1600 °C, in zirconia. The thermal expansion volume differences for forsterite and cordierite, relative to zirconia, are of the same order of magnitude as that observed for the martensitic transformation. Microcracking due to the former is therefore considered quite plausible.

In one study of zirconia grains in a cordierite matrix, the expansion mismatch of zirconia transformation was in fact considered offset by the contraction mismatch between the grain

and matrix phases[131]. The geometry is different in this instance and the evidence for subgrain separation/fracture along boundaries characterized by secondary phases clearly visible. Fracturing may have occured due to both phase formation and phase expansion/contraction during cycling.

4.2.3. Differences between the refractories

The breakdown of aggregates in the LP refractory (>50% after 8 cycles) is substantially more prevalent than in aggregates within the HP refractory (<10% after 8 cycles). Several manufacturing differences exist between the two materials which might explain the difference in response to cycling: the presence of MgO fines in the LP matrix, the difference in binders and cold isostatic pressing conditions. However, the link between formation of secondary phase and fracture is clear. These secondary phases all lie within the Mg-rich portion of the MgO-Al_2O_3-SiO_2 system and it is therefore suggested that Mg concentrations dictate the degree to which secondary phase development, and thus fracture, occurs.

Thermodynamic modeling based on the composition of aggregates (but by extrapolation, also the matrix particles which are finer fractions of the same material) indicates that the LP refractory generates greater amounts of secondary phase liquid, in support of this proposition. Higher Mg ranges in the LP components (aggregate and matrix) are likely to be due in part, to the presence of Mg fines in this refractory, although this aspect of the microstructure was not studied in this work. . The SA aggregates, manufactured without Mg, but still containing Al and Si impurities, do not display any significant development of secondary phases or allied fracture. Their matrix phase, rich in Mg, yields a strong cordierite signature.

4.2.4. A model for aggregate breakdown

Solubility studies in single crystals, doped by ion implantation, provide a robust estimate of alumina solubility in zirconia up to 1600 °C: 0.2-0.3 wt%[54]. This range matches the alumina concentrations quoted by fused Mg-PSZ suppliers for their aggregates[46], and the concentrations recorded in this study for the as-fired aggregates in the LP and HP refractories. In other words, the aggregates entering the VIM crucible refractories contain alumina at the limits of its solubility within their zirconia lattices at service temperatures. The silica which

remains is present in even lower concentrations but has a high affinity for the alumina. Thus a simple model (Fig. 53) is proposed here to explain the aggregate breakdown observed.

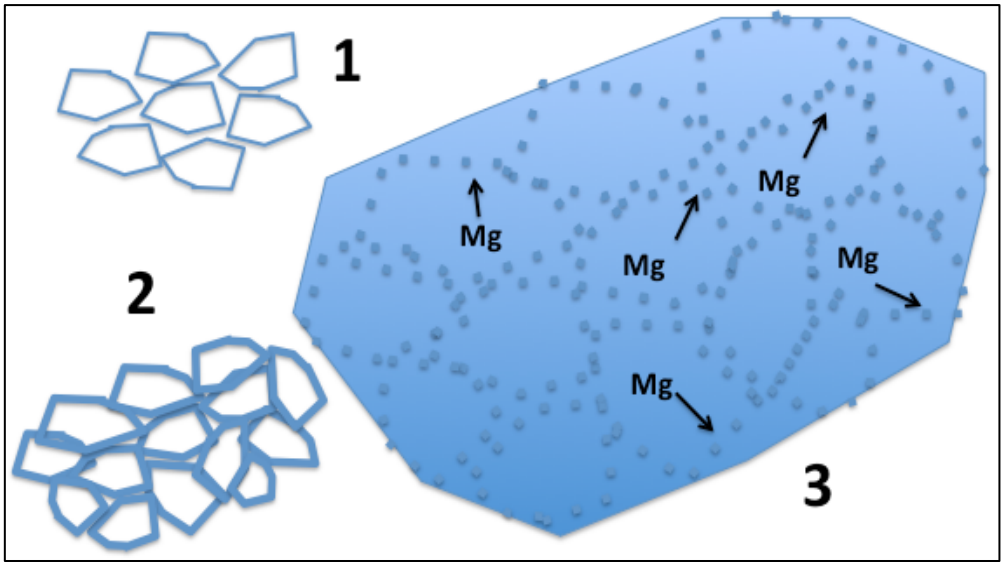

Figure 53 : Basic model for subgrain break-up of fused Mg-PSZ aggregates. Individual zircon sand grains (1) fuse at high temperatures with Al and Si impurities moving to the grain surfaces during the process (2). Fused Mg-PSZ aggregates are formed in which remnant sand particle boundaries represent areas of impurity concentration (3). MgO is scavenged by the impurity elements to form secondary phases along these remnant boundaries.

During the carbothermic reduction of zircon sand to make fused zirconia, it is proposed that alumina and silica diffuse to the zircon sand particle surfaces, the alumina displaying a greater affinity for silica than zirconia[52] (Steps 1->2, Fig. 53). Fusion largely eradicates the physical sand particle boundaries but does not entirely homogenize the resulting ingot so it retains a 'memory effect'. After fusion, crushed crystals retain local heterogeneities reminiscent of sand particle borders and may even retain zonation from the Al-Si diffusion process. (This aspect appears captured in some SA refractory aggregates (cf. Section 4.1.6.2 on zonation captured in the Raman mapping). These aggregates do not undergo a second fusion, for addition of stabiliser, and are therefore more likely, than their Mg-PSZ counterparts, to retain compositional history from the zircon sand source.)

In the second fusion step (in which MgO is added to zirconia to produce the Mg-PSZ ingot) local heterogeneities are exacerbated further as elevated alumina-silica regions effectively draw magnesia (Step 3, Fig. 53). This inhomogeneity of stabiliser has been noted in other zirconia aggregate studies[42]). The resulting MgO gradients in the final ingot explain the wide range of stabilizer contents 'arriving' in the final, crushed Mg-PSZ fused aggregates. The latter, once reheated during firing of the refractory and on subsequent service heats, increasingly give rise

to 'intergranular' liquids, located along remnant sand particle boundaries. Work reported by Aiba et al.[48] and Hino and Kiyota[49] (cf. Section 2.1.3) confirms the possibility of secondary phase evolution *within* refractory particles / aggregates. In addition, Mg fines within the matrix phases should produce secondary phase liquids of similar composition. The secondary phases which result, cause disaggregation through 1) fracture arising from their molar volume changes on formation and the subsequent thermal expansion mismatch between the zirconia and secondary phases, and 2) the infiltration of matrix-generated liquid phases which add to the volume strains during subsequent cycles.

Breakdown of the aggregates through phase transformation strains is an additional possibility but the work of French researchers[26] on high-alumina aggregates has shown strong crystallographic controls on the t-m domains which arise from cyclic transformations and the geometric arrangement of these domains matches the angles (109°) observed for microcracking in this study's samples (cf. Section 4.1.2. above and Section 5.1.2. below). Such microcracks are linear and often parallel and are therefore, highly dissimilar to the curvilinear geometry displayed by the subgrain boundaries attributed here to secondary phase formation.

In support of this proposed model, it is noted that the subgrain particle sizes observed in the broken down aggregates correspond with those of the size profiles quoted by zircon sand suppliers for sand used in the manufacture of fused zirconia (e.g. 29 cumulative wt% retained at 150 μm, 86 cumulative wt% retained at 106 μm and 99.8 cumulative wt% retained at 75 μm[132]).

5. THERMOMECHANICAL EVOLUTION

Having recorded the microstructural changes that arise on thermal cycling of the three commercial refractories, concurrent modification of bulk material mechanical behaviour was then evaluated - both during thermal cycling (thermal expansion, stiffness) and before and after eight thermal cycles (strength, toughness). As in the previous chapter, results will be presented here with low-level interpretation applied simultaneously, allowing a more narrative interpretation in the discussion section, where results from multiple techniques will be integrated.

5.1. Results

5.1.1. Thermal expansion

Dilatometry curves for two samples of the **LP refractory** are plotted in Fig. 54A. The heating slopes before onset of the m-t transformation and the cooling slopes after t-m transformation were used to determine 'low temperature' coefficients of thermal expansion (CTE). Similarly, heating slopes after m-t transformation and cooling slopes prior to t-m transformation were used to calculate a 'high temperature' CTE for each sample (Table 9).

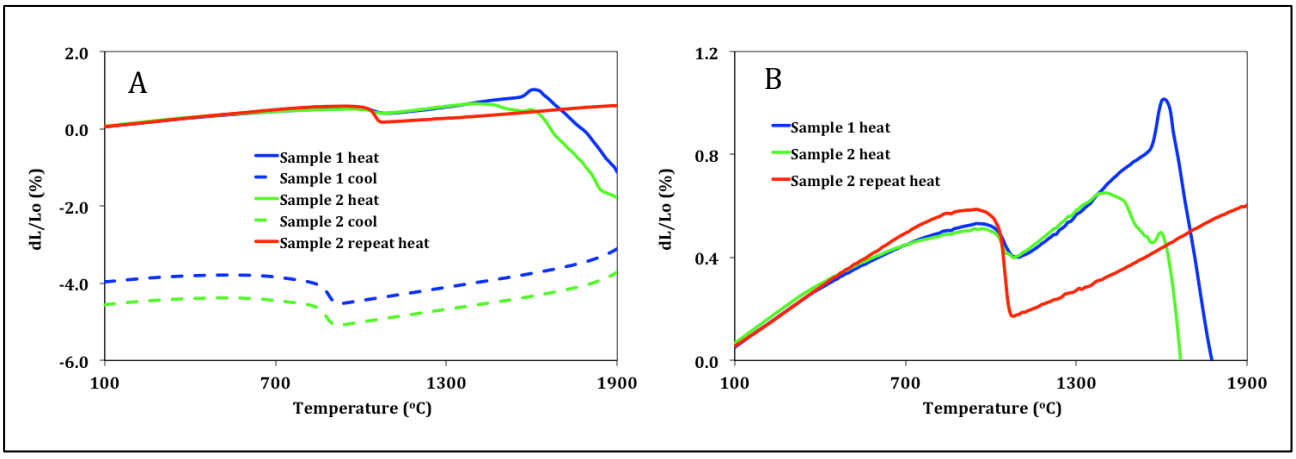

Figure 54 : Dilatometry results for the LP refractory. The heating curves in A are magnified in B.

The m-t and t-m transformation events were identified from the mid-curve regions of rapid strain and are quantified in Table 1. There is good repeatability between the two LP samples, both in terms of the heating and cooling CTE's as well as the onset and end temperatures of the

polymorphic transformations. The latter reveal a hysteresis - typical of martensitic events - of approximately 160°C between heating and cooling transformation events.

Onset temperatures for zirconia transformation have been linked to i) relative initial proportions of monoclinic and tetragonal phases, ii) level and distribution of stabiliser cations and iii) grain size and shape, among other factors[22]. Microcracking triggered by phase contraction during the first heat cycle will also alter the matrix constraints around tetragonal precipitates, modifying the thermodynamic conditions for transformation on cooling. Tetragonal precipitates may grow at the high temperature stage of heating too, altering the temperatures to which they remain stable during the cooling step.

Table 9 : Dilatometry data for the LP refractory. CTE's have been calculated on those segments of the dilatometry curves yielding >99% fit to a linear regression. Arrows indicate how the data chronology should be followed.

	Sample 1 heat	Sample 1 cool	Sample 2 heat	Sample 2 cool	Sample 2 reheat
Section of curve used to calculate low temperature CTE (°C)	100-700	400-100	100-700	350-100	100-700
Low temperature CTE ($10^{-6}.K^{-1}$)	6.69 ↓	5.37 ↑	6.42 ↓	5.73 →	7.43 ↓
Section of curve used to calculate high temperature CTE (°C)	1520-1120 ↓	1680-940 ↑	1100-1350 ↓	1600-900 ↑	1200-1800 ↓
High temperature CTE ($10^{-6}.K^{-1}$)	9.90 →	11.8	8.75 →	10.9	5.68
Midpoint of m-t transformation (°C) - inflection method	1040	-	1030	-	nd
Midpoint of t-m transformation (°C) - inflection method	-	880	-	870	-
Onset of m-t transformation (°C) - max temp method	950	-	940	-	950
Onset of t-m transformation (°C) - min temp method	-	920	-	920	-
Onset of m-t transformation (°C) - tangent method	±1000	-	±1010	-	±990
Onset of t-m transformation (°C) - tangent method	-	±900	-	±900	-
Linear m-t strain (dL/L_o) on heating (%)	nd	-	0.1	-	0.4

nd - not determined

A peak feature at 1580°C in the heating curves in Fig. 54 is an artifact, consistent with formation temperatures for ZrC[133], formed during zirconia contact with the dilatometer's graphite pushrod. This does not appear to have modified data insofar as the trends reported here occur in results that include the artifact as well as those that do not. After 1600°C, both samples contracted significantly on first heat (by ±4%) with this irreversible shrinkage attributed to further sintering, post firing. No further contraction occurred on reheating of the samples. A thermal expansion study done on zirconia brick as far back as 1925, shows exactly the same expansion trend, with m-t contraction at ± 1000°C and rapid shrinkage above 1600°C[134]. By comparison, dilatometry work by Caproni and Muccillo[135] on Mg-Y-doped

composite zirconia's produced linear shrinkage values of ±20% from first heat cycle sintering and reduction of this linear shrinkage (to ±1%), on reheating the same samples.

The low temperature CTE's for the LP refractory are almost half the value of the high temperature CTE's, *on first heat*, indicating that the increased presence of the tetragonal phase, post m-t transformation, enhances thermal expansion of the material as a whole (Table 9). This is due to the difference in CTE for the pure phases of monoclinic (±5 x $10^{-6}K^{-1}$) and tetragonal zirconia (±10 x $10^{-6}K^{-1}$)[6]. On cooling, some of the metastable tetragonal phase is converted to monoclinic, increasing the amount of this phase available for transformation during the next heat (i.e. the reheat in Fig. 54). Hence linear strain at the second m-t event increases from 0.1% to 0.4%. The larger strain may produce significant microdamage, reducing the high temperature CTE, as the latter is no longer elevated for the reheat sample as observed in first heat data.

Similarly, two samples of the **HP refractory** were tested and again, the second sample was cycled twice through the temperature programme (Fig. 55). Once more, consistent results are observed across samples. High temperature sintering produced permanent linear changes (between -2 and -7%) in both samples, but reheating triggered minimal further dimension loss (<0.5%). A slightly larger hysteresis (190 °C) was found between the m-t and t-m onset temperatures (Table 10), relative to the LP sample.

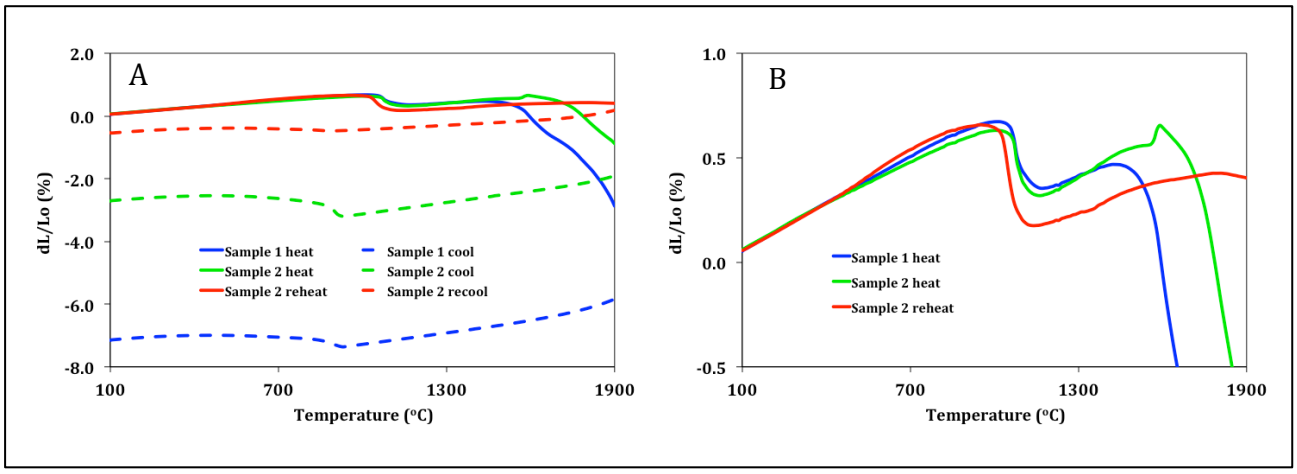

Figure 55 : Dilatometry results for the HP refractory. The heating curves in A are magnified in B.

CTE values are in the same range as determined for LP samples with slightly higher CTE values above the m-t event (12-14 x$10^{-6}K^{-1}$ as opposed to 9-12 x$10^{-6}K^{-1}$ for LP). On reheating, linear strain again increases (by 50%) from 0.31% to 0.48% (Fig. 55B) and similar to the LP behaviour, a reduced high temperature CTE is observed for the reheat.

Table 10 : Dilatometry data for the HP refractory. CTE's have been calculated on those segments of the dilatometry curves yielding >99% fit to a linear regression.

	Sample 1 heat	Sample 1 cool	Sample 2 heat	Sample 2 cool	Sample 2 reheat	Sample 2 recool
Section of curve used to calculate low temperature CTE (°C)	100-900	300-100	100-900	300-100	100-800	300-100
Low temperature CTE ($10^{-6}K^{-1}$)	7.36	6.07	6.72	6.09	8.12	5.75
Section of curve used to calculate high temperature CTE (°C)	-	1700-1200	1200-1500	1800-1100	1200-1700	1700-1000
High temperature CTE ($10^{-6}K^{-1}$)	nd	13.5	7.79	12.2	4.79	4.93
Midpoint of m-t transformation (°C) - inflection method	1080	-	1080	-	1050	-
Midpoint of t-m transformation (°C) - inflection method	-	890	-	910	-	860
Onset of m-t transformation (°C) - max temp method	1010	-	1010	-	950	-
Onset of t-m transformation (°C) - min temp method	-	930	-	930	-	890
Onset of m-t transformation (°C) - tangent method	±1060	-	±1060	-	±1020	-
Onset of t-m transformation (°C) - tangent method	-	±920	-	±920	-	±890
Linear m-t strain (dL/L_o) on heating (%)	nd	-	0.31	-	0.48	-

nd - not determined

A single sample of the **SA refractory** was tested by cycling four times through the temperature programme without the dilatometer chamber being opened (Fig. 56). High temperature sintering on the first heating cycle was offset by the very pronounced peak at 1580 °C, attributed to ZrC formation. A permanent linear reduction of ±2% occurred in both the first and second heats with no further shrinkage due to sintering in subsequent runs.

CTE values range from 3 x $10^{-6}K^{-1}$ to 7 x $10^{-6}K^{-1}$ (Table 11). Thermal expansion rates drop after each m-t transformation, perhaps due to microdamage caused by the event. There is some recovery at the start of the next heating cycle, but successive cycles result in lower CTE values for each pre- and post-transformation stage, relative to the corresponding stage in the previous cycle. This is indicative of a cumulative increase in the monoclinic content of the bulk refractory and therefore a degree of irreversible transformation.

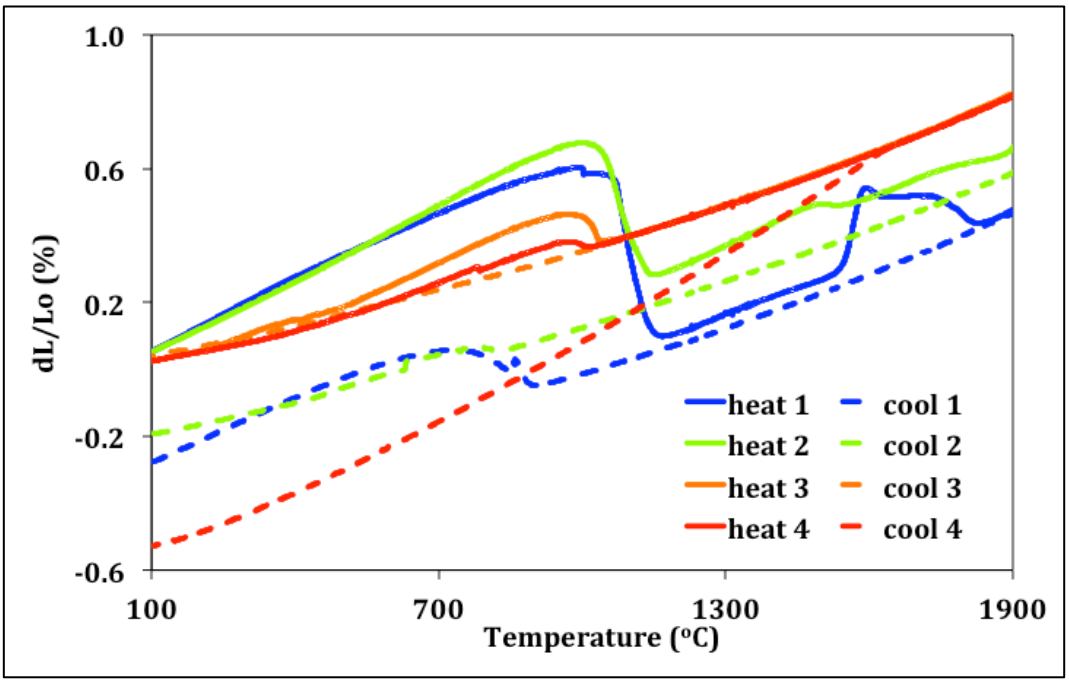

Figure 56 : Dilatometry results for the SA refractory.

A large hysteresis (>200 °C) was found between the m-t and t-m onset temperatures (Table 11), but disappears by the third heating cycle as the t-m event does not register by this step. There is a notable and systematic reduction in m-t transformation strain with successive cycling of the SA refractory, so that by the fourth cycle, linear contraction is approximately 4% of the strain recorded for the first cycle. This incremental reduction in m-t strain is directly opposite to the increase in m-t strain with cycling, for the LP and HP refractories. The SA sample also displays a steady decrease in the onset temperature for the m-t event : 1075 °C -> 1070 °C -> 1030 °C -> 1000 °C. In a dilatometry study on yttria-stabilised zirconia, Basu et al.[22] observe that transformation onset temperatures shift to higher temperatures (with lower volume fractions transformed) with decreasing stabiliser content. Other authors have reached the same conclusion (Section 2.1.2.). A similar interpretation would apply here. In Section 4.1.3.1., it is shown that cycling introduces Mg gradually into the SA aggregates: stabiliser concentrations increase with cycling, and should drop onset temperatures for transformation as well as the amount of material transformed. Correspondingly, Mg mobility in LP and HP aggregates, resulting in minor losses of stabiliser, would explain the small increase in transformation volumes implied by m-t strain increases.

Finally, in the SA refractory, the m-t strain on first cycle is almost double that found for the other two refractories, consistent with the larger proportion of monoclinic available for transformation in the SA sample (>90% versus ±50% monoclinic fraction for LP/HP - cf. XRD results in Section 4.1.6.1.).

Table 11 : Dilatometry data for the SA refractory. CTE's have been calculated on those segments of the dilatometry curves yielding >99% fit to a linear regression.

	heat 1	cool 1	heat 2	cool 2	heat 3	cool 3	heat 4
Section of curve used to calculate low temperature CTE (°C)	100-800	100-500	100-900	100-300	600-900	100-400	500-750
Low temperature CTE ($10^{-6}.K^{-1}$)	6.76	6.40	7.41	3.06	6.57	2.94	5.31
Section of curve used to calculate high temperature CTE (°C)	1250-1500	1000-1700	1250-1450	1000-1700	1250-1550	1000-1700	1200-1500
High temperature CTE ($10^{-6}.K^{-1}$)	5.26	5.08	6.97	4.94	5.03	4.94	4.78
Midpoint of m-t transformation (°C) - inflection method	1075	-	1070	-	1030	-	1000
Midpoint of t-m transformation (°C) - inflection method	-	880	-	810	-	nd	-
Onset of m-t transformation (°C) - max temp method	1054	-	998	-	966		974
Onset of t-m transformation (°C) - min temp method	-	1032	-	821	-	nd	-
Onset of m-t transformation (°C) - tangent method	±1050	-	±1050	-	±1000	-	±950
Onset of t-m transformation (°C) - tangent method	-	±900	-	±800	-	nd	-
Linear m-t strain (dL/L_o) on heating (%)	0.5	-	0.4	-	0.09		0.02

nd - not determined

5.1.2. Stiffness

Each of the three refractories was cycled for ±70 hours on the impulse excitation unit described in Section 3.3.2., representing eight service cycles between room temperature and 1750 °C. Table 12 summarises the Young modulus values obtained for the as-fired refractory before cycling and at the end of each service cycle. For all three materials, the first service cycle produces a marked increase in stiffness due to sintering at temperatures above the original firing temperature. As might be expected from the higher surface energy of the smaller aggregates, the SA refractory exhibits the greatest degree of sintering, leading to an increase in stiffness of 67%. HP and LP stiffen by 24% and 17% respectively, in their first cycle. Subsequent cycles produce little change in the Young modulus of the larger-aggregate samples. The SA refractory, however, deteriorates systematically and significantly in subsequent cycles, producing a value 43% lower than its maximum stiffness after 8 cycles.

Table 12 : Summary of stiffness data, at the end of each of eight thermal cycles.

Cycle	LP (GPa)	HP (GPa)	SA (GPa)
0	47.72	41.91	39.42
1	55.62	52.04	65.83
2	56.62	55.12	59.79
3	57.24	56.54	57.09
4	57.76	56.93	54.12
5	57.93	54.81	49.23
6	58.45	55.84	45.87
7	58.82	55.74	41.26
8	58.98	not acquired	37.11

The largest error in the conversion of resonance frequency to Young modulus is associated with the sample bar dimensions. Using an absolute errors of 0.02 mm on these and 0.001g on mass, a relative error of 0.01 GPa was calculated for the data in this table, using Equations 3 and 4 in Section 3.3.2.

Figure 57 presents stiffness data for eight thermal cycles for the **LP refractory**. A chronological sequence of material behaviour is observed as follows :

- Initially, stiffness is lost as the sample heats from room temperature to approximately 750°C and thermal expansion reduces E by approximately 1% per 100 °C. The decreasing trend in stiffness comprises a series of step-like descents, arising from the additional effect of reorientation (and relaxation) of Mg-oxygen vacancy dipoles in response to the applied impulse stress (cf. Section 3.3.2.). This interpretation is confirmed by the presence of a series of peaks in the corresponding damping curves (an example is given in Fig. 58) representing discreet dissipations in energy for each of the relaxation events over this temperature range.

- Between 750 °C and 1000 °C, stiffness increases again, due to closure of microcracks originally created during cooling after firing of the refractory. Other researchers working on high zirconia fused refractories also observe this "mid-cycle stiffness increase"[136] .

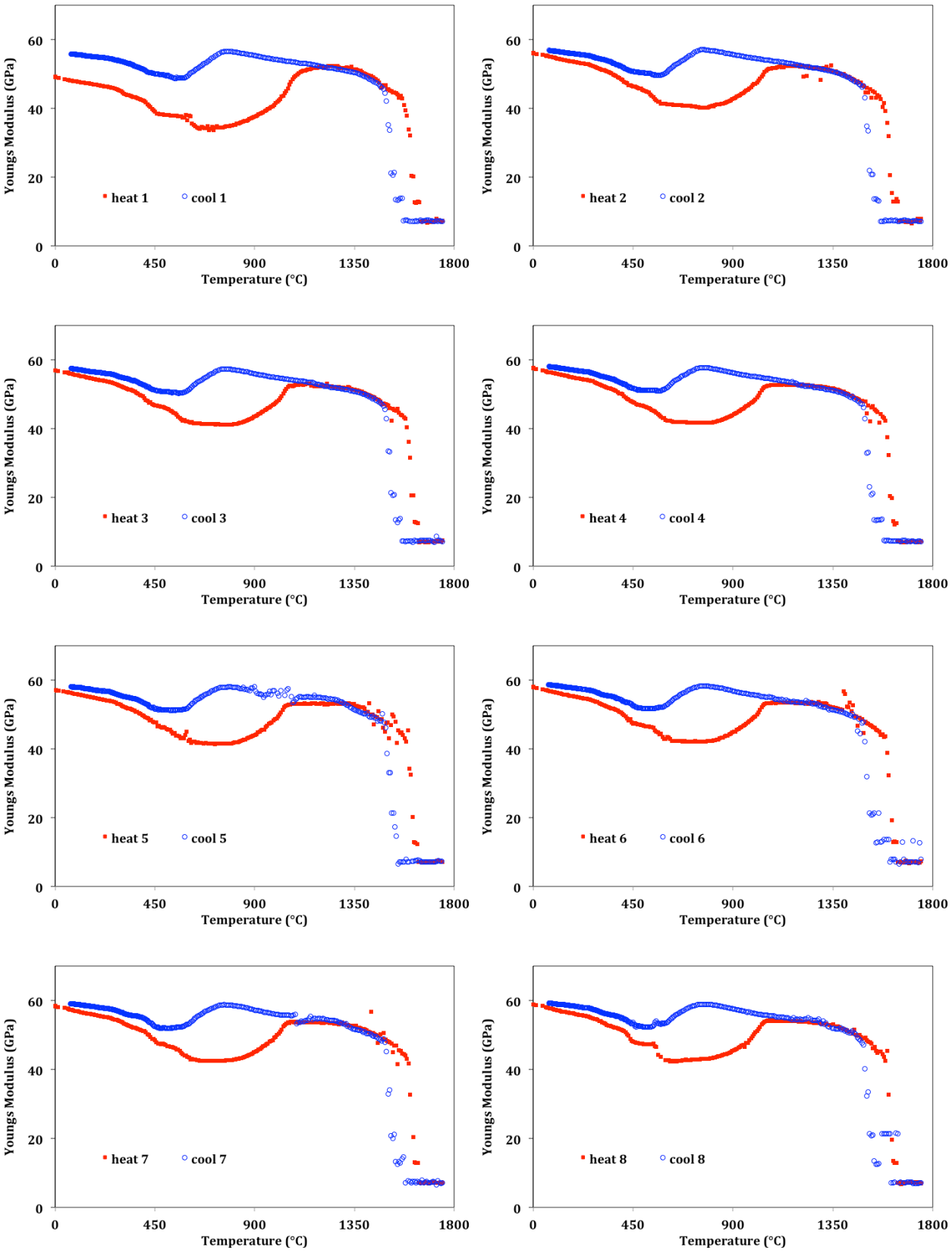

Figure 57 : Impulse excitation data for eight heating (red) and cooling (blue) cycles of the LP refractory.

- At approximately 1050 °C, there is a marked change in gradient as stiffness plateaus. This inflection point corresponds well with the 1040 °C onset temperature reported above for the m-t transformation in LP. The leveling off in stiffness is therefore attributed to the volume contraction of the transformation event.

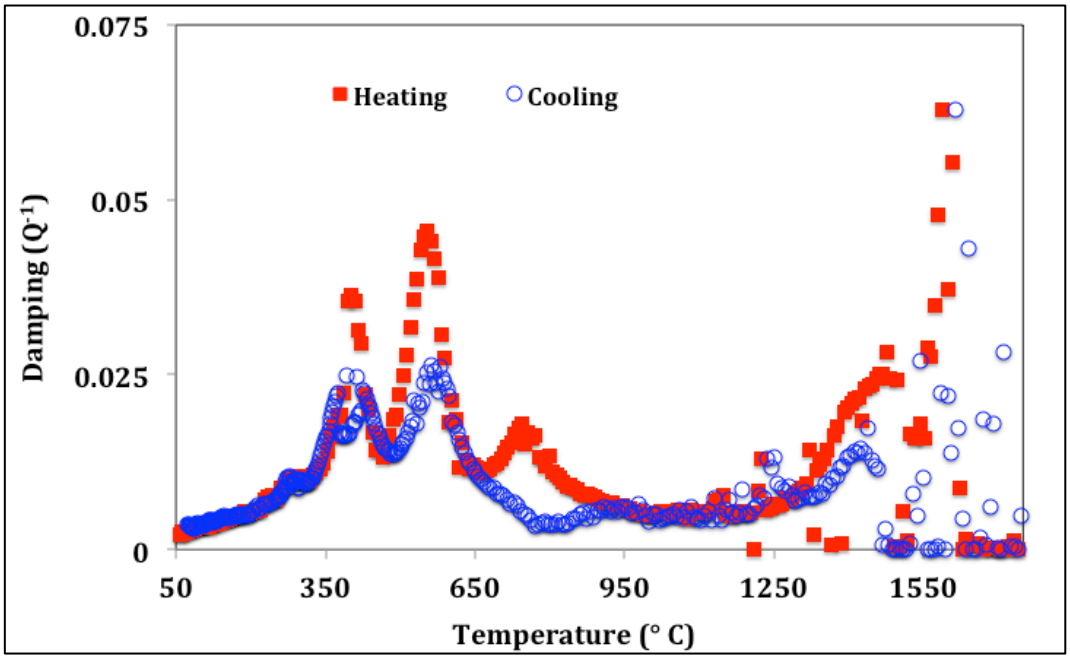

Figure 58 : Damping (energy dissipation) curves for the third thermal cycle on the LP refractory, during impulse excitation testing.

- From approximately 1560 °C, damping of the resonance vibration increases exponentially (Fig. 58), indicating the likely presence of a liquid phase, dissipating energy during vibration. This is consistent with the fact that a small amount of clay is added as a plasticiser during the manufacture of LP, which could give rise to low melting phases. The matrix phase contains enough silica (Fig. 59) to expect some viscous response in the vibration and Young modulus values calculated at these high temperatures must be viewed with some caution as derivation of the formulae in Section 3.3.2. assumed an undamped linear elastic vibration.

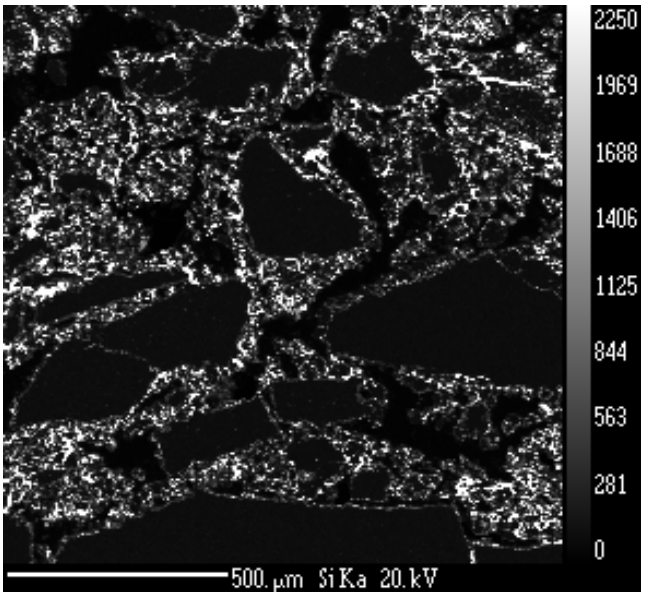

Figure 59 : SEM-EDS silicon map for the LP microstructure. Elevated Si levels in the matrix are attributed to the clay plasticiser added during green body manufacture.

- On cooling, a ±100 °C temperature lag arises in the data. This is due to the relatively high heating/cooling rates used during cycling, which give rise to quite different temperature distributions in the furnace during heating and cooling. (Heating rates were chosen to mimic real-world behaviour in which the refractory is routinely heated and cooled at rates above 10 °C/min in service.) Stiffness increases rapidly below 1580°C and returns to its previous maximum value.

- At ±750 °C there is an inflection. This temperature, allowing for some of the lag mentioned above, correlates broadly with the 850 °C at which the t-m transformation occurs, based on the dilatometry data in Section 5.1.1. Again, the inflection in the stiffness curve is attributed to the impact of the transformation: the volume expansion associated with t-m inversion gives rise to microcracks that expand on cooling, reducing stiffness.

- Above and below 750 °C, the linear trend in increasing stiffness is simply attributed to thermal contraction. As room temperatures are approached and interatomic bonds tighten, the lattice dipoles adjust to the changing stress regime, stiffening the zirconia in a trend which parallels the heating trend. Damping data suggest that the reverse adjustment of the Mg-vacancy dipoles does not always parallel relaxation behaviour

during heating as the damping peaks do not necessarily match in number or position (Fig. 58).

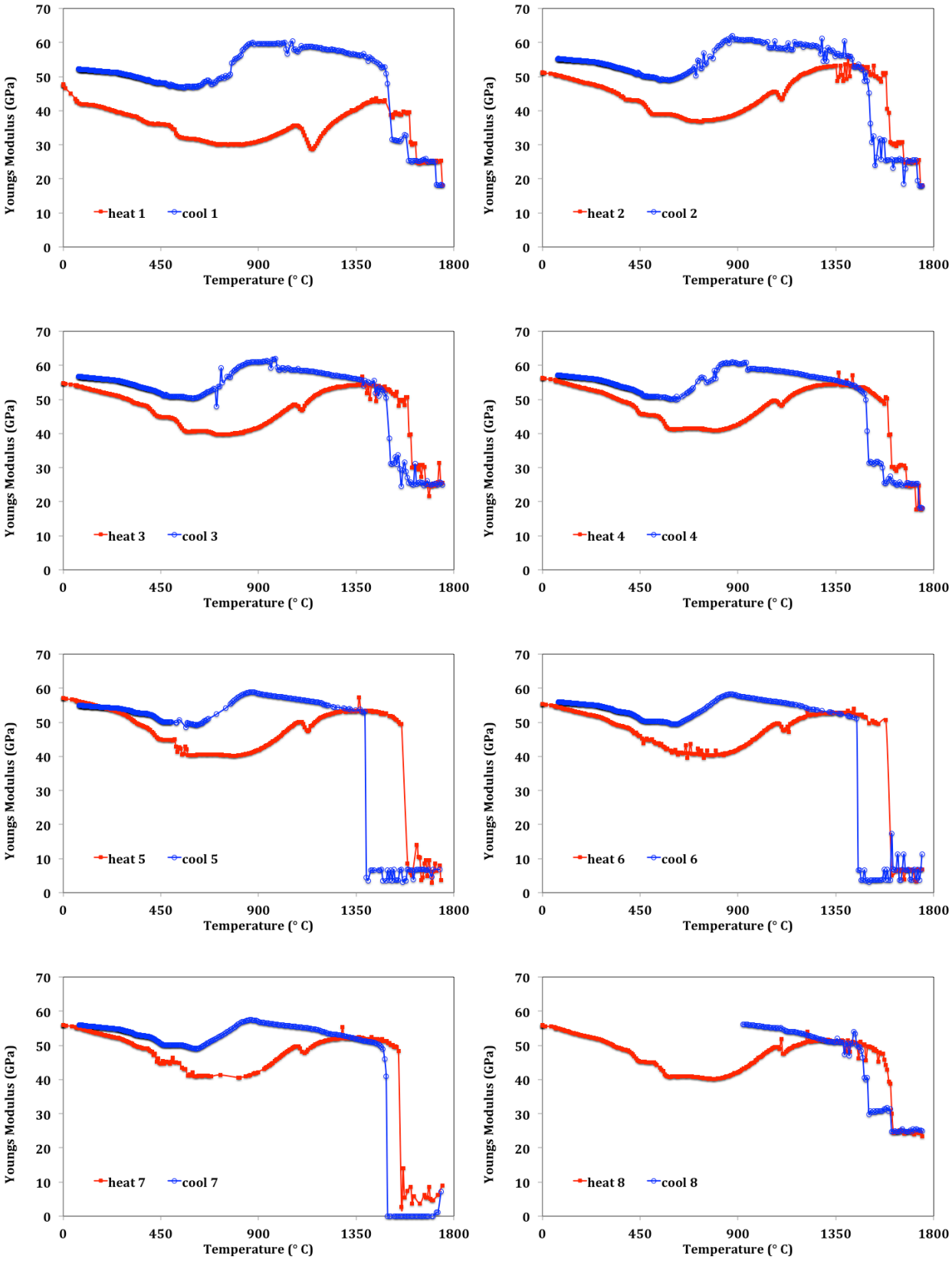

Figure 60 : Impulse excitation data for eight heating (red) and cooling (blue) cycles of the HP refractory.

Figure 60 contains the eight thermal cycles for the **HP refractory**. The heating and cooling curves observed for HP are similar to those just discussed for LP, with a notable exception: between 1050 °C and 1150 °C, a distinct reduction in stiffness (±3-5 GPa) coincides exactly with the m-t transformation temperature zone. In this instance, transformation strain appears to have a greater immediate impact on the bulk material than for the LP refractory. Contraction during the m-t event is interpreted to fracture some elements within the microstructure, leading to a temporary loss of bulk rigidity. Although most distinct in thermal cycle 1, the feature remains for all eight thermal cycles recorded.

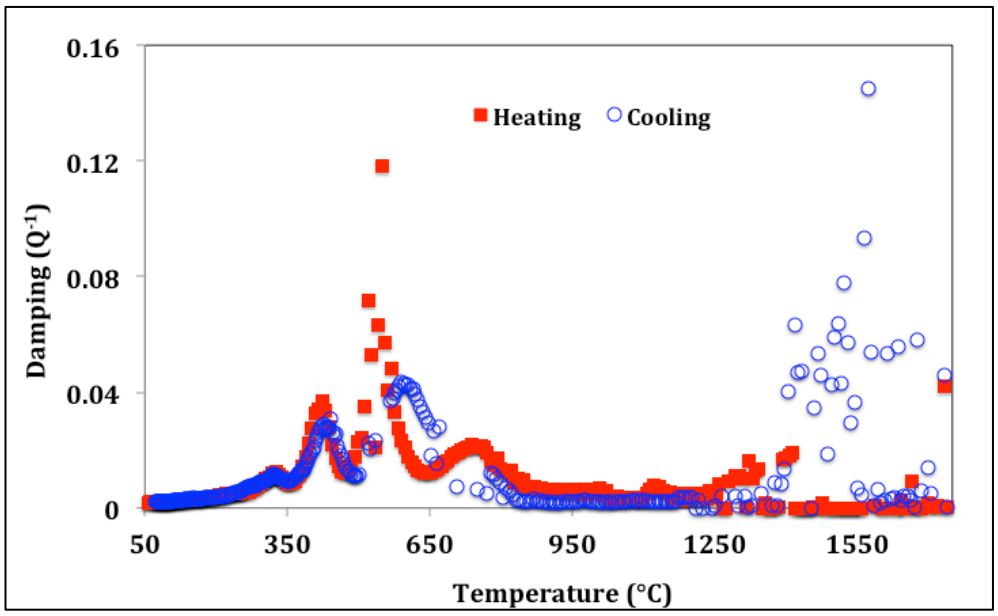

Figure 61 : Damping (energy dissipation) curves for the fifth thermal cycle on the HP refractory, during impulse excitation testing.

Recent acoustic emission and ultrasonic pulse work on high zirconia fused cast refractories produced the same distinct stiffness drops at m-t transformation temperatures[136] [26] [137]. Using some rare Young modulus data for single monoclinic crystals and Voigt, Reuss and Hill extrapolations (to convert single crystal elasticity to polycrystalline equivalents) for stiffness for tetragonal zirconia, Fogaing et al.[136] suggest a two tier contribution to stiffness change during the polymorphic transformation: first, they calculate an approximately 30 GPa drop in the stiffness (six times larger than the reduction observed in the data presented here) which should occur simply due to the difference in Young modulus values for the pure monoclinic and tetragonal phases and second, stiffness should drop further as a result of the strain and damage induced by the transformation.

With respect to the latter, it has also been shown that multiple monoclinic crystal variants form during first cooling after firing and these adjacent, but variably oriented, domains give rise to microcracks due to their anisotropic strain differences during transformation[26] [137]. The microcracks so caused manifest as cross-hatch features similar to the 109°-oriented microcracking noted for the refractories in this study (Fig. 24D in Section 4.1.2).

Damping in HP increases exponentially from 1350 °C (Fig. 61), consistent with the leveling off of stiffness data at this temperature and is once more attributed to the potential presence of a viscous liquid at high temperature.

Figure 62 contains eight recorded cycles for the **SA refractory**. The stiffness behaviour in this material is different from that of the larger aggregate refractories in several ways. First, the drop in stiffness during m-t transformation while the material heats, is much larger (12-15 GPa vs 3-5 GPa for HP) and the sample does not recover room temperature stiffness values as it climbs to maximum temperature. This aligns with the dilatometry results, in which a larger m-t strain is noted, due to the higher levels of monoclinic phase in the SA aggregates (±90%), relative to LP and HP aggregates (±50%).

Second, the elevation in stiffness during the t-m transformation, on cooling, appears to be a distinct event, rather than a continuous linear trend as observed for the other samples. In fact, from the second cycle onwards, resonance oscillates between two frequencies, quite close together, between temperatures of ±915 °C and ±1215 °C, one defining a continuous, linear cooling path as for HP and LP, and one delineating the elevated stiffness interval presented here. The last plot in Fig. 62 (after 8 cycles) gives some idea of the situation emerging when both frequencies are plotted. It is possible that the high transformation strains have destroyed aggregate-matrix interfaces enough to allow free movement of the aggregates in their surrounding matrix. The two frequencies observed may then be a consequence of the aggregates reaching a locked state (giving rise to a high stiffness) or not (giving a lower stiffness) until they have all expanded and been locked into the microstructure again.

Third, a small 'peak' occurs in the heating data between 1125 °C and 1175 °C for all seven cycles after the initial heat. The origin of this small recovery, post m-t event, followed by another stiffness drop, is at present inexplicable.

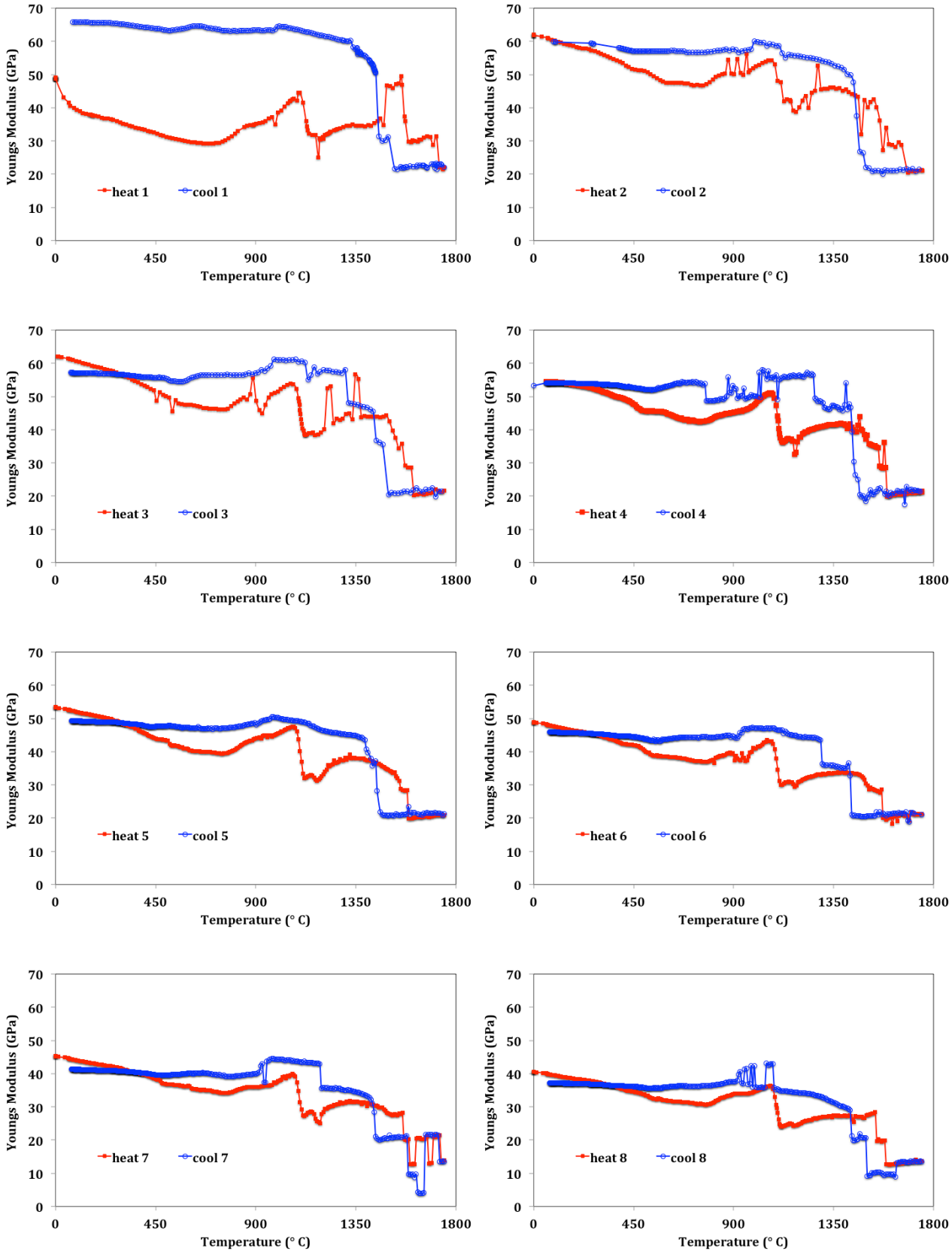

Figure 62 : Impulse excitation data for eight heating (red) and cooling (blue) cycles of the SA refractory.

5.1.3. Strength

Force-displacement curves for the LP, HP and SA refractories - before and after eight thermal cycles - are presented in Figures 63, 64 and 65 respectively. Prior to cycling, the LP and HP refractories yield higher break force values for those test bars oriented with their concave surface facing the crosshead. After cycling, all three refractories display this behaviour. The change in the SA refractory response to the bend conditions once again highlights the more marked evolution of this refractory with cycling.

All three refractories yield initial force-displacement trends which are linear. In Figs. 63a and 10b, the 'climbing force' curves for LP exhibit random sawtooth features or minor inflections that are a typical result of the hardness of ceramics which, as a consequence, tend to damage or chip at the loading points. They do not occur in the data for the HP and SA refractories, suggesting that the coarser and less consolidated nature of the LP microstructure directly affects test conditions.

At point of fracture and afterwards, all three refractories show rounded force maxima and inclined (rather than just vertical) breakage slopes (Figs. 63b, 64b and 65b), indicating that totally brittle failure did not occur. The breakage slopes all display a sudden drop in force, implying an initial burst of crack growth, but deflection of the curve as crack growth becomes stable[138]. These refractories can thus be said to be more prone to semistable fracture. The results can be compared to standard curves presented by Nakayama[58] in 1965 (Fig. 66) to demonstrate the impact of crack stability on force-time response. The breakage slopes of the LP refractory are the most notably inclined with the curves from the convex-side-up test bars almost symmetrical around the curve apex (Fig. 63b). Cracking is therefore almost fully stable for this material after cycling.

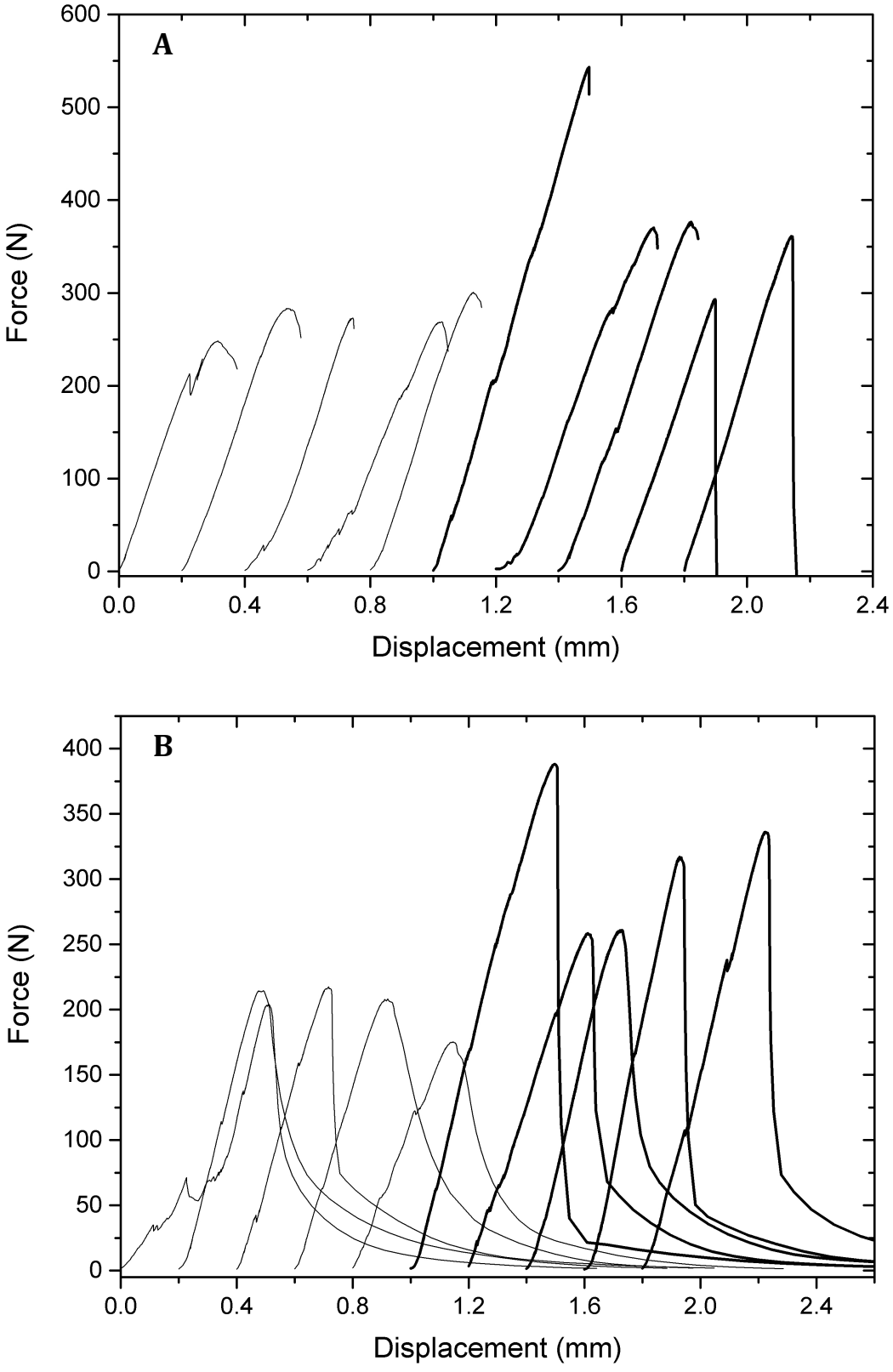

Figure 63 : MOR results for the LP refractory, before (A) and after (B) eight thermal cycles. Thin black lines represent convex-up bars and thicker black lines, concave-up bars. Results in A were terminated after 5% drop in force, post maximum force except for dotted line tests which were carried out with ball bearing contact between crosshead and sample.

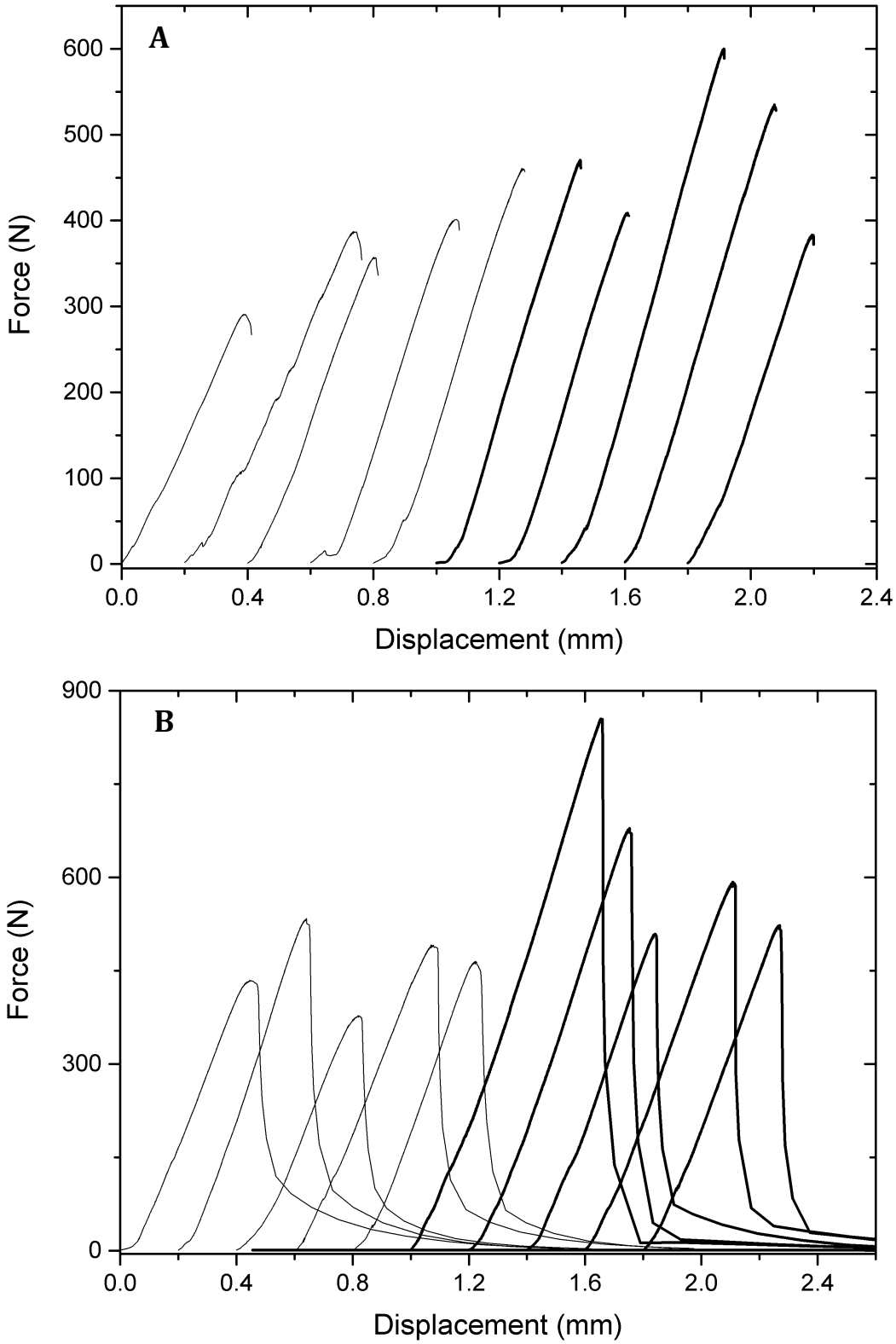

Figure 64 : MOR test results for the HP refractory, before (A) and after (B) eight thermal cycles. Thin black lines represent convex-up bars and thicker black lines, concave-up bars. Results in A were terminated after 5% drop in force, post maximum force.

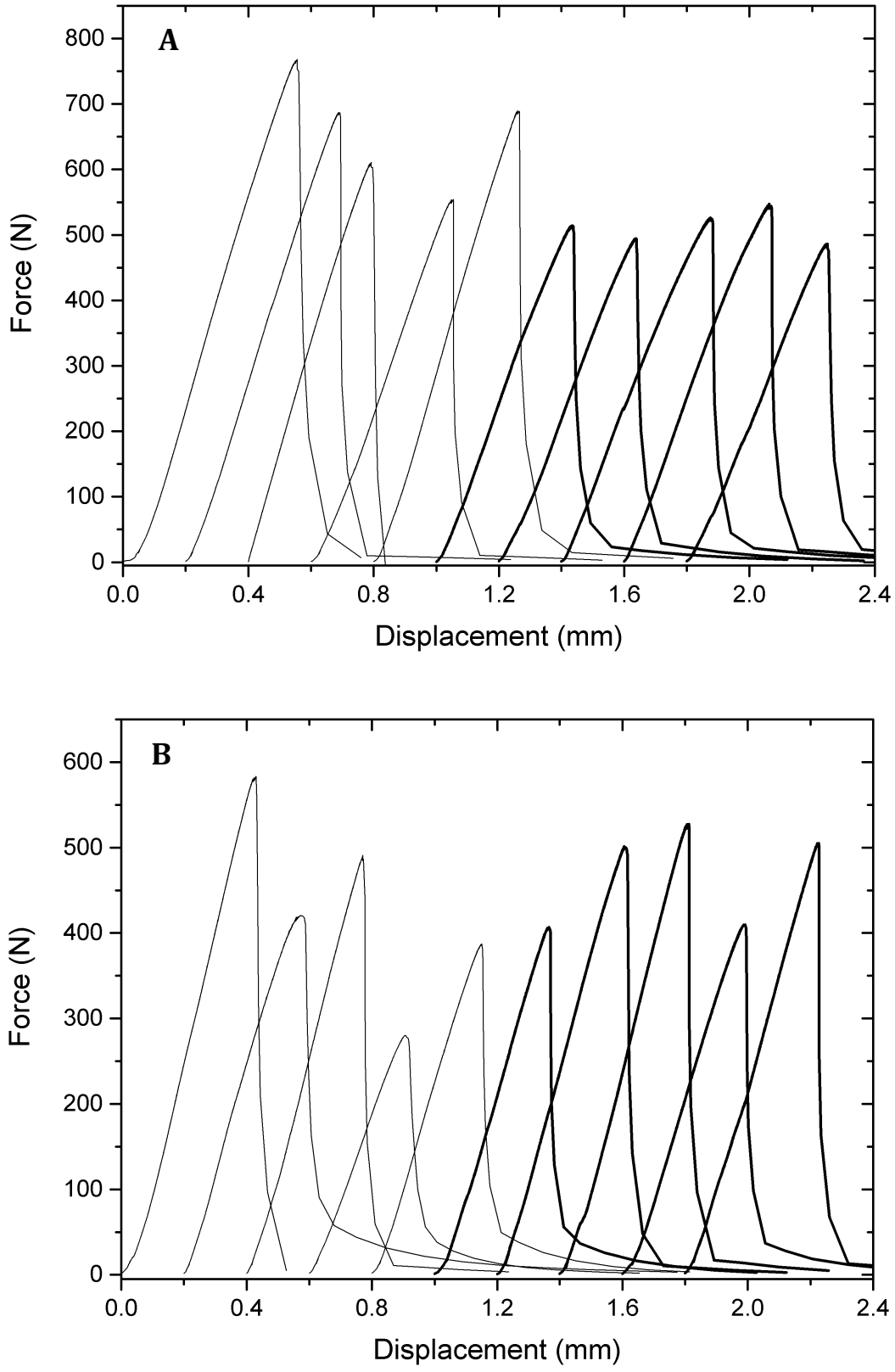

Figure 65 : MOR results for the SA refractory, before (A) and after (B) eight thermal cycles. Thin black lines represent convex-up bars and thicker black lines, concave-up bars.

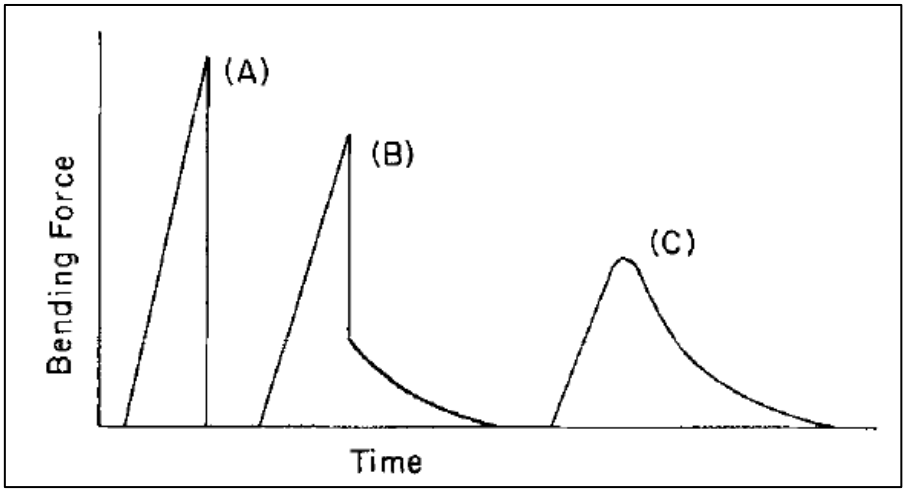

Figure 66 : Load-time curves representing catastrophic (A), semistable (B) and stable (C) fracture of a brittle heterogeneous material. Reproduced with permission[58].

Average strength data were calculated for a sample of ten bars per refractory, before and after thermal cycling. The data are plotted in Fig. 67 with a sample-specific standard deviation in order to compare performance. After cycling, average strength drops by 24% from 17 MPa to 13 MPa for the LP refractory, and by 29% for the SA material (24 MPa to 17 MPa). The HP refractory's average performance improves from 20 MPa to 25 MPa (25%) with cycling. The overall range of data is consistent with the low strengths (usually less than 30 MPa[139]) expected of refractories.

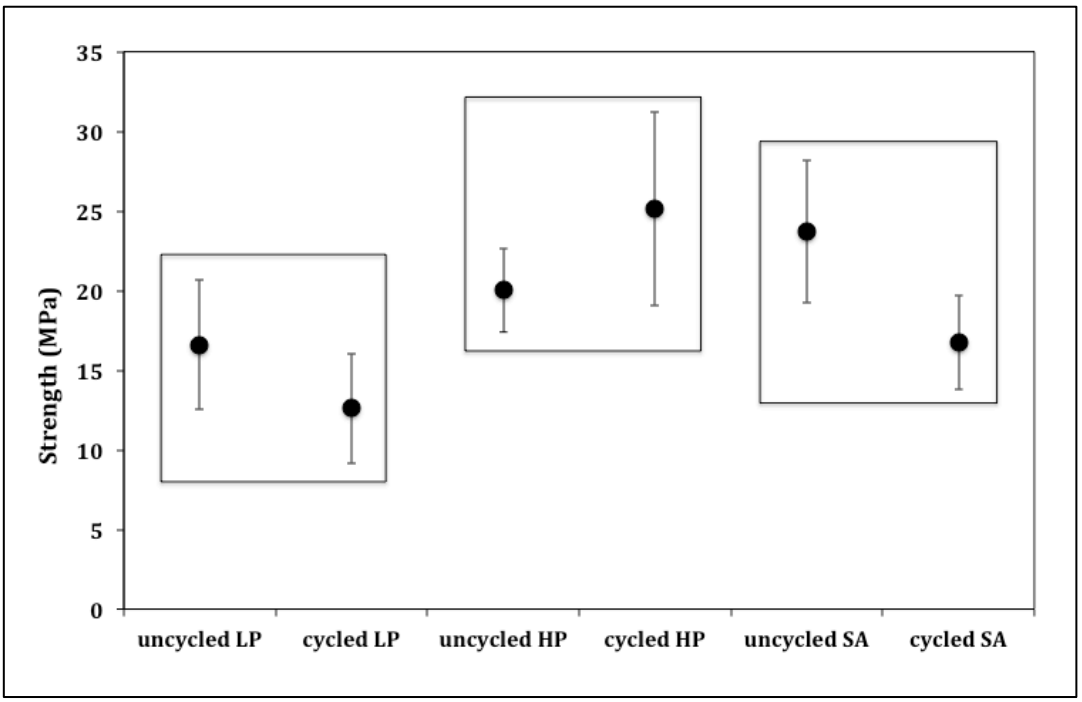

Figure 67 : Strength results for each refractory, pre- and post- eight thermal cycles. Each data point represents an average for ten test results. Error bars are one standard deviation using n-1 (i.e. 9).

5.1.4. Fracture toughness

The force-displacement curves for single edge notched bars (SENB) of LP, HP and SA are presented in Figures 68, 69 and 70 respectively. Once again, the SA refractory displays reverse behaviour, relative to LP and HP, in terms of bar orientation's impact on breaking force. Contrary to the results for the unnotched bars, the SENB used for the fracture toughness bend tests yield higher breaking forces when placed convex side up to the crosshead. This situation does not reverse on cycling. For the SA refractory, however, breaking forces are similar irrespective of orientation, prior to cycling, and concave-up orientations record larger breaking forces after cycling.

Linear elastic behaviour pertains to all the samples, prior to fracture.. Breakage slopes are rounded from the point of fracture and inclined, as before, confirming semistable-stable fracture. Because notching reduces the load at which fracture occurs and thus less energy has been stored in the sample when it breaks, fracture for the HP and SA refractories appears more stable (lower inclination angle on the breakage slopes) than for the un-notched bar tests.

Average fracture toughness data, calculated for a sample of ten bars per refractory, before and after thermal cycling, are plotted in Fig. 71, with sample-specific standard deviations. The toughness values fall within the range known for refractories[139]: 0.2-1.5 MPa.m$^{1/2}$. After cycling, average toughness drops by 14% for the LP refractory (from 1.3 to 1.1 MPa.m$^{1/2}$) and 20% for the SA refractory (from 1.5 to 1.1 MPa.m$^{1/2}$). Average toughness improves by 24% with cycling of the HP refractory (from 1.4 to 1.6 MPa.m$^{1/2}$). These results fall within the error margins of the test but clearly indicate that the HP refractory fares better in terms of toughness evolution, relative to the SA refractory. Work of fracture (WOF) data are summarised in Table 13 and are consistent with the high end of WOF value ranges quoted for refractories in general[139] : ±10-150 J/m^2.

Table 13 : Average work-of-fracture values, calculated from the area under SENB fracture curves and fracture surface area (x2) of SENB bars. Standard deviation is for n=9.

Sample	Average work-of-fracture (J/m^2)
uncycled LP	204 ±55
cycled LP	157 ±33
uncycled HP	192 ±33
cycled HP	241 ±58
uncycled SA	203 ±16
cycled SA	123 ±16

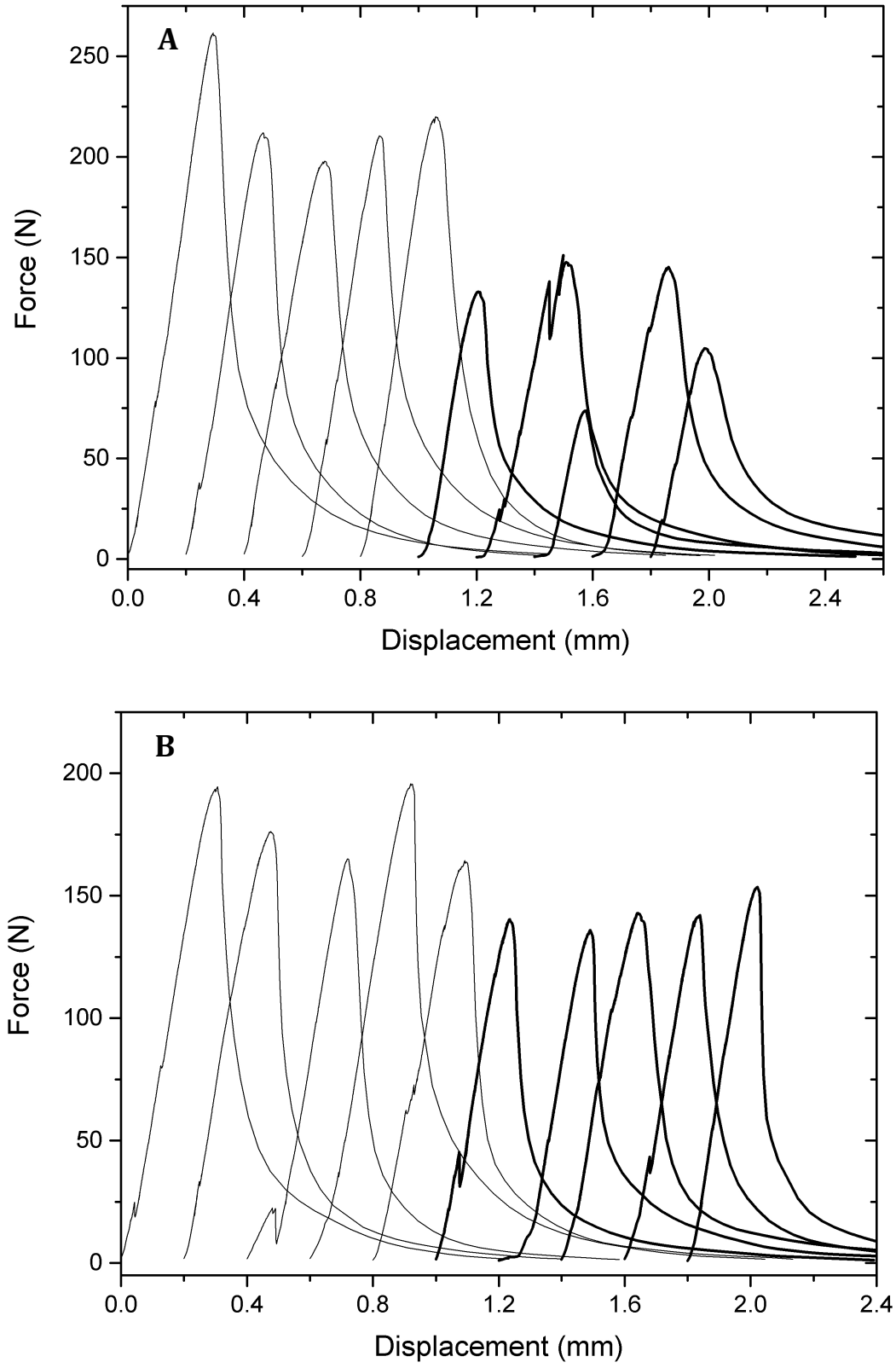

Figure 68 : SENB test results for the LP refractory, before (A) and after (B) eight thermal cycles. Thin black lines represent convex-up bars and thicker black lines, concave-up bars.

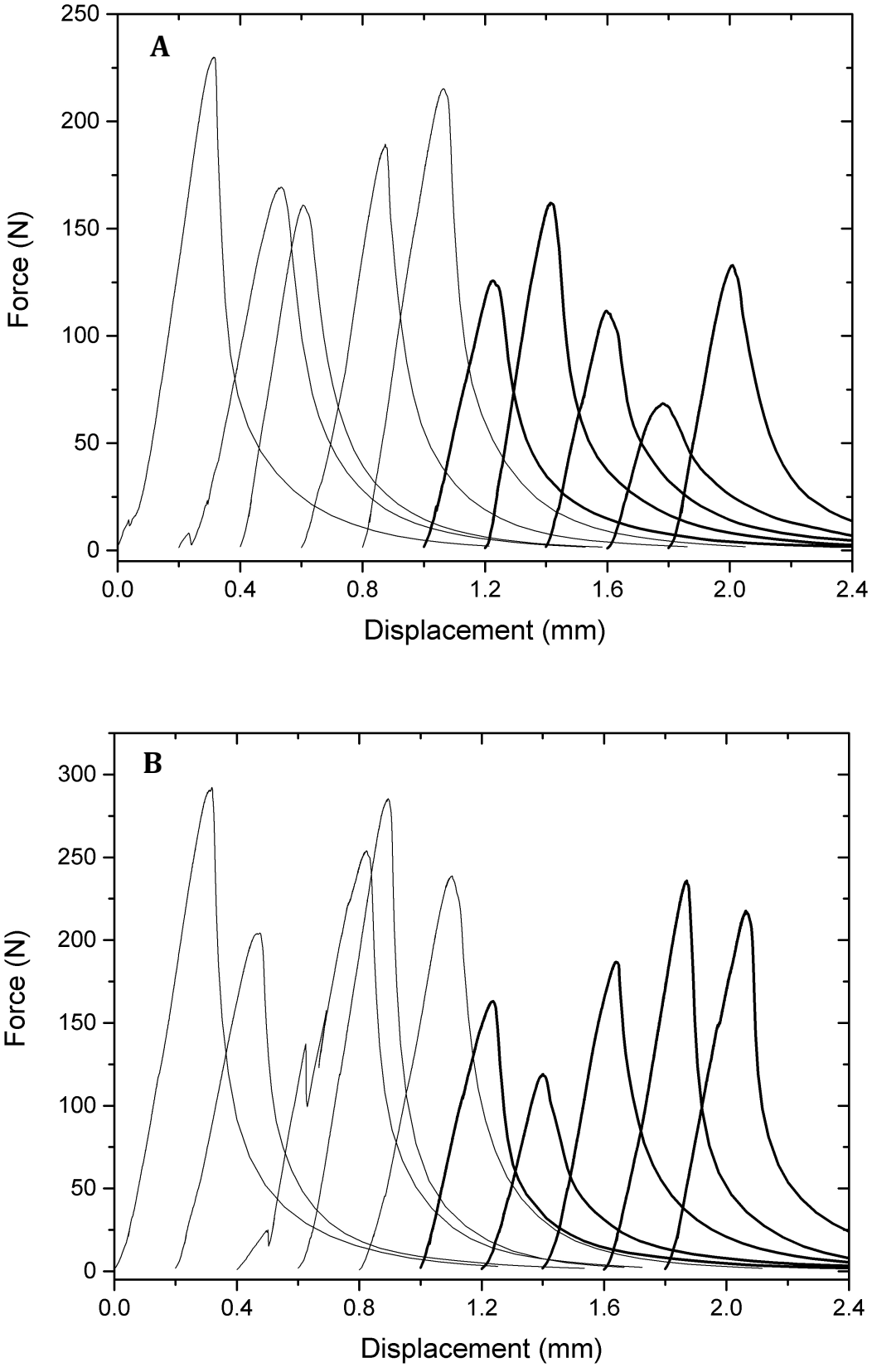

Figure 69 : SENB test results for the HP refractory, before (A) and after (B) eight thermal cycles. Thin black lines represent convex-up bars and thicker black lines, concave-up bars.

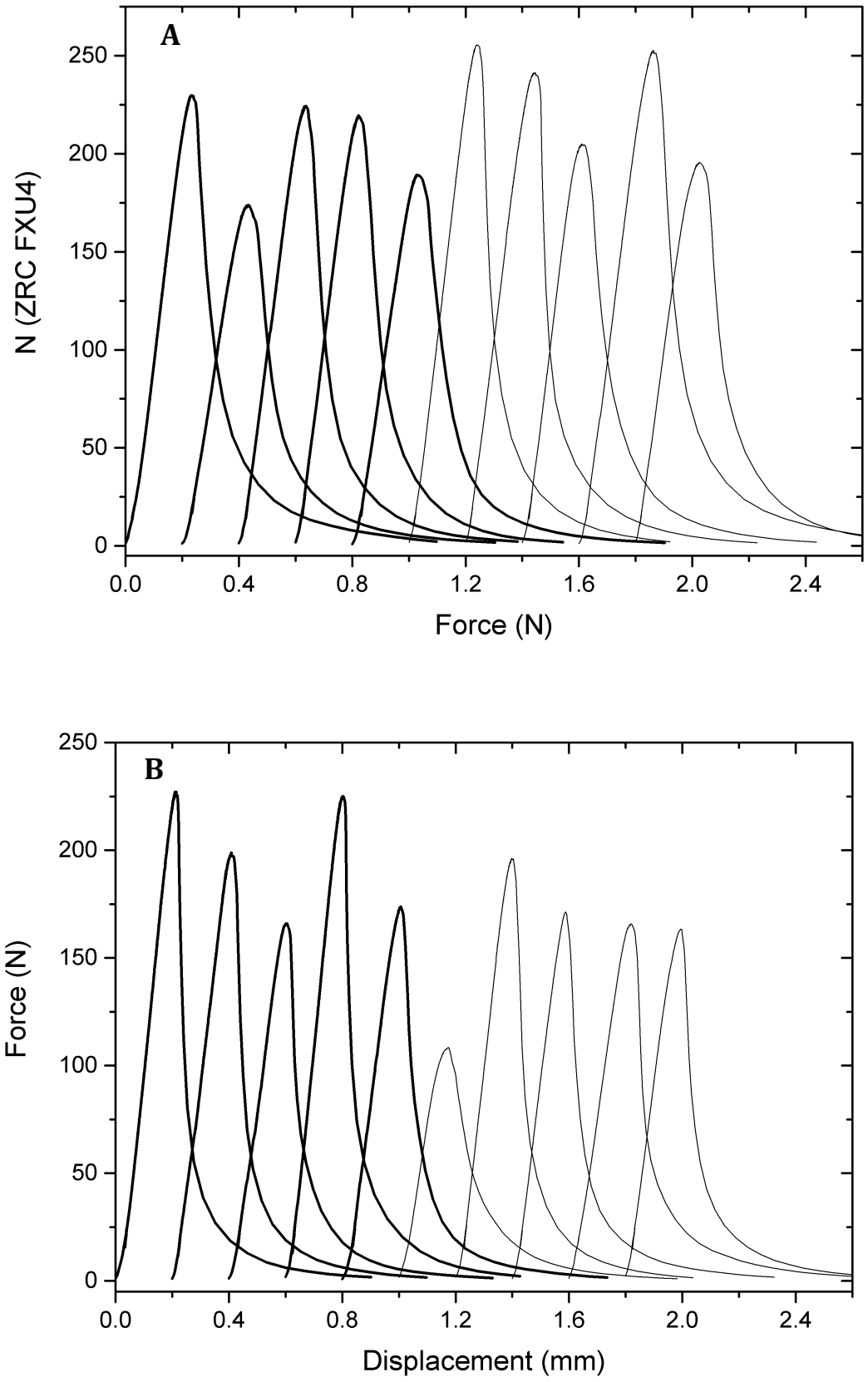

Figure 70 : SENB test results for the SA refractory, before (A) and after (B) eight thermal cycles. Thin black lines represent convex-up bars and thicker black lines, concave-up bars

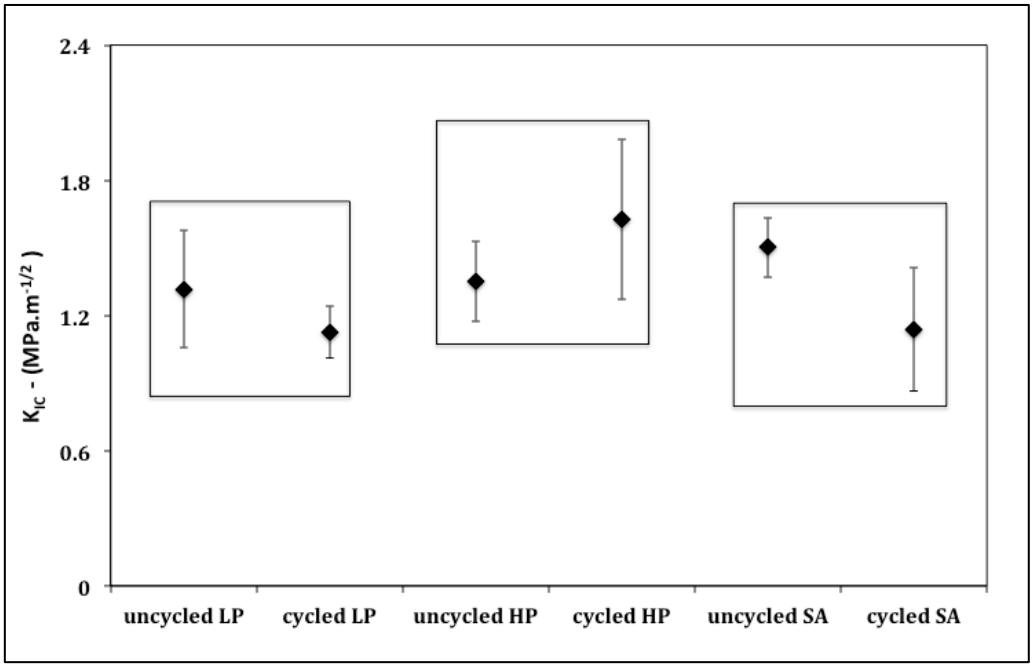

Figure 71 : Fracture toughness results for each refractory, pre- and post- eight thermal cycles. Each data point represents an average for ten test results. Error bars are one standard deviation using N-1 (i.e. 9).

5.1.5. Fracture paths and surfaces

Several dozen attempts to obtain an R-curve using double cantilever testing of notched specimens failed, always due to breakage in the cantilever sections, at the base of the notch (Fig. 72). Cracking initiated where the notch edge intersected aggregate-matrix interface and propagated as pre-existing cracks joined up with the main crack which continued to branch.

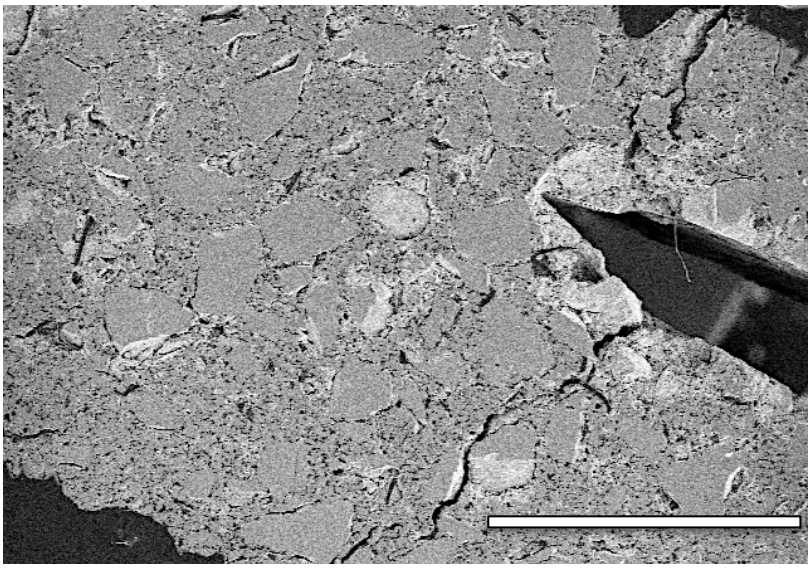

Figure 72 : Secondary electron image of the cycled HP refractory with a notch for double cantilever testing. The specimen has cracked near the base of the notch, in the cantilever regions, with cracking initiated at aggregate-matrix interfaces intersected by the notch edge. Scalebar is 2 mm.

Although this testwork did not yield quantitative data, it did provide examples of crack path tendencies. Fig. 73 is a clear and rare example of an aggregate where secondary phase development has produced openings along internal subgrain boundaries. As this aggregate lies within the crack path (Fig. 73A), it is possible that fracture surface may have developed internally, to exploit the pre-existing openings.

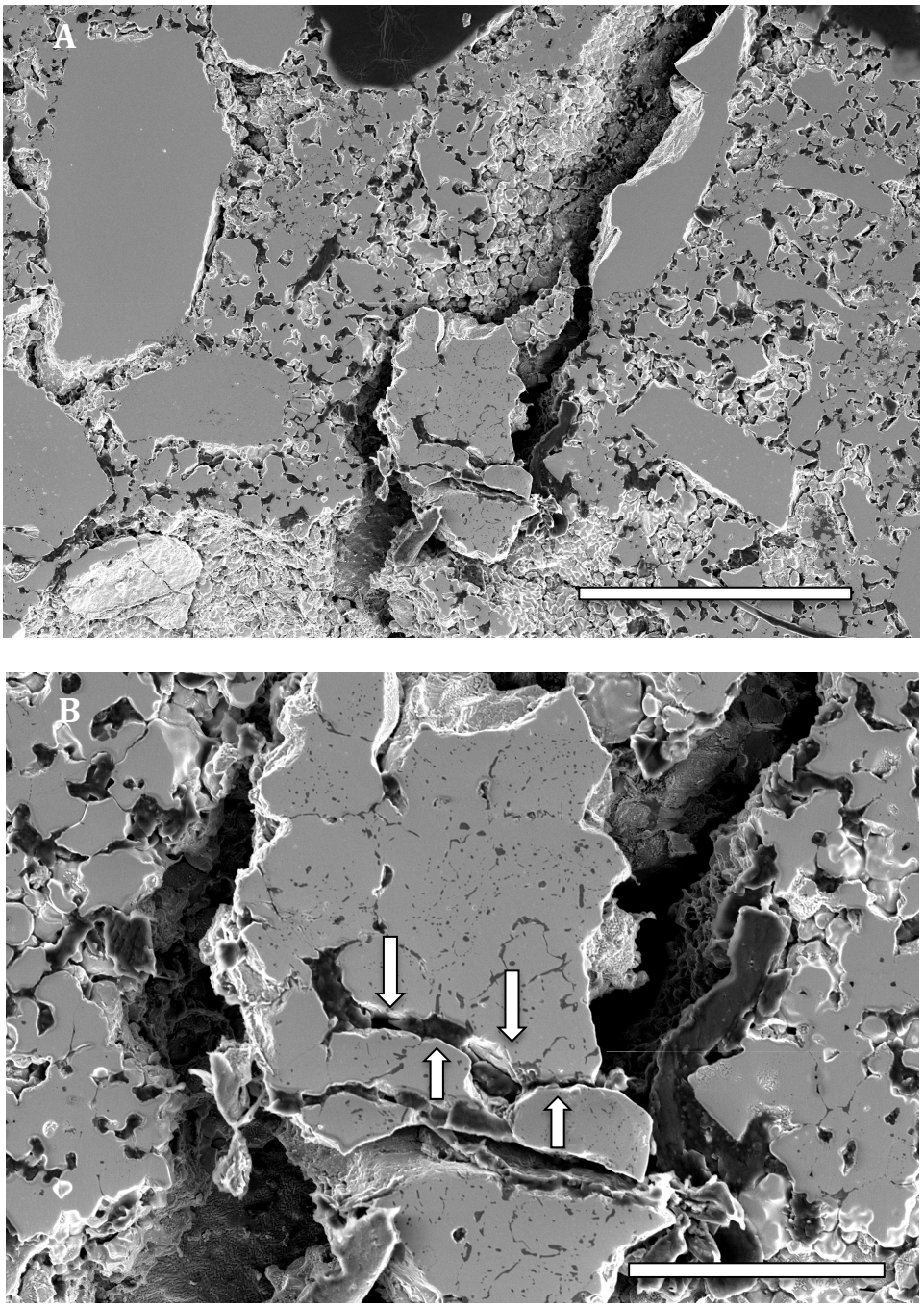

Figure 73 : Secondary electron images of a fracture path through the cycled HP refractory. An aggregate with secondary phase breakdown and openings at internal grain boundaries (arrowed region). Scalebars are 2 mm (A) and 500 µm (B).

The example in Fig. 73 is for the HP refractory but aggregate breakdown due to secondary phase development was far more prevalent in the LP refractory (Table 3, Section 4.2.1.). Fracture surfaces from the three point bend test specimens, viewed under a stereomicroscope reveal a combination of inter- and intra-granular breaks across aggregates in the LP refractory (Fig. 74). Plucked aggregates (from intergranular fracture) are mirrored by clean pits on the mirror surface (Fig. 74B). Intragranular breaks are characterised by distinct crater shapes in the negative halves (Figs. 74C) - some with trapezoid bases - and facets on the positive halves of the broken aggregates (Figs. 74D).

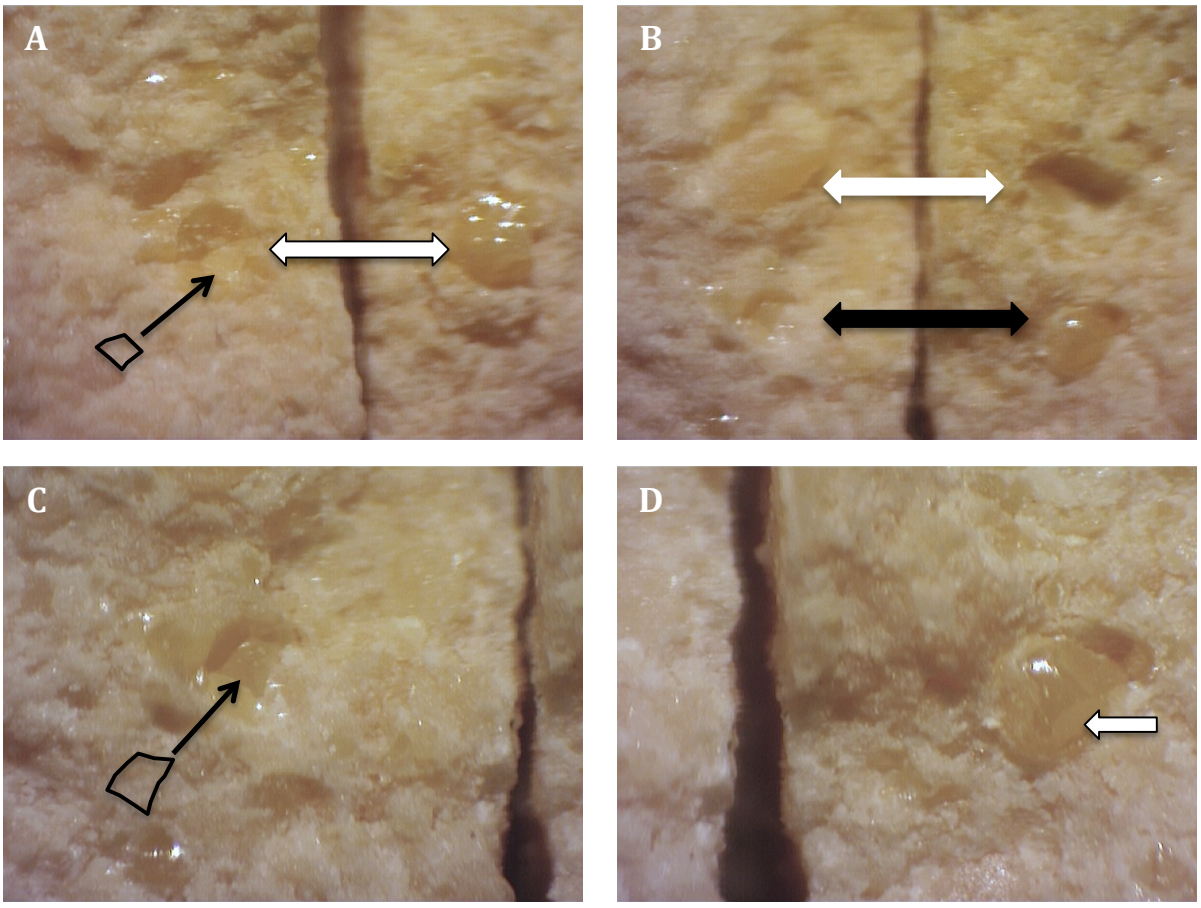

Figure 74 : Stereomicroscope images of an uncycled LP fracture surface. A and B represent two different fields of view. Aggregate highlighted in A has fractured internally and the negative half has a characteristic trapezoid base. Top aggregate in B (white arrow) has pulled out completely; lower aggregate in B (black arrow) has fractured internally. The latter is shown at higher magnification in C and D, with the trapezoid base of the negative half again demonstrated, as well as the faceted edges on the positive half (white arrow in D). Aggregates are approximately 500 µm in diameter.

SEM images of the same types of feature provide a magnified view of the positive and negative relief of fractured LP aggregates in Fig. 75. A qualitative comparison of the LP and HP fracture

surfaces, post three point bend testing, indicated a high prevalence of intragranular fracture in LP with minimal indication of intragranular fracture on the HP surfaces. Small aggregate sizes in the SA refractory made aggregate surface evaluation difficult but pull-out pits were observed on the fracture surfaces.

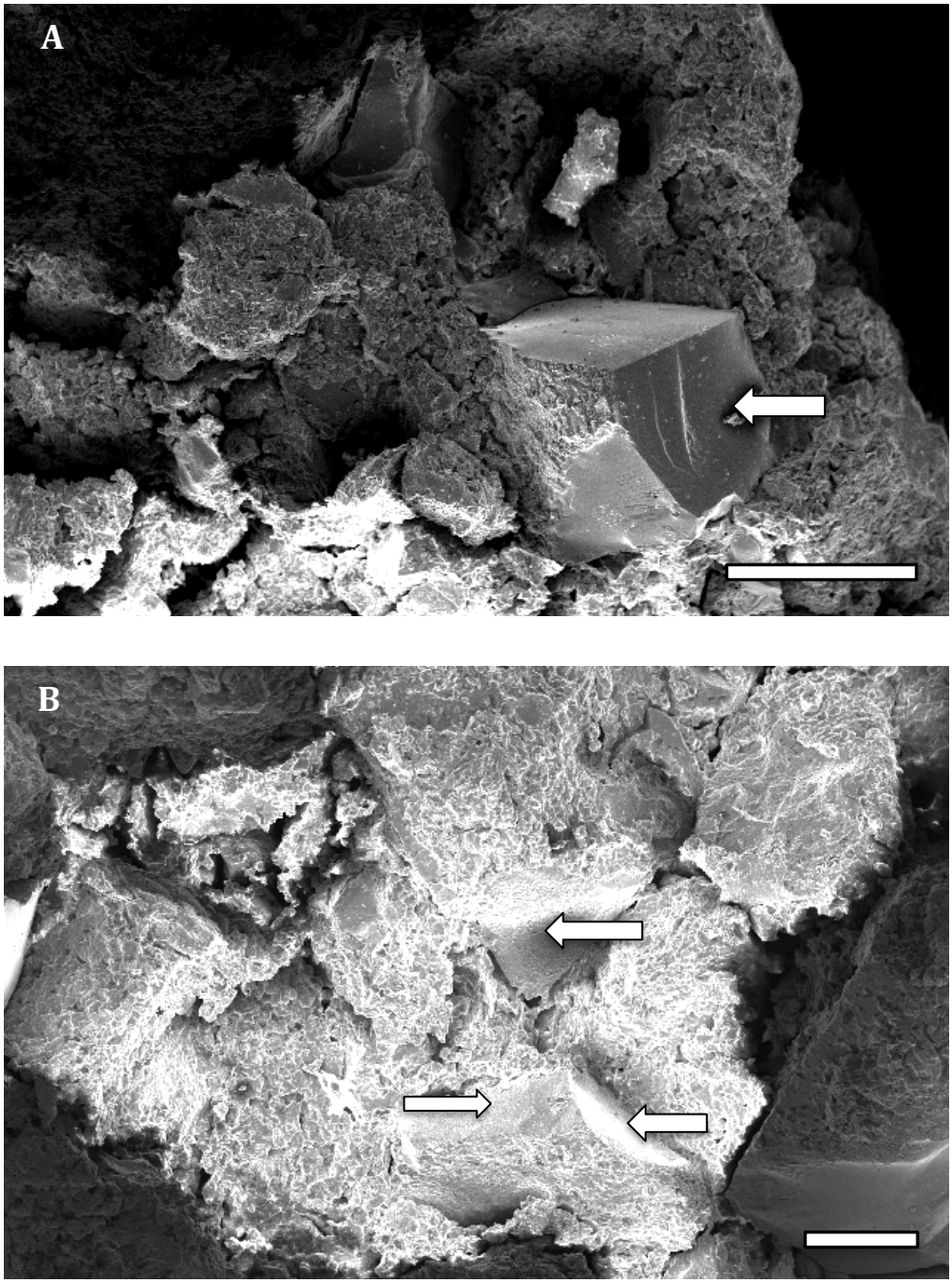

Figure 75 : Secondary electron images of fracture surfaces on the LP refractory before (A) and after (B) eight thermal cycles. The arrow in A highlights the strongly faceted sides of a fractured aggregate. Arrows in B indicate a crater region remaining after aggregate break up. Scalebars are 500 µm and 200 µm respectively.

5.2. Discussion

Table 14 contains a summary of the bulk thermomechanical properties measured and calculated for the three refractories LP, HP and SA. In the sections below, changes in these properties, with thermal cycling, are discussed.

Table 14 : Summary of bulk mechanical properties pre- and post-cycling for the LP, HP and SA refractories. Aggregate dimension data are included for comparison.

Property	as-fired LP	cycled LP	as-fired HP	cycled HP	as-fired SA	cycled SA
CTE ($10^{-6}K^{-1}$)	5(LT) - 12 (HT)	nd	5(LT) - 14 (HT)	nd	7 (LT) - 3 (HT)	nd
E (GPa)	48; 56 (after 1st run)	59 ±0.01	42; 52 (after 1st run)	56 ±0.01	39; 66 (after 1st run)	37
σ (MPa)	17 ±4	13 ±4	20 ±3	25 ±6	24 ±5	17 ±3
K_{IC} ($MPa.m^{-1/2}$)	1.3 ±0.3	1.1 ±0.1	1.4 ±0.2	1.6 ±0.4	1.5 ±0.1	1.1 ±0.3
$G_{ICo} = K_{IC}^2.(1-\nu)/E$ ($J.m^{-2}$)	21.6	15.0	24.6	33.1	23.9	24.5
γ_{wof} ($J.m^{-2}$)	204 ±55	157 ±33	192 ±33	241 ±58	203 ±16	123 ±16
$R = 2\gamma_{wof}$ ($J.m^{-2}$)	408	314	384	482	406	246
d_{50} (mm)	0.163	nd	0.145	nd	0.071	nd
d_{90} (mm)	0.312	nd	0.298	nd	0.126	nd
Diameter of single largest measured aggregate (mm)	0.965	nd	0.472	nd	0.216	nd
Critical flaw size (mm) = $(K_{IC}/1.12\ \sigma)^2 / \pi$	1.6	2.0	1.2	1.1	1.0	1.2
Characteristic length ($J.m^{-2}$) = $(2\gamma_{wof}.E)/\sigma^2(1-\nu)$	1.3	1.4	0.99	1.1	1.1	0.53

nd : not determined; ± indicates standard deviation; LT - low temperature; HT - high temperature; Poisson value of 0.3 assumed for all calculations.

5.2.1. Evolution of stiffness

The Young modulus for these fused zirconia refractories - at around 50 GPa - is approximately a quarter of that determined for dense polycrystalline zirconia ceramics[6], reflecting the porous and relatively poorly connected microstructures of the former relative to the latter. Using the stiffness as a proxy for connectedness, the data in Table 14 suggest that early cycling does not compromise the degree to which microstructure is connected in the LP and HP materials. These two refractories have in common their larger aggregate size distributions and the fact that the aggregates and matrix are Mg-stabilised. SA aggregates are smaller and unstabilised and this refractory's thermal expansion and stiffness responses are notably different from those of LP and HP.

The SA refractory data for dilatometry and impulse excitation both highlight the large impact of the m-t transformation on *bulk* material response to heating. The SA refractory *matrix* particles are stabilised though, and their response to the m-t event should be limited. This suggests that the mismatch between stabilised matrix response and the unstabilised aggregates' response to transformation may be the primary cause for material deterioration in terms of SA stiffness: expansion / contraction differences at the interface between aggregate and matrix result in debonding and general loss of connectedness in the microstructure (Fig. 76).

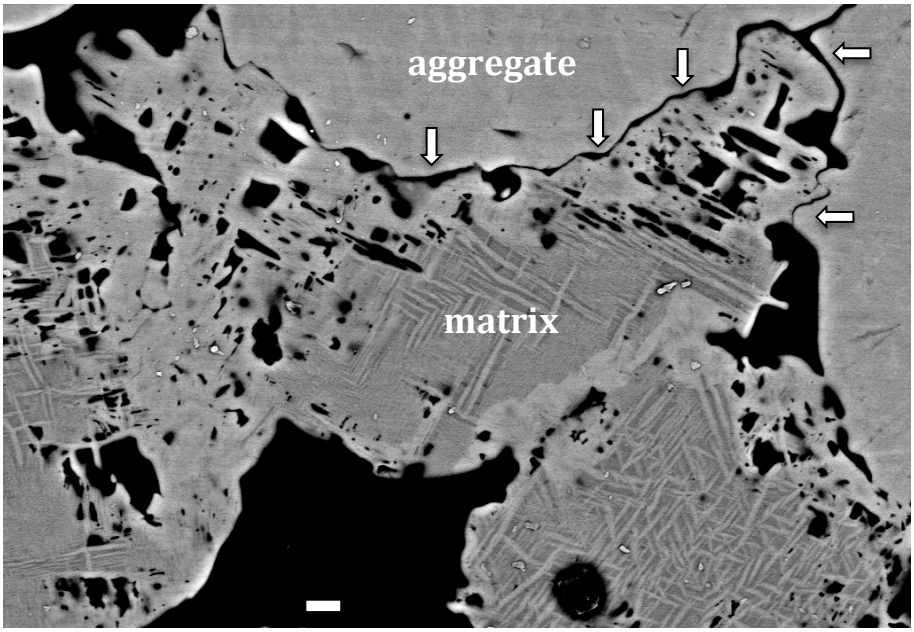

Figure 76 : Secondary electron image of SA refractory, post cycling. Arrows highlight interfaces that appear to be fresh breaks between aggregate and matrix. Scalebar is 2 µm.

5.2.2. Evolution of strength and toughness

Table 14 shows that LP and SA lose strength and toughness with cycling, while HP's mechanical performance improves. The relationship between strength (σ) and toughness (K_{IC}) can been used to predict a critical flaw size (a) using the equation[140]:

$$K_{IC} = 1.12\,\sigma\sqrt{\pi a} \qquad (22)$$

This parameter is plotted in Fig. 77 for each refractory, pre- and post-cycling, with the trends for constant defect sizes of 1mm and 2mm added for comparison. The results for each

refractory are broadly parallel with the linear flaw size trends, indicating that their critical flaw size remains roughly constant with cycling. Thus the reduction in strength in for LP and SA is not linked to an increase in flaw size and must be due to a drop in fracture toughness. In contrast, HP's toughness improves with cycling and hence its strength increases.

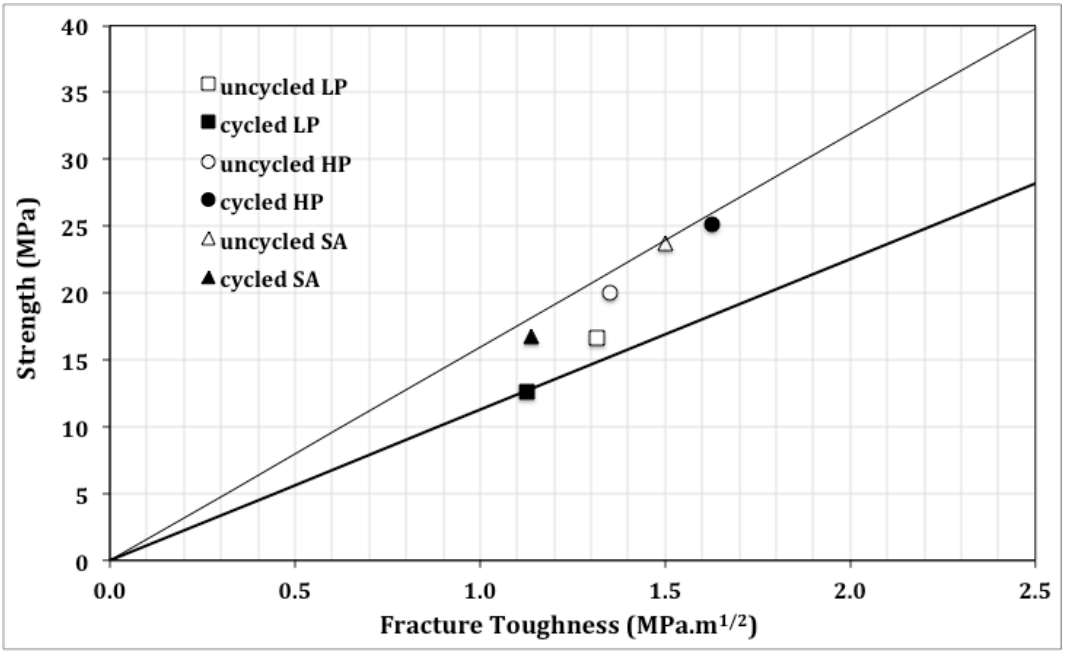

Figure 77 : Evolution of strength with cycling, as a function of toughness. Lines represent constant critical flaw sizes of 1mm (thin) and 2mm(thick).

The drop in fracture toughness for the SA refractory is consistent with its loss of connectedness. Aggregates cast loose within the matrix of this damaged microstructure would rapidly lose their potential to act as elastic bridging entities during crack propagation, leading to a reduction in WOF (Table 14).

Toughness in the LP refractory is degraded by the evolution of secondary phases within its aggregates: internal boundaries defined by these secondary phases have been shown to promote aggregate fissure (Section 5.1.5.). The observed increased incidence of transgranular fracture in LP would reduce the effectiveness of its aggregates as elastic bridges in the wake of a propagating crack. Only eight thermal cycles have been monitored here and the loss of aggregate integrity has not yet resulted in a significant loss of connectedness or stiffness. However, strength and toughness losses in these eight cycles imply ongoing deterioration of this refractory. An aspect not explored in this work is the impact of increased liquid phase within the matrix of the refractory. It was concluded in Chapter 4, that increased magnesium

content gives rise to increased liquid generation at elevated temperatures in these stabilised zirconia materials. The addition of Mg fines within the LP matrix is considered likely therefore, to give rise to additional levels of liquid at matrix-aggregate interfaces, thereby reducing bridging capability and consequently, toughness. Liquid infiltrating those aggregates already fractured through volume strains associated with internal secondary phase evolution would add a further dimension to toughness deterioration.

The HP refractory, with both stabilised matrix and aggregate phases, does not suffer the thermal strain mismatches described for the SA material during transformation events. Nor does it develop secondary phase degradation in its aggregates to anything like the extent of those in the LP refractory.. As it contains no Mg fines in its matrix, the impact of liquid phases is minimal for this material.

Bower and Ortiz[141] show that for reinforced composites, increased particle toughness relative to matrix toughness improves bulk effective toughness. In SA, matrix toughness is damaged due to loss of connectedness; in the LP refractory, aggregate toughness is compromised. HP's superior performance is attributed to the sustained integrity of its aggregates (Table 3, Section 4.1.1) and increased densification of its matrix with cycling, both of which enhance bulk toughness.

All three refractories indicate R-curve behaviour in their breakage curves, which are quasi-stable. This is consistent with the data in Table 14 which show that - although stored elastic strain energy (G) increases for HP after eight cycles - in none of the refractories does G come close to exceeding R (surface fracture energy, resisting crack propagation)[142]. R decreases by 23% for LP and 39% for SA with cycling, but increases by 26% for HP.

5.2.3. The impact of aggregates on thermal cycling resistance

Table 14 includes the d_{90} value for the aggregate populations of each of the refractories (aggregate diameter for the largest 10% of each material's aggregate population) and the diameter measured for the single largest aggregate in each refractory. Both the d_{90} and the largest-diameter value are estimates, based on an assumption of spherical shape for the aggregates, and using the area data from Chapter 4.1.2. The predicted critical flaw size is

double that of the *largest* aggregate dimensions calculated for the LP and HP refractories and the ratio is almost 5:1 for the SA refractory so that the direct link between aggregate size and critical flaw is not as straight forward as is often reported for refractories and concretes.

In Section 2.2.5., refractories studies were also reported to show that brittleness increases with transgranular fracture (high aggregate-matrix interface strength) and decreases with fracture along this interface. However, the 'characteristic length' (l_{ch}) in Table 14, calculated as:

$$l_{ch} = \frac{G_f.E}{\sigma^2} \tag{23}$$

with G_f equal to 2 x γ_{WOF}, is an inverse measure of brittleness and indicates low brittleness for LP (manifesting transgranular fracture) and high brittleness for HP (dominated by interface fracture). Thus the reported relationship between brittleness and mode of fracture does not hold up for these two samples in this study either.

What is evident is that the microstructural and mechanical evolution of these refractories is highly dependent on the degree of stabilisation of their aggregates. Where aggregate doping differs substantially, relative to the matrix phase, refractory connectedness is damaged by transformation strain mismatches, decreasing bulk stiffness. Where stabiliser levels are relatively high in the aggregates, secondary phase development is triggered which rapidly degrades the aggregates, reducing bulk refractory strength and toughness.

6. CONCLUSIONS

6.1. Work completed in this study

The Mg-PSZ refractories used as VIM crucibles and studied here are particle-reinforced composites and almost uniquely for this class of materials, their aggregate and matrix phases comprise the same mineralogy. Their variations in aggregate size and stabilisation, aggregate-matrix interface and matrix character give rise to different evolutions in microstructure and mechanical behaviour with thermal cycling. Samples were therefore heated to service temperatures (1750 °C) and cooled, eight times, with some tests performed pre- and post-cycling and others during cycling.

SEM imaging was used to size the aggregate populations and SEM observation to evaluate microstructural modification, after cycling, at micrometre scale. SEM-EDS and -WDS data were acquired to monitor stabiliser (Mg) mobility and to identify impurity elements and newly formed, secondary phases. Distribution of the latter was tracked with Raman micro-mapping and confirmed in one instance by TEM.

Thermal expansion and contraction was recorded (using dilatometry) during cycling, as was stiffness, using an impulse excitation technique. Strength and fracture toughness values were obtained from intact and single-edge notched bars respectively, subjected to three point bend tests. Double cantilever beam tests failed to deliver quantitative R-curves but produced fracture paths for SEM study. Fracture surfaces from the strength and fracture toughness tests were imaged using SEM and stereomicroscopy.

6.2. Findings of this study

The three products, studied here at micrometre (rather than nanometre) scale, comprised a variety of microstructures which modified as a result of thermal cycling. In several instances, this study has been able to attribute changes in mechanical properties, during and after cycling, to the evolving microstructure. These findings are summarised in Fig. 78 and as follows :

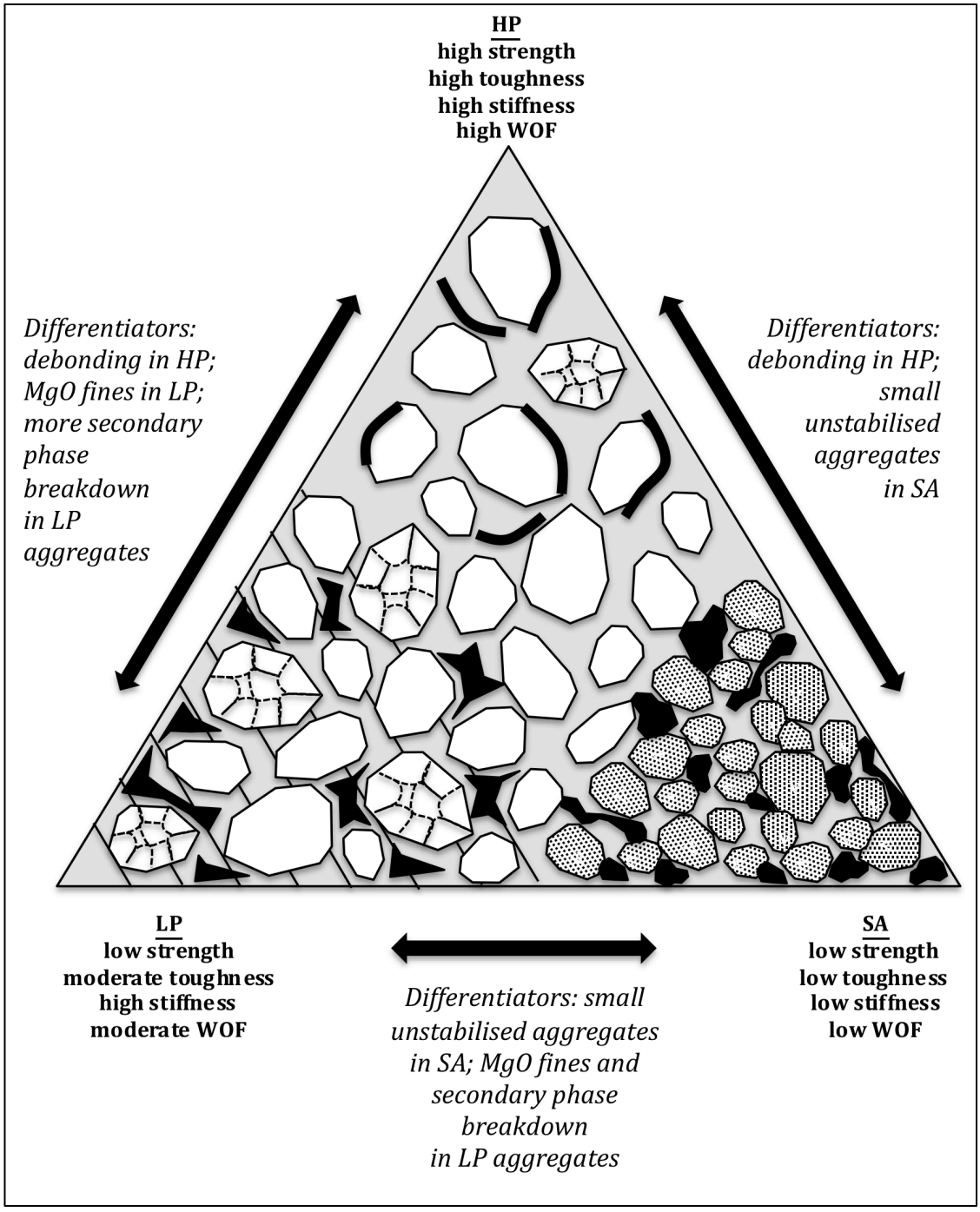

Figure 78 : Summary of links between microstructure and mechanical properties. White aggregates are Mg-stabilised and where subgrained, display hatched grids; shaded aggregates are unstabilised; grey matrix is stabilised and where striated, includes MgO fines; black phase represents porosity.

- The aggregates of the LP refractory develop segregated secondary phases along internal grain boundaries (discussed further below), leading to zones of weakness and eventual aggregate break-up. This degradation mechanism inhibits the aggregates' crack bridging capabilities (transgranular fracture is frequently observed in fracture surfaces), reducing toughness from ±1.3 to ±1.1 MPA.$m^{1/2}$ within the first eight cycles.

Strength-toughness correlations pre- and post-cycling indicate little change in the predicted critical flaw size, indicating that it is the drop in toughness which accounts for an observed drop in strength and work of fracture values for the same test conditions. Although bulk stiffness is stable during this early cycling history, the aggregate break-up mechanism is viewed as irreversible and compromised stability of the LP refractory is indicated for further service cycles. High levels of liquid generation are expected due to the addition of Mg fines to the matrix.

- The aggregates of the HP refractory display infrequent secondary phase development and aggregate break-up due to this mechanism is rare. These aggregates are characterised by partial interface debonding during firing. Fracture is intergranular as crack paths deflect around aggregates and this refractory retains its strength, stiffness and toughness on cycling. After eight cycles fracture energy increases by 26%.
- The aggregates of the SA refractory are unstabilised and are much smaller, as a population, relative to those of the LP and HP materials. They produce large strains during polymorphic transformation, in contrast to the particles of their adjacent matrix. This strain mismatch fractures the overall microstructure so that connectedness is lost and bulk stiffness is rapidly and irreversibly diminished (±44% drop) in just eight cycles. Multiple vibration frequencies at high temperatures suggest that the aggregates become entirely loosed for short periods of time within the microstructure, reducing their effectiveness at elastic bridging and decreasing toughness. Once more, a constant defect size is predicted from the toughness-strength relationship for this material, pre- and post-cycling so that strength losses are attributed to loss of toughness.

All three refractories display R-curve behaviour with fracture energies far in excess of stored elastic strain energies and quasi-stable fracture curves recorded during bend tests. However, the HP refractory is clearly the most thermally stable material of the three due to the retained integrity of its aggregates. A quantitative relationship between largest (or even average) aggregate size and predicted critical flaw size was not strongly born out by the results. In addition, transgranular fracture did not correlate with increased levels of brittleness, in contrast to studies reported elsewhere for concretes.

The findings of the microstructural evaluation yield the most novel outcome of this investigation: Alumina and silica impurities within the fused aggregates scavenge the Mg

stabiliser - from the aggregates in the case of LP and from the matrix particles in the case of SA - so that secondary phase liquids form at service temperatures. During cooling, forsterite, spinel and cordierite are crystallised. In the LP aggregates, these secondary phases produce internal grain boundaries, remnant from the zircon grains used in their manufacture where fusion does not perfectly homogenise the source ingot. In the SA refractory, the secondary phases fill interface regions between aggregate and matrix particles. These secondaries impact on the microstructures in three ways: i) volume changes during their formation vary from -3% (forsterite) to +14% (cordierite); ii) once formed, their thermal expansion coefficients differ from that of zirconia such that volume mismatches between the latter and the secondaries of up to 3% are predicted to arise in cycling and iii) they appear to present a path of weakness for crack growth leading to transgranular fracture.

6.3. Limitations and what remains to be learned

The scope of this study was broad and was consciously designed to be so in order to provide a full narrative on the material link between empirical physical changes and service outcome in real-world conditions. (The aim was for an applied, rather than wholly fundamental, study.) However, the broad scope has limited the degree to which individual mechanisms could be studied in depth. The limited sample set also included too many microstructural variations to allow conclusive links between all microstructural features and mechanical performance.

The work proceeded from anecdotal industry evidence that aggregate size strongly impacts on microstructural and mechanical evolution of the VIM refractories. Aggregate size did not turn out to be the central discriminator in refractory evolution at temperature and in retrospect, it is clear that far more attention was needed on the matrix phases. Future work on Mg-PSZ refractories could include :

- A study on the quantitative relationship between degree of secondary phase formation in fused aggregates and resulting refractory toughness. Wedge-splitting techniques, rather than double cantilever beam tests would be more suitable for toughness measurements. Experimental controls should ensure constant matrix composition and density between samples, uniformity in the presence / absence of debonding and stabilisation of both aggregate and matrix phases.

- Further studies on how metal oxide stabilisers used in zirconia influence liquid phase formation at service temperatures. This type of work would enhance fundamental use of ternary phase diagrams and the thermodynamic relationships they contain, to tweak microstructural design of fused refractories / ceramics.

6.4. Industrial implications

Understanding the links between composition, microstructure and mechanical evolution has implications for crucible manufacturers and customers: each VIM crucible costs several hundred pounds (GBP) and improving service life provides direct cost benefit for end users and sales advantages to suppliers. Indirect cost gains also arise from prevented loss of the high value Ni-Co based specialty alloys processed in the refractories.

Ceramicists working with zirconia are used to considering the damage due to phase changes in this mineral yet this study has proved that in addition to polymorphic transformations, serious concern must be given to formation of secondary phases in fused zirconia. Secondary phases break up stabilised fused aggregates, reducing their host refractory toughness and strength. Where secondary phases form at microstructural interfaces, they jeopardise refractory connectedness. In order to anticipate secondary phase damage, crucible designers need to consider two aspects :

- Mg availability determines the *extent* to which secondary phases will form: LP aggregates contained higher overall stabiliser levels, relative to the HP aggregates, by only ±1 wt%. Yet modeling predicts that the former will produce more than double the amount of secondary liquid segregation at service temperatures, as a result. Stabiliser distributions should therefore be well constrained in raw material inputs to crucible manufacture.
- The levels of alumina and silica impurity in fused zirconia aggregates determine the *feasibility* of secondary phase formation. Current restrictions on access to mineral deposits of baddeleyite often mean zircon sand is used as a source of fused zirconia instead. Alumina within zircon sand may be held in kyanite lattices, making extraction difficult so that some level of impurity is always present. Baddeleyite sources may provide higher purity zirconia.

****

REFERENCES

1. Shaw, K., *Refractories and Their Uses.* Halsted Press Division, Wiley and Sons: New York, 1972.
2. Chesters, J. H., *Refractories Production and Properties.* The Metals Society: London, 1983.
3. Garbers-Craig, A. M., Presidential Address : How Cool are Refractory Materials ? *The Journal of the Southern African Institute of Mining and Metallurgy* **2005,** *108* (September), 1-16.
4. Committee, I. S. O., ISO10081-4:2007 Classification of Dense Shaped Refractory Products. In *Special Products*, Published online, 2007.
5. Kisi, E. H.; Howard, C. J., Crystal Structures of Zirconia Phases and their Inter-Relation. *Key Engineering Materials* **1998,** *153-154*, 1-36.
6. Riley, F., *Structural ceramics : Fundamentals and Case Studies.* Cambridge University Press: Cambridge, 2009.
7. Green, D. J.; Hannink, R. H. J.; Swain, M. V., *Transformation Toughening of Ceramics.* CRC Press: Boca Raton, Florida, 1989.
8. Lee, W. E.; Rainforth, M. W., *Ceramic microstructures : Property Control by Processing.* Chapman and Hall: London, 1994.
9. Bradt, R. C., The Crack Growth Resistance of Refractories in the Following Wake Region behind the Crack Front. In *St Louis Refractories Meeting*, unpublished: 2012.
10. Brooks, R., Refractory Demand Shows Patterns of Industrial Growth. *Foundry Management and Technology* May 16, 2013.
11. Blackford, J., Engineering of Superalloys. Centre for Materials Science and Engineering, The University of Edinburgh: 2002.
12. Cahn, R. W., The Coming of Materials Science. In *The Coming of Materials Science* Cahn, R. W., Ed. Pergamon: Oxford, 2001; Vol. 5.
13. Pollock, T. M.; Tin, S., Nickel-Based Superalloys for Advanced Turbine Engines : Chemistry, Microstructure, and Properties. *Journal of Propulsion and Power* **2006,** *22* (2), 361-374.
14. Choudhury, A., State of the Art of Superalloy Production for Aerospace and Other Application Using VIM/VAR or VIM/ESR. *ISIJ International* **1992,** *32* (5), 563-574.
15. Holt, R. T.; Wallace, W., Review 203 :Impurities and Trace Elements in Nickel-Base Superalloys. *International Metals Reviews* **1976,** *March*, 1-24.

16. Flaitz, P. L.; Pask, J. A., Penetration of Polycrystalline Alumina by Glass at High Temperatures. *Journal of the American Ceramic Society* **1987,** *70* (7), 449-455.
17. Evans, A. G.; Burlingame, N.; Drory, M.; Kriven, W. M., Martensitic Transformations in Zirconia - Particle Size Effects and Toughening. *Acta Metallurgica* **1981,** *29*, 447-456.
18. Ruhle, M.; Heuer, A. H., Phase Transformations in ZrO2-Containing Ceramics: II, The Martensitic Reaction in t-ZrO_2. In *Science and Technology of Zirconia II*, Claussen, N.; Ruhle, M.; Heuer, A., Eds. The American Ceramic Society Inc.: Columbus, Ohio, 1984.
19. Curtis, C. E., Development of Zirconia Resistant to Thermal Shock. *Journal of the American Ceramic Society* **1946,** *30* (6), 180-196.
20. Garvie, R. C., The Occurrence of Metastable Tetragonal Zirconia as a Crystallite Size Effect. *The Journal of Physical Chemistry* **1965,** *69* (4), 1238-1243.
21. Heuer, A. H.; Claussen, N.; Kriven, W. M.; Ruhle, M., Stability of Tetragonal ZrO_2 Particles in Ceramic Matrices. *Journal of the American Ceramic Society* **1982,** *65* (12), 642-650.
22. Basu, B.; Vleugels, J.; Biest, O. V. D., Transformation Behaviour of Tetragonal Zirconia : Role of Dopant Content and Distribution. *Materials Science and Engineering* **2004,** *A366*, 338-347.
23. Orange, G.; Fantozzi, G.; Cambier, F.; Leblud, C.; Anseau, M. R.; Leriche, A., High Temperature Mechanical Properties of Reaction-Sintered Mullite/Zirconia and Mullite/Alumina/Zirconia Composites. *Journal of Materials Science* **1985,** *20*, 2533-2540.
24. Choi, S. R.; Bansal, N. P., Mechanical Behaviour of Zirconia/Alumina Composites. *Ceramics International* **2005,** *31*, 39-46.
25. Cabodi, I.; Gaubil, M., New Highly Resistive High Zirconia Fused Cast Products for Electrode Blocks Application. *The Refractories Engineer* **2013,** (May), 21-25.
26. Lataste, E.; Erauw, J.-P.; Olagnon, C.; Fantozzi, G., Microstructural and Mechanical Consequences of Thermal Cycles on a High Zirconia Fuse-Cast Refractory. *Journal of the European Ceramic Society* **2009,** *29*, 587-594.
27. Sibil, A.; Douillard, T.; Cayron, C.; Godin, N.; R'mili, M.; Fantozzi, G., Microcracking of High Zirconia Refractories after t->m Phase Transition during Cooling: An EBSD study. *Journal of the European Ceramic Society* **2011,** *31*, 1525-1531.
28. Huger, M.; Ota, T.; Tessier-Doyen, N.; Michaud, P.; Chotard, T. In *Microstructural Effects Associated to CTE Mismatch for Enhancing the Thermal Shock Resistance of Refractories.*,

ICC3 : Symposium 16: Innovation in Refractories and Traditional Ceramics, IOP Publishing: 2011; pp 1-6.

29. Sarpoolaky, H.; Zhang, S.; Argent, B. B.; Lee, W. E., Influence of Grain Phase on Slag Corrosion of Low-Cement Castable Refractories. *Journal of the American Ceramic Society* **2001,** *84* (2), 426-434.
30. Kaniuk, J. A.; DiRuggiero, C.; Ratcliffe, D. K. Quick Change Crucible for Vacuum Melting Furnace. 1995.
31. Zircoa Engineering Guide for Zircoa's Foundry Crucibles. http://www.zircoa.com/assets.common/pdfs/crucible.pdf (accessed 19 March 2013).
32. Lee, W. E.; Zhang, S.; Karakus, M., Refractories : Controlled Microstructure Composites for Extreme Environments. *Journal of Materials Science* **2004,** *39*, 6675-6685.
33. Evans, A. G., Toughening Mechanisms in Zirconia Alloys. In *Science and Technology of Zirconia II*, Claussen, N.; Ruhle, M.; A.Heuer, Eds. The American Ceramic Society Inc.: Columbus, Ohio, 1984.
34. Porter, D. L.; Heuer, A. H., Microstructural Development in MgO-Partially Stabilized Zirconia (Mg-PSZ). *Journal of the American Ceramic Society* **1979,** *62* (5-6), 298-305.
35. Grain, C. F., Phase Relations in the ZrO_2-MgO System. *Journal of the American Ceramic Society* **1967,** *50* (6), 288-290.
36. Society, T. A. C.; 31, N. S. R. D., ACerS - NIST Phase Equilibrium Diagrams Version 3.3.0. The American Ceramic Society: Westerville.
37. Hughan, R. R.; Hannink, R. H. J., Precipitation During Controlled Cooling of Magnesia-Partially-Stabilised Zirconia. *Journal of the American Ceramic Society* **1986,** *69* (7), 556-563.
38. Bocanegra-Bernal, M. H.; Torre, S. D. D. L., Review : Phase Transitions in Zirconium Dioxide and Related Materials for High Performance Engineering Ceramics. *Journal of Materials Science* **2002,** *37*, 4947-4971.
39. Hannink, R. H. J., Growth Morphology of the Tetragonal Phase in Partially Stabilised Zirconia. *Journal of Materials Science* **1978,** *13*, 2487-2496.
40. Heuer, A. H.; Schoenlein, L. H., Thermal Shock Resistance of Mg-PSZ. *Journal of Materials Science* **1985,** *20*, 3421-3427.
41. Farmer, S. C.; Heuer, A. H.; Hannink, R. H. J., Eutectoid Decomposition of MgO-Partially-Stabilized ZrO_2. *Journal of the American Ceramic Society* **1987,** *70* (6), 431 - 440.

42. Martin, S.; Berek, H.; Aneziris, C. G.; Martin, U.; Rafaja, D., Pitfalls of Local and Quantitative Phase Analysis in Partially Stabilized Zirconia. *Journal of Applied Crystallography* **2012,** *45*, 1136-1144.

43. Farmer, S. C.; Schoenlein, L. H.; Heuer, A. H., Precipitation of $Mg_2Zr_5O_{12}$ in MgO-Partially-Stabilized ZrO_2. *Communications of the American Ceramics Society* **1983**, C107-C109.

44. Chaim, R.; Brandon, D. G., Microstructure Evolution and Ordering in Commercial Mg-PSZ. *Journal of Materials Science* **1984,** *19*, 2934-2942.

45. Abe, F.; Muneki, S.; Yagi, K., Tetragonal to Monoclinic Transformation and Microstructural Evolution in ZrO_2 - 9.7 mol% MgO during Cyclic Heating and Cooling. *Journal of Materials Science* **1997,** *32*, 513-522.

46. Bennett, G., Personal Communication. Imerys: February 2014.

47. Bennett, G., Personal Communication, Imerys: April 2014.

48. Aiba, Y.; Oki, K.; Sugie, M.; Kurihara, K.; Oya, S., Study of Corrosion and Penetration of Zirconia Refractories by Molten Steel and Slag (3rd Report). *Taikabutsu Overseas* **1985,** *5* (1), 3-11.

49. Hino, Y.; Kiyota, Y., Fatigue Failure Behavior of Al_2O_3-SiO_2 System Bricks under Compressive Stress at Room and High Temperatures. *ISIJ International* **2012,** *52* (6), 1045-1063.

50. Hino, Y.; Yoshida, K.; Kiyota, Y.; Kuwayama, M., Fracture Mechanics Investigation of MgO-C Bricks for Steelmaking by Bending and Fatigue Tests Along with X-Ray CT Scan Observation. *ISIJ International* **2013,** *53* (8), 1392-1400.

51. Guo, X.; Tang, C.-Q.; Yuan, R.-Z., Grain Boundary Ionic Conduction in Zirconia-based Solid Electrolyte with Alumina Addition. *Journal of the European Ceramic Society* **1995,** *15*, 25-32.

52. Butler, E. P.; Drennan, J., Microstructural Analysis of Sintered High-Conductivity Zirconia with Al_2O_3 Additions. *Journal of the American Ceramic Society* **1982,** *65* (10), 474 - 478.

53. Aneziris, C. G.; Pfaff, E. M.; Maier, H. R., Fine Grained Mg-PSZ Ceramics with Titania and Alumina or Spinel Additions for Near Net Shape Steel Processing. *Journal of the European Ceramic Society* **2000,** *20*, 1729 - 1737.

54. Stough, M. A.; Jr., J. R. H., Solid Solubility and Precipitation in a Single-Crystal Alumina-Zirconia System. *Journal of the American Ceramic Society* **2002,** *85* (12), 2895-2902.

55. Aksel, C.; Rand, B.; Riley, F. L.; Warren, P. D., Mechanical Properties of Magnesia-Spinel Composites. *Journal of the European Ceramic Society* **2002,** *22*, 745 - 754.
56. Schacht, C. A., Thermomechanical Considerations for Refractor Linings. In *Refractories Handbook*, Schacht, C. A., Ed. Marcel Dekker Inc.: New York, 2004.
57. Lawn, B. R., *Fracture of Brittle Solids*. Cambridge University Press: Cambridge, 1993.
58. Nakayama, J., Direct Measurement of Fracture Energies of Brittle Heterogeneous Materials. *Journal of the American Ceramic Society* **1965,** *48* (11), 583-587.
59. Hasselman, D. P. H., Thermal Stress Resistance Parameters for Brittle Refractory Ceramics : A Compendium. *Bulletin of the American Ceramic Society* **1970,** *49* (12), 1033-1037.
60. Hasselman, D. P., Unified Theory of Thermal Shock Fracture Initiation and Crack Propagation in Brittle Ceramics. *Journal of the American Ceramic Society* **1969,** *52* (11), 600-604.
61. Salvini, V. R.; Pandolfelli, V. R.; Bradt, R. C., Extension of Hasselman's Thermal Shock Theory for Crack/Microstructure Interactions in Refractories. *Ceramics International* **2012,** *38*, 5369-5375.
62. Gogotsi, G. A.; Grushevsky, Y. L.; Strelov, K. K., The Significance of Non-Elastic Deformation in the Fracture of Heterogeneous Ceramic Materials. *Ceramurgia* **1978,** *4* (2), 113-118.
63. Swain, M. V., R-Curve Behaviour and Thermal Shock Resistance of Ceramics. *Journal of the American Ceramic Society* **1990,** *73* (3), 621-628.
64. Bradt, R. C., Fracture of Refractories. In *Refractories Handbook*, Schacht, C. A., Ed. Marcel Dekker Inc.: New York, 2004.
65. Harmuth, H.; Tschegg, E. K., A Fractue Mechanics Approach for the Development of Refractory Materials with Reduced Brittleness. *Fatigue and Fracture of Engineering Materials and Structures* **1997,** *20* (11), 1585-1603.
66. Harmuth, H.; Bradt, R. C., Review : Investigation of Refractory Brittleness by Fracture Mechanical and Fractographic Methods. *Interceram Refractories* 2010, pp 6-10.
67. Marshall, D. B., Strength Characteristics of Transformation-Toughened Zirconia. *Journal of the American Ceramic Society* **1986,** *69* (3), 173-180.
68. Swain, M. V., Inelastic Deformation of Mg-PSZ and its Significance for Strength-Toughness Relationship of Zirconia Toughened Ceramics. *Acta Metallurgica* **1985,** *33* (11), 2083-2091.

69. Ribeiro, S.; Rodrigues, J. A., The Influence of Microstructure on the Maximum Load and Fracture Energy of Refractory Castables. *Ceramics International* **2010,** *36*, 263-274.
70. Damhof, F.; Tesselaar, W.; Eynden, J. C. v. d., A Novel Experimental Approach to Investigate Thermal Shock Damage in Refractory Materials. *Ceramic Forum International* **2007,** *84*, 75-79.
71. Lawson, S., Review : Environmental Degradation of Zirconia Ceramics. *Journal of the European Ceramic Society* **1995,** *15*, 485-502.
72. Boccaccini, D. N.; Cannio, M.; Volkov-Husoviae, T. D.; Kamseu, E.; Romagnoli, M.; P.Veronesi; Leonelli, C.; Dlouhy, I.; Boccacini, A. R., Service Life Prediction for Refractory Materials. *Journal of Materials Science* **2008,** *43*, 4079-4090.
73. Luz, A. P.; Jr., T. S.; Medeiros, J.; Pandolfelli, V. C., Thermal Shock Damage Evaluation of Refractory Castables via Hot Elastic Modulus Measurements. *Ceramics International* **2013,** *39*, 6189-6197.
74. Boccaccini, D. N.; Romagnoli, M.; Veronesi, P.; Cannio, M.; Leonelli, C.; Pellacani, G., Quality Control and Thermal Shock Damage Characterization of High-Temperature Ceramics by Ultrasonic Pulse Velocity Testing. *International Journal of Applied Ceramic Technologies* **2007,** *4* (3), 260-268.
75. Sadowski, T.; Golewski, G., Effect of Aggregate Kind and Graining on Modelling of Plain Concrete under Compression. *Computational Materials Science* **2008,** *43*, 119-126.
76. Grassl, P.; Wong, H. S.; Buenfeld, N. R., Influence of Aggregate Size and Volume Fraction on Shrinkage Induced Micro-cracking of Concrete and Mortar. *Cement and Concrete Research* **2010,** *40*, 85-93.
77. Guinea, G. V.; El-Sayed, K.; Rocco, C. G.; Elices, M.; Planas, J., The Effect of the Bond between the Matrix and the Aggregates on the Cracking Mechanism and Fracture Parameters of Concrete. *Cement and Concrete Research* **2002,** *32*, 1961-1970.
78. Thermal Ceramics, 94M Zirconia. Datasheet R137.R192. Copyright of Morgan Advanced Materials, 2010.
79. Priese, A., private communication. Imerys: February 2014.
80. Ledsham, J., private communication. Minchem HMP: April 2014.
81. Francus, P., An Image-Analysis Technique to Measure Grain-size Variation in Thin Sections of Soft Clastic Sediments. *Sedimentary Geology* **1998,** *121*, 289-298.
82. Cooper, M. C., The Use of Digital Image Analysis in the Study of Laminated Sediments. *Journal of Paleolimnology* **1997,** *19*, 33-40.

83. Fortey, N. J., Image Analysis in Mineralogy and Petrology. *Mineralogical Magazine* June 1995, 1995, pp 177-178.
84. Muirhead, J.; Cawley, J.; Strang, A.; English, C. A.; Titchmarsh, J., Quantitative Aspects of Grain Size Measurement. In *Quantitative Microscopy of High Temperature Materials*, Strang, A.; Cawley, J., Eds. IOM Communications: London, 2001; Microstructure of High Temperature Materials, Number 5.
85. Roebuck, B., Measurement of Grain Size and Size Distribution in Engineering Materials. In *Quantitative Microscopy of High Temperature Materials*, Strang, A.; Cawley, J., Eds. IOM Communications Ltd: London, 2001; Microstructure of High Temperature Materials, Number 5.
86. Kimball, S.; Mattis, P.; Team, G. D. *GNU Image Manipulation Programme*, 2.6.11; 2008.
87. Rasband, W. *ImageJ*, 1.45s; National Institutes of Health: USA.
88. Reinking, L. Examples of Image Analysis Using Image J : Particle Counting and Analysis 2007. http://rsbweb.nih.gov/ij/docs/pdfs/examples.pdf (accessed 19 February 2013).
89. Newbury, D. E. In *Quantitative Electron Probe Microanalysis (EPMA): Doing It Right and Doing It Wrong!*, CeCAMP, Gaithersburg, National Institute of Standards and Technology: Gaithersburg, 2004.
90. Pouchou, J.-L.; Pichoir, F., Quantitative Analysis of Homogeneous or Stratified Microvolumes Applying the Model "PAP". In *Electron Probe Quantitation*, Heinrich, K. F. J.; Newbury, D. E., Eds. Plenum Press: New York, 1991.
91. Botta, W. J. In *Advanced Electron-Optics Techniques for Materials Characterization, TEM/ SEM/ STEM/ HAADF/ EELS.*, SANCAS MSE, Sao Carlos, Universidade Federal de Sao Carlos: Sao Carlos, 2012.
92. Williams, D. B.; Carter, C. B., *Transmission Electron Microscopy. A Textbook for Materials Science.* Springer: New York, 2009.
93. Pittayachawan, P. Comparative Study of Physical Properties of Zirconia Based Dental Ceramics. University College London (UCL), UCL Discovery Open Access, 2009.
94. Sonneveld, E. J.; Visser, J. W., Automatic Collection of Powder Data from Photographs. *Applied Crystallography* **1975,** *8*, 1-7.
95. Garvie, R. C.; Nicholson, P. S., Phase Analysis in Zirconia Systems. *Journal of the American Ceramic Society* **1972,** *55* (6), 303-305.

96. Toraya, H.; Yoshimura, M.; Somiya, S., Quantitative Analysis of Monoclinic-Stabilized Cubic ZrO2 Systems by X-Ray Diffraction. *Communications of the American Ceramics Society* **1984,** *September*, C183-C184.

97. Minsky, M., Memoir on Inventing the Confocal Scanning Microscope. *Scanning* **1988,** *10*, 128-138.

98. Gazzoli, D.; Mattei, G.; Valigi, M., Raman and X-ray Investigations of the Incorporation of Ca2+ and Cd2+ in the ZrO2 Structure. *Journal of Raman Spectroscopy* **2007,** *38*, 823-831.

99. Bowden, M.; Dickson, G. D.; Gardiner, D. J.; Wood, D. J., Patterns of Stress-Induced Phase Transformation in MgO-Stabilized Zirconia Ceramic Revealed using Micro-Raman Imaging. *Journal of Materials Science* **1993,** *28*, 1031-1036.

100. Naumenko, A. P.; Berezovska, N. I.; Biliy, M. M.; Shevchenko, O. V., Vibrational Analysis and Raman Spectra of Tetragonal Zirconia. *Physics and Chemistry of Solid State* **2008,** *9* (1), 121-125.

101. Bale, C. W.; Pelton, A. D.; Thompson, W. T.; Eriksson, G.; Hack, K.; Chartrand, P.; Decterov, S.; Jung, I.-H.; Melancon, J.; Petersen, S., FactSage 6.2. Thermfact - GTT Technologies: 2010.

102. Lee, W. E.; Argent, B. B.; Zhang, S., Complex phase equilibria in refractories design and use. *Journal of the American Ceramic Society* **2002,** *85* (12), 2911-2918.

103. Bale, C. W.; Belisle, E.; P.Chartrand; Decterov, S. A.; Eriksson, G.; Hack, K.; Jung, I.-H.; Kang, Y.-B.; Melancon, J.; Pelton, A. D.; Robelin, C.; Petersen, S., FactSage Thermochemical Software and Databases - Recent Developments. *Computer Coupling of Phase Diagrams and Thermochemistry* **2009,** *33*, 295-311.

104. ASTM, E1876-07, Standard Test Method for Dynamic Young's Modulus, Shear Modulus,and Poisson's Ratio by Impulse Excitation of Vibration. ASTM International: West Conshohocken, 2007

105. Walshaw, A. C., *Mechanical Vibrations with Applications.* Ellis Horwood Ltd.: Chichester, 1984.

106. Roebben, G.; Bollen, B.; Brebels, A.; Humbeeck, J. V.; Biest, O. V. d., Impulse Excitation Apparatus to Measure Resonant Frequencies, Elastic Moduli and Internal Friction at Room and High Temperature. *Review of Scientific Instruments* **1997,** *68* (12), 4511-4515.

107. Roebben, G.; Donzel, L.; Stemmer, S.; Steen, M.; Schaller, R.; Biest, O. V. D., Viscous Energy Dissipation at High Temperatures in Silicon Nitride. *Acta Materialia* **1998,** *46* (13), 4711-4723.

108. Pihlatie, M.; Kaiser, A.; Mogensen, M., Mechanical Properties of NiO/Ni-YSZ Composites Depending on Temperature, Porosity and Redox Cycling. *Journal of the European Ceramic Society* **2009,** *29*, 1657-1664.

109. Weller, M.; Schubert, H., Internal Friction, Dielectric Loss, and Ionic Conductivity of Tetragonal ZrO_2-3%Y_2O_3 (Y-TZP). *Journal of the American Ceramic Society* **1986,** *69* (7), 573-577.

110. Lins, W.; Kaindl, G.; Peterlik, H.; Kromp, K., A Novel Resonant Beam Technique to Determine the Elastic Moduli in Dependence on Orientation and Temperature up to 2000C. *Review of Scientific Instruments* **1999,** *70* (7), 3052-3058.

111. Roebben, G.; Basu, B.; Vleugels, J.; Biest, O. V. D., Transformation-induced Damping Behaviour of Y-TZP zirconia ceramics. *Journal of the European Ceramic Society* **2003,** *23*, 481-489.

112. Latella, B. A.; Humphries, S. R., Young's Modulus of a 2.25Cr-1Mo Steel at Elevated Temperature. *Scripta Materialia* **2004,** *51*, 635-639.

113. ASTM, C133-97 (2008) Standard Test Methods for Cold Crushing Strength and Modulus of Rupture of Refractories. ASTM International: Conshohocken, 2008. .

114. Rooke, D. P.; Cartwright, D. J., *Compendium of Stress Intensity Factors.* Her Majesty's Stationary Office: London, 1976.

115. Sorensen, B. F.; Horsewell, A.; Jorgensen, O.; Kumar, A. N., Fracture Resistance Measurement Method for in situ Observation of Crack Mechanisms. *Journal of the American Ceramic Society* **1998,** *81* (3), 661-669.

116. Heuer, A. H.; Readey, M. J.; Steinbrech, R., Resistance Curve Behavior of Supertough MgO-partially-stabilized ZrO_2. *Materials Science and Engineering* **1988,** *A105/106*, 83-89.

117. Marshall, D.; Swain, M. V., Crack Resistance Curves in Magnesia-Partially-Stabilized Zirconia. *Journal of the American Ceramic Society* **1988,** *71* (6), 399-407.

118. Swain, M. V.; Garvie, R. C.; Hannink, R. H. J., Influence of Thermal Decomposition on the Mechanical Properties of Magnesia-Stabilized Cubic Zirconia. *Journal of the American Ceramic Society* **1983,** *66* (5), 358-362.

119. Osborn, E. F.; Muan, A., Phase Equilibrium Diagrams of Oxide Systems. American Ceramic Society with Edward Orton Jr. Ceramic Foundation: Columbus, Ohio, 1960.
120. Levin, E. M.; Robbins, C. R.; McMurdie, H. F., *Phase Diagrams for Ceramists.* American Ceramic Society: Columbus, Ohio, 1964.
121. ENS-Lyon, Handbook of Raman Spectra, http://www.ens-lyon.fr/LST/Raman: Free database 2000-2014.
122. Poon, W. C.-K.; Putnis, A.; Salje, E., Structural States of Mg Cordierite: IV. Raman Spectroscopy and Local Order Parameter Behaviour. *Journal of Physics : Condensed Matter* **1990,** *2*, 6361-6372.
123. McMillan, P.; Putnis, A.; Carpenter, M. A., A Raman Spectroscopic Study of Al-Si Ordering in Synthetic Magnesium Cordierite. *Physics and Chemistry of Minerals* **1984,** *10*, 256-260.
124. Slotznick, S. P.; Shim, S.-H., In Situ Raman Spectroscopy Measurements of MgAl2O4 Spinel up to 1400 C. *American Mineralogist* **2008,** *93*, 470-476.
125. Zucker, R.; Shim, S.-H., In Situ Raman Spectroscopy of $MgSiO_3$ Enstatite up to 1550K. *American Mineralogist* **2009,** *94*, 1638-1646.
126. Marshall, D. B.; James, M. R.; Porter, J. R., Structural and Mechanical Property Changes in Toughened Magnesia-Partially-Stabilized Zirconia at Low Temperatures. *Journal of the American Ceramic Society* **1989,** *72* (2), 218-227.
127. Bauer, C.; Rollinger, B.; Krumpel, G.; Hoad, O.; Pascual, J.; Rogers, N. In *Characterization Methods of Zirconia and the Impact of Stabilizing Agents on its Functionality.*, UNITECR 2013, Victoria, Canada, Goski, D.; Smith, J. D., Eds. Wiley: Victoria, Canada, 2013; p 1408.
128. Pramarna, S., Personal Communication.
129. Bouhifd, M. A.; Andrault, D.; Fiquet, G.; Richet, P., Thermal Expansion of Forsterite up to the Melting Point. *Geophysical Research Letters* **1996,** *23* (10), 1143-1146.
130. Goren, R.; Gocmez, H.; Ozgur, C., Synthesis of Cordierite Powder from Talc, Diatomite and Alumina. *Ceramics International* **2005,** *in press*.
131. Wadsworth, I.; Wang, J.; Stevens, R., Zirconia Toughened Cordierite. *Journal of Materials Science* **1990,** *25*, 3982 - 3989.
132. Doral, Product Data Sheet: Zircon Standard Grade. 2013; PDS-004-2b-DMS-Zircon Sand.
133. Maitre, A.; Lefort, P., Solid State Reaction of Zirconia with Carbon. *Solid State Ionics* **1997,** *104*, 109-122.

134. Norton, F. H., The Thermal Expansion of Refractories. *Journal of the American Ceramic Society* **1925,** *8* (12), 799-815.
135. Caproni, E.; Muccillo, R., Preparation and Characterization of Zirconia-Yttria / Zirconia-Magnesia Composites. *Materials Science Forum* **2006,** *530-531*, 389-394.
136. Fogaing, E. Y.; Huger, M.; Gault, C., Elastic Properties and Microstructure: Study of Two Fused Cast Refractory Materials. *Journal of the European Ceramic Society* **2007,** *27*, 1843-1848.
137. Patapy, C.; Gault, C.; Huger, M.; Chotard, T., Acoustic Characterization and Microstructure of High Zirconia Electrofused Refractories. *Journal of the European Ceramic Society* **2009,** *29*, 3355-3362.
138. Tattersall, H. G.; Tappin, G., The Work of Fractue and its Measurement in Metals, Ceramics and Other Materials. *Journal of Materials Science* **1966,** *1*, 296-301.
139. Bradt, R. C., Elastic Moduli, Strength and Fracture Characteristics of Refractories. *Key Engineering Materials* **1993,** *88*, 165-192.
140. Wei, W.-C. J.; Lin, Y.-P., Mechanical and Thermal Shock Properties of Size Graded MgO-PSZ Refractory. *Journal of the European Ceramic Society* **2000,** *20*, 1159-1167.
141. Bower, A. F.; Ortiz, M., A Three-Dimensional Analysis of Crack Trapping and Bridging by Tough Particles. *Journal of Mechanics and Physics of Solids* **1991,** *39* (6), 815-858.
142. Vandeperre, L. J.; Inagaki, Y.; Clegg, W. J., Thermal Shock of Porous Silicon Nitride with Preferentially Aligned Grains. *Journal of Materials Research* **2003,** *18* (11).